Antibody Targeted Magnetic Nanoparticle Hyperthermia for Cancer Therapy

Bettina Kozissnik

A thesis submitted to the University College London for the degree of
Doctor of Philosophy in the Faculty of Biomedical Sciences,
Department of Oncology,
UCL Cancer Institute,
University College London

November 2013

Abstract

Superparamagnetic iron oxide nanoparticles (SPION) are used clinically to improve the sensitivity of magnetic resonance imaging (MRI). A less exploited property of SPION is their ability to generate heat when subjected to an alternating magnetic field, a process called magnetic alternating current hyperthermia (MACH). Hyperthermia has been shown to be a cancer effective treatment modality in the clinic when given together with radio/chemotherapy. However, delivery of sufficient heat to damage tumours without harming healthy tissue remains challenging. The central hypothesis for this thesis is that MACH activated SPION can be used to generate hyperthermia *in situ* and therefore will have potential to achieve localised hyperthermic cancer treatments.

The aim of the thesis was to evaluate the potential of SPION to deliver localised hyperthermia by: (1) Characterization and comparison of SPION to select a lead candidate for clinical application. (2) Developing conjugation methods to confer SPION with cancer-binding properties by attachment of single chain Fv antibodies (scFv). (3) Evaluating the localisation and heating potential *in vivo*.

SPION were characterized with regard to their hydrodynamic diameter, core size, magnetic properties, atomic iron content and heating potential for hyperthermia application. Different chemistries were evaluated to functionalize the most promising candidate using shMFEm, an scFv targeting the carcinoembryonic antigen (CEA). A CEA-non-binding scFv variant, shNFEm, was used as a negative control. Functionality of the scFv-SPIONs was assessed using quartz crystal microbalance. *In vivo* heating potential of the SPION was tested in a xenograft tumour model *in vivo*, using bespoke MACH apparatus.

The results established Ferucarbotran (FX), unformulated Resovist®, an MRI contrast agent, as the most suitable candidate for hyperthermia application. Cyanogen bromide chemistry was selected to functionalise Ferucarbotran with the scFvs shMFEm. The FX-scFv conjugates were purified and analysed. Functionality was confirmed by quartz crystal microbalance, enabling the first visualisation of the interaction between a SPION-scFv conjugate and cognate antigen in real-time. The *in vivo* assessment of Ferucarbotran and the FX-scFv conjugates confirmed the *in vitro* heating potential of Ferucarbotran. *In vivo* analysis of heating showed that localised hyperthermia was achievable with intratumoral injection followed by MACH. Histological analysis of the tumours revealed an uneven distribution of particles within the tumours and an accumulation of the particles within the surrounding stroma indicating the future work should include study of innovative tumour delivery methods.

These results support the hypothesis of a therapeutic potential for targeted magnetic nanoparticle hyperthermia and indicates the challenges that have be addressed to enable clinical application of this treatment modality.

Declaration of Originality

"I declare in lieu of an oath that I have written this thesis myself and that I have not used any sources or resources other than stated for its preparation. I further declare that I have clearly indicated all direct and indirect quotations. This thesis has not been submitted elsewhere for examination purposes."

November 2013

Table of Contents

List of Figures

Chapter 5

List of Tables

Chapter 2

Chapter 3

Chapter 4

Appendix I

List of Equations

Chapter 1

Chapter 2

Abbreviations

A	Amplitude
A375M	Human melanoma cell line
AC	Alternating current
ADCC	Antibody dependent cellular toxicity
ADEPT	Antibody-directed enzyme prodrug therapy
AMF	Alternating magnetic field
Anti-His	Monoclonal antibody raised against the hexahistidine tag
ATCC	American Type Culture Collection
BNF starch	starch coated nanoparticles from Micromod GmbH
BSA	Bovine serum albumin
Capan-1	Human pancreatic adenocarcinoma cell line
CDRs	Complementary determining regions
CEA	Carcinoembryonic antigen
CNBr	Cyanogen bromide
COOH	Carboxyl group
Da	Dalton
DAB	3,3'-Diaminobenzidine
DC	Direct current
dH_2O	distilled water
DLS	Dynamic light scattering
DMSO	Dimethyl sulfoxide
DNA	Desoxyribonucleic acid
E. coli	*Escherichia coli*
ECL	Enhanced chemiluminescence
EDC	*N*-ethyl-*N'*-(3-diethyl-aminopropyl)-carbodiimide
EDTA	Ethylenediamine tetraacetic acid
ELISA	Enzyme-linked immunosorbent assay
EMA	European Medicines Agency
emu	electromagnetic unit
EPR	Enhanced permeability and retention effect
EU	European Union
Fab	Fragment antibody binding
FCS	Fetal calf serum
FDA	US Food and Drug Administration

Fe	Iron
Fe_3O_4	Magnetite
fM-CMX	carboxydextran coated nanoparticles from Chemicell GmbH
fM-DX	dextran coated nanoparticles from Chemicell GmbH
fM-DXS	dextran sulphate coated nanoparticles from Chemicell GmbH
FPLC	Fast pressure liquid chromatography
Fv	Fragment variable
FX	Ferucarbotran
g	gram
Gd	Gadolinium
GMP	Good manufacturing practice
h	hour
H_2O_2	Hydrogen peroxide
HCl	Hydrochloric acid
HRP	Horseradish peroxidase
Hz	Hertz
ICP-AES	Inductively coupled plasma atomic emission spectroscopy
Ig	Immunoglobulin
IgG	Immunoglobulin G
ILP	Intrinsic loss power
IMS	Industrial methylated spirit
iT	intra-tumoural
K	Anisotropy energy density
k_a	Association rate constant
k_B	Boltzmann constant
K_D	Dissociation constant
k_d	Dissociation rate constant
kDa	kilodalton
$KMnO_4$	Potassium permanganate
l	litre
LS174T	Human colon adenocarcinoma cell line
M	molar
MACH	Magnetic Alternating Current Hyperthermia system
MEM	Minimum Essential Medium
mg	milligram
MHz	mega hertz
min	minute

ml	millilitre
mM	millimolar
MNPs	Magnetic nanoparticles
MPI	Magnetic particle imaging
MRHA	Medicines and Healthcare products Regulatory Agency
MRI	Magnetic resonance imaging
MW	Molecular weight
NA1	Subdomains N and A1 of CEA
NaCl	Sodium chloride
NaOH	Sodium hydroxide
NEAA	Non-essential amino acids
NH_2	amine group
NHS	*N*-hydroxysuccinimide
nm	nanometre
nm-CLD-spio	cross-linked dextran coated nanoparticles from Micromod GmbH
nm-d-spio	dextran coated nanoparticles from Micromod GmbH
o/n	overnight
OD	Optical density
Oe	Oersted, unit of the magnetic field strength
OH	hydroxyl group
OPD	*O*-phenylenediamine dihydrochloride
P. pastoris	*Pichia pastoris*
PAGE	Polyacryliamide gel electrophoresis
PBS	Phosphate buffered saline
PdI	Polydispersity index
PEG	Polyethylene glycol
pH	Negative logarithm of concentration of dissolved hydronium ions
PVDF	Polyvinylidene difluoride
QCM	Quartz crystal microbalance
Resovist	Formulated Ferucarbotran by Bayer-Schering Pharma AG
RGD	Arginine-glycine-aspartic acid peptide
rpm	revolutions per minute
RT	room temperature
SAR	Specific absorption rate
scFv	single-chain fragment variable
SDS	Sodium dodecyl sulphate
SEC	Size exclusion chromatography

shMFEm	Stabilised humanised CEA binding scFv
shMFEm-Cys	Cys tagged stabilised humanised CEA bindin scFv
shNFEm	Stabilised humanised non-CEA binding scFv
SPION	Superparamagnetic iron oxide nanoparticle
SPR	Surface plasmon resonance
SQUID	Superconducting quantum interference device
SW1222	Human colorectal carcinoma cell line
T	Tesla
TBS	Tris-buffered saline
TEM	Transmission electron microscopy
UV	Ultraviolet
V	Volt
VSM	Vibrating sample magnetometer
γ-Fe_2O_3	Maghemite
η	Viscosity coefficient
µl	microlitre
µm	micrometre

Acknowledgements

First of all I would like to thank my supervisors Prof. Kerry A. Chester and Prof. Quentin A. Pankhurst for their encouragement, advice and support throughout my PhD.

Furthermore, I would like to thank everyone I had the opportunity to work with in the Department of Oncology in the past four years, particular those who always had an open ear for even the craziest of my ideas including Kim Vigor, Helen Lowe, Lynda Robson, Jenny Yeung, Enrique Miranda Rota, Berend Tolner, Soraya Diez-Posada, Leena Mukherjee, Maha Abdollah, Gaurav Bhavsar, May Yong, Carima Andrady, Maria Livanos, Robert Goldstein and Tom Oxenham. Thanks also go to Prof. Barbara Pedley, Mathew Robson, Mario Mazzantini, Elisa Cerri, Ethaar El-Emir, Uzma Qureshi and Tammy Kalber for the help with the *in vivo* work and histology.

Additionally, I would like to thank the team at the Royal Institution, especially Nguyen TK Thanh, Daniel Ortega and Steve Nesbitt for always having an open door and helpful discussions; as well as Paul Southern, Kristopher Page, Cristina Blanco-Adujar, Luke A. Green and Samantha Chalker.

Special Thanks also go to Liselotte Kaiser and Staffan Grenklo from Attana for their support, expertise and curiosity to look into completely new ways to use quartz crystal microbalance.

A big Thank You also goes to Julie Olszewski, before last, but not least, I would like to thank my friends and family, especially my mum Brigitte, my husband Dominik and his parents, Roswitha and Oswin for their constant encouragement and for always being there.

Chapter 1

Introduction

Nanoparticles, nanotubes, nanoclusters – 'nano' and nanotechnology are used prevalently, while their true meaning remains a mystery. Most definitions on the topic, found on the web, characterize nanotechnology by the study and control of phenomena and materials at length scales smaller than 100 nm. In the first issue of Nature Nanotechnology, 13 scientists in the field were asked for their definition of nanotechnology and got very different responses (Theis, Parr et al. 2006). Even though there might not be a consensus yet with regard to nanotechnology, there already is a definition for the sub-discipline of nanomedicine – The European Science Foundation in 2004 defined this as the following:

"Nanomedicine is the science and technology of nanometre size scale complex systems, consisting of at least two components, one of which being the active ingredient… In this context, nanoscale should be taken to include active components or objects in the size range from one nanometre to hundreds of nanometres." (ESF 2004)

Following this definition, nanoparticles are small entities between 1 and 1000 nm, varying in composition, shape and effect, dependent on their use. Nanoparticles can be synthesized within a narrow size distribution and specifically 'tuned' to meet the requirements of various applications.

In this thesis, the focus was on magnetic nanoparticles consisting of iron oxide cores surrounded by carbohydrates, such as dextran and it's derivatives or starch, similar to the ones already used in the clinic as contrast agents for magnetic resonance imaging (Reimer and Balzer 2003).

Even though magnetic iron oxide nanoparticles are used clinically, targeting them to specific tissues remains a challenge. Therefore, the aims of this thesis were to identify suitable commercial nanoparticles for hyperthermia application, determine appropriate conjugation chemistry to functionalise them with scFv antibody fragments to enable targeting, purify and verify functionality of the nanoparticle-scFv conjugates, as well as evaluate their therapeutic potential *in vivo.*

This chapter provides the physical background for this thesis, exploring different biomedical applications of magnetic nanoparticles, as well as the role of hyperthermia and its need for a more targeted approach in cancer therapy.

1.1 Magnetic nanoparticles

When materials are taken to the 'nanoscale' their properties change; magnetite, Fe_3O_4, in the form of magnetic iron oxide nanoparticles loses it its magnetic poles and splits into single magnetic magnetic moments with different magnetisation directions giving rise to different magnetic phenomena, such as paramagnetism, superparamagnetism or ferromagnetism (Pankhurst, Connolly et al. 2003; Morup 2010).

1.1.1 Basic Concepts

The origin of magnetism lies in the orbital and spin motions of electrons and how electrons interact with each other. A material's magnetisation strength depends on whether there is collective interaction of these electrons or not and can further be influenced by the atomic structure and also the temperature (Pankhurst, Connolly et al. 2003).

The most common form of magnetism is diamagnetism, as it is a fundamental property of all matter. It is usually very weak and caused by the non-cooperative behavior of orbiting electrons, when a magnetic field is applied. As all orbitals are filled with paired electrons, diamagnetic materials have no net magnetic moment and therefore do not appear magnetic. (Cullity 2008)

Paramagnetism occurs in materials, such as iron, which have a net magnetic moment due to unpaired electrons in partially filled orbitals. So, when subjected to a magnetic field, the magnetic moments in the material align with the direction of the field, resulting in a net positive magnetization and positive susceptibility. However, since thermal energy has a randomization effect in paramagnetic material, when the magnetic field is withdrawn there is no net magnetization. (Pankhurst, Connolly et al. 2003; Cullity 2008)

In ferromagnetism, there is a strong exchange interaction between the atomic moments, which results in a large net magnetization even in the absence of a magnetic field. However, in contrast to what the name suggests, this phenomenon is not limited to iron, but also arises in nickel, cobalt and many of their alloys. When ferromagnetic particles are small enough (below about 20 nm), the magnetization flips randomly under thermal influence resulting in superparamagnetism.

Once the field is withdrawn the magnetic moments quickly 'relax'. The time that this event takes is referred to as relaxation time τ (Pankhurst, Connolly et al. 2003; Cullity 2008) and is described with the following equation:

$$\tau = \tau_0 \exp\left(\frac{KV}{k_B T}\right) \qquad \text{Equation 1.1}$$

where K is the anisotropy energy density, V is the particle volume and k_BT, the thermal energy, Boltzmann constant k_B (1.38 x 10^{-23} J K^{-1}) multiplied by the absolute temperature T (Pankhurst, Connolly et al. 2003).

Superparamagnetic behaviour is strongly size dependent and in magnetite observed at sizes <20 nm hydrodynamic diameter (Pankhurst, Connolly et al. 2003; Hofmann-Amtenbrink 2009) and a core size <5 nm (Krishnan 2010).

As previously stated, thermal energy aims to randomize particles, where a magnetic field applies a torque on the particles to align with the field. While the thermal energy is the same for all particles, the magnetic torque is smaller for smaller particles. This behavior of the nanoparticles is described in the Langevin function:

$$L(\alpha) = \coth\alpha - \frac{1}{\alpha} \qquad \text{Equation 1.2}$$

$$\alpha = \frac{\mu_0 m H}{k_B T} \qquad \text{Equation 1.3}$$

where μ_0 is the permeability of free space (4π x 10^{-7} N A^{-2}), m is the dipole moment, H the magnetic field strength, k_B is the Boltzmann constant and T the absolute temperature. (Rosensweig 1997)

These unique behaviours of magnetic nanoparticles have given rise to a number of biomedical applications.

1.1.2 Biomedical Applications

Biomedical applications of magnetic particles can be divided in four main categories: imaging, drug delivery, gene transfection and hyperthermia

1.1.2.1 Magnetic Resonance Imaging (MRI)

The best know application of magnetic nanoparticles is MRI. It exploits the small magnetic moment on a proton, such as the hydrogen nuclei, and its large number [6.6 x 10^{19}/mm^3 water (Pankhurst, Connolly et al. 2003)] present within the human body. When subjected to a static field, only a tiny fraction of protons will align in parallel to the field applied. However since there are so many, this response can be measured. This is achieved through an alternating magnetic field set at the frequency to flip the magnetic moment of the proton. This field is orientated perpendicular to direction of the static field and applied in pulses, to allow for just enough time to capture the re-alignment of the spins with the static field. (Lepage 2004)

There are two types of relaxation times: longitudinal relaxation, T_1, involving the proton releasing absorbed energy to the surrounding tissue and transverse relaxation, T_2, involving the exchange of energy between spinning protons (Pankhurst, Connolly et al. 2003). These relaxation times can be reduced by the use of magnetic contrast agents (Lin and Brown 2007), such as Resovist® (Reimer and Balzer 2003).

Superparamagnetic nanoparticles are magnetically saturated in a static field and thereby generating a dipolar field, causing a shortened relaxation time. (Pankhurst, Connolly et al. 2003)

The most commonly used MRI contrast agents in the clinic currently include paramagnetic gadolinium complexes Magnevist®, Gadovist® (Pintaske, Martirosian et al. 2006) or Primovist™ (Hammerstingl, Huppertz et al. 2008) to improve T_1 relaxation, and ultrasmall superparamagnetic iron oxide nanoparticles (USPIO), such as Supravist™ (Simon, von Vopelius-Feldt et al. 2006), to improve T_2 relaxation.

One of the most exciting developments in MRI contrast agents is magnetic block ionomer clusters (MBIClusters). Carroll *et al* showed that magnetite nanoparticles coated with copolyethers, when “clustered” increased their T_2 relaxivities and were 1.7 times better than commercial contrast agent Feridex® (Carroll, Huffstetler et al. 2011). Recently they went one step further and demonstrated that the model drug gentamicin, an antibiotic, could be incorporated in the clusters without affecting the high MRI sensitivity of the MBIClusters; combining imaging with drug delivery (Pothayee 2013).

1.1.2.2 Magnetic Particle Imaging

In 2005, Gleich and Weizenecker, presented a completely new imaging modality – magnetic particle imaging (MPI). Hereby an alternating magnetic field is applied to nanoparticles resulting in a non-linear magnetization. A static field is superimposed on the oscillating field, so the nanoparticles remain in their maximum magnetization. However, this static field is provided by two antiparallel coils generating a field free point (FFP) enabling the detection of the changing magnetization (harmonics) caused by the alternating magnetic field (Gleich and Weizenecker 2005).

In their first experiments, Resovist® was used, but only a small fraction of particles demonstrated the desired harmonics calling for specifically designed nanoparticles (Biederer, Knopp et al. 2009). Since then first *in vivo* studies have been performed (Weizenecker, Gleich et al. 2009), new scanners developed (Sattel, Knopp et al. 2009) and currently the focus lies on improving particle designs (Eberbeck, Wiekhorst et al. 2011; Ferguson, Minard et al. 2011) and reconstruction (Goodwill and Conolly 2011; Lampe, Bassoy et al. 2012).

1.1.2.3 Implant-assisted Magnetic Targeting

One of the biggest challenges in coronary disease is in-stent thrombosis. Therefore Kempe and Kempe (Kempe and Kempe 2010) proposed the combination of a magnetisable stent with magnetic nanoparticles carrying the tissue plasminogen activator (tPA) for thrombolysis and a static magnetic field. The static magnetic field induces magnetic field gradients within the stent and enables targeting of the tPA loaded nanoparticles, in order to break down blood clots. First results from *in vivo* pig experiments are promising.

1.1.2.4 Magnetic Pushing

Permanent or electromagnets attract magnetic particles and so the majority of magnetic systems are based on this fact. However, in order to direct magnetic nanoparticles to the inner ear or the back of the eye, incredibly strong magnets would have to be used due to the exponential decay of magnetic field strength with distance from the magnet. Therefore, Sarwar *et al.* developed a magnetic system, consisting of just two permanent magnets arranged at an angle (Fig. 1.1), to push nanoparticles and enable treatment of inner-ear diseases, such as tinnitus (Sarwar, Nemirovski et al. 2012; Sarwar, Lee et al. 2013).

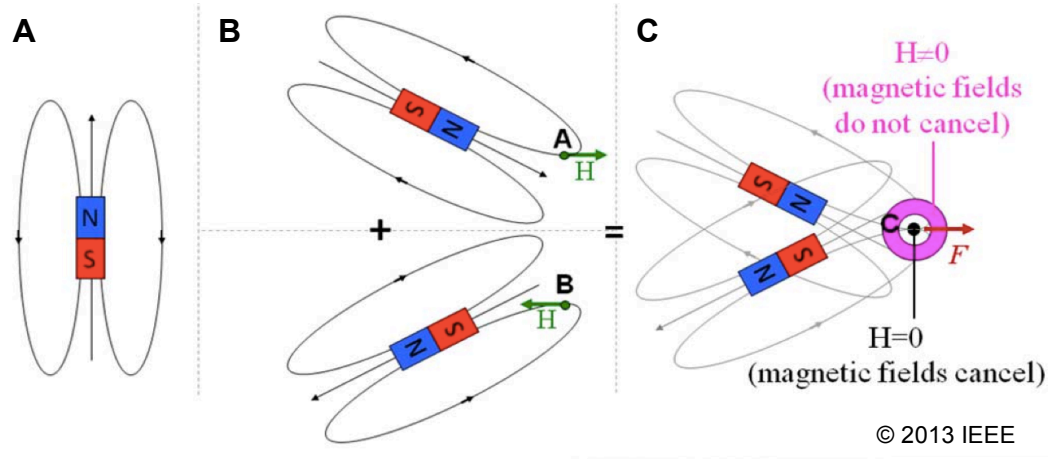

Fig. 1.1 Two permanent magnets can push particles away. A) Schematic field lines around a single magnet. B) Two magnets oriented, so that their polarity is reversed. C) When these two magnets are correctly overlaid their magnetic fields add to exactly cancel at the node point C (big black dot), but they do not cancel around that point (purple ring) thus forces go outward enabling pushing. (Sarwar, Lee et al. 2013) [Reprinted, with permission from Sarwar, Lee et al., Magnetic injection of nanoparticles into rat inner ears at a human head working distance, IEEE Transactions on Magnetics, 2013]

1.1.2.5 Magnetofection

Another important biomedical application of magnetic nanoparticles is magnetic transfection for gene delivery, also known as magnetofection. Nucleic acids and cationic lipids or polymers are associated with superparamagnetic nanoparticles and accumulated on the surface of target cells by applying a magnetic field (Plank, Schillinger et al. 2003). This set-up leads to substantially improved *in vitro* transfection efficiencies compared with nonmagnetic gene vectors (Mykhaylyk, Antequera et al. 2007), which was even further enhanced by mechanical stimulation through the use of oscillating magnet arrays and pulsed electromagnets (McBain, Griesenbach et al. 2008).

1.1.2.6 Magnetic Microbubbles for Drug Delivery

A different approach using magnetic nanoparticles for gene delivery combines magnetofection with ultrasound and nanoparticle loaded microbubbles (Stride, Porter et al. 2009). However, this technique is not only interesting for transfection, but also drug delivery and imaging.

Bubbles are interesting delivery vehicles. Depending on the design, nanoparticles or drugs can be incorporated in the coating or loaded within the bubble itself, while depending on the acustic field applied different physical effects, such as microjetting

may improve drug delivery opening an array of possibilities (Stride and Coussios 2010; Owen, Pankhurst et al. 2012).

1.1.2.7 Magnetic Actuation

Magnetic manipulation of cell surface receptors is a relatively new procedure of interest not only for tissue engineering, but also therapeutic applications. There are different approaches for magnetic actuation, as shown in Figure 1.2. In general nanoparticles are conjugated with targeting moieties specific to certain cell surface proteins. The cells are incubated with the nanoparticle conjugates before actuation is initiated through the application of magnetic field, such as provided by a magnetic needle. Magnetic actuation can enable transduction either through twisting of the particles by applying a magnetic torque (magnetic twisting cytometry); open ion channels through pulling on the membrane (mechanosensitive ion-channel activation); manipulating a channel with a nanoparticle directly (targeted ion-channel activation) or by clustering receptors. (Dobson 2008)

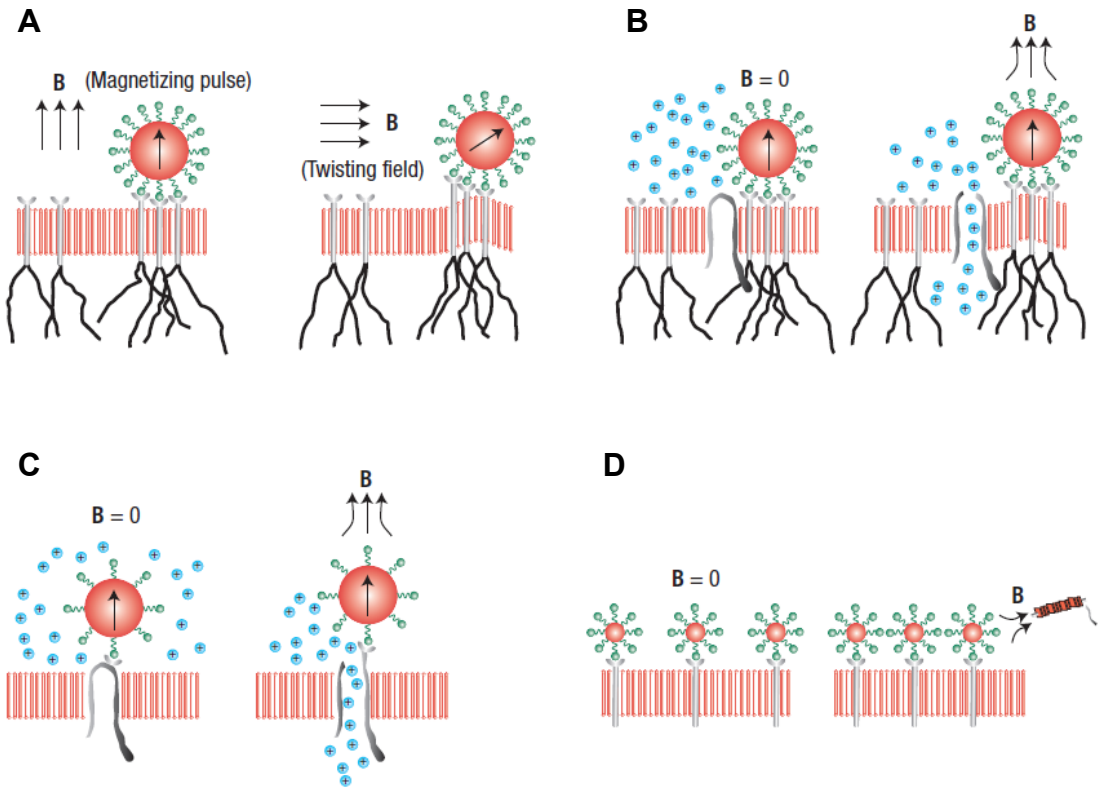

Fig. 1.2 Different types of magnetic actuation: Magnetic twisting cytometry (A); Mechanosensitive ion-channel activation (B); Targeted ion-channel activation (C); Receptor clustering (D) (Dobson 2008) [Reprinted, with permission from Dobson, Remote control of cellular behaviour with magnetic nanoparticles, Nature Nanotechnology, 2008]

Mannix *et al.* presented another mechanism involving receptor clustering (Mannix, Kumar et al. 2008), whereby superparamagnetic nanoparticles were coated with monovalent ligands and bound to transmembrane receptors. The presence of a magnetic field causes clustering between nanoparticles, but also between the bound receptors, directly inducing a signalling cascade. Cho *et al.* adapted this idea *in vivo* and recently demonstrated initiation of apoptosis in the tail region of zebrafish embryo, by targeting and clustering the TNF-related apoptosis inducing ligand (TRAIL) (Cho, Lee et al. 2012).

1.2 Hyperthermia in Cancer Therapy

Magnetic fluid hyperthermia, another biomedical application of magnetic nanoparticles, is of particular interest in cancer therapy, as other forms of hyperthermia are already in use.

1.2.1 Hyperthermia in Cancer Therapy

In the literature conventional hyperthermia refers to temperatures used between 40 and 44 °C, while thermal ablation discusses temperatures above 50 °C (van der Zee 2002; Chichel 2007).

The rational behind using hyperthermia in cancer therapy is that cells are more susceptible to temperatures between 40 to 44 °C under low pH and low oxygen conditions, which can be found in necrotic regions of tumours, due to poor vascularisation and blood supply (Otte 1988). These cells can enter the G_0 phase of the cell cycle rendering them resistant to most cytostatic drugs, while cells in the S phase are mostly resistant to radiation, but also most susceptible to heat (Hildebrandt and Wust 2007). Therefore hyperthermia has a cytotoxic effect on radioresistant cells at temperatures above 42 °C. While at lower temperatures between 39.5 °C and 40.5 °C, the heating improves vascularisation increasing the oxygen supply and thus sensitizes them to radiation. (van der Zee 2002)

In chemotherapy depending on the temperature and length of the treatment hyperthermia has the potential to enhance the blood supply within the tumour and enabling improved delivery of cytostatic drugs (Otte 1988; Hildebrandt and Wust 2007).

1.2.2 Clinical Hyperthermia

The parts of the body that receive hyperthermic treatment, such as whole-body, partial and local hyperthermia, distinguish the different kinds of hyperthermia used in the clinic.

Whole-body hyperthermia aims to achieve a body temperature of 41.8 to 42 °C by using wax baths, thermal chambers, hot water blankets, infrared radiators or extracorporeal circulation in order to treat metastatic cancers such as melanoma (Otte 1988; van der Zee 2002; Wust, Hildebrandt et al. 2002).

Partial or regional hyperthermia for deep seated tumours or locally advanced cancer is often achieved through isolated perfusion or the use of external applicators, antennas emitting microwave or radiofrequencies. The main advantage of this approach over whole-body hyperthermia is less systemic side effects, however burns and other side effects are reported (van der Zee, Gonzalez et al. 2000).

Local hyperthermia, the most frequently used, originally was distinguished by the method inducing the heat, like microwave (0.3 - 6 MHz), ultrasound (50 - 2450 MHz) or radiofrequency hyperthermia (Otte 1988). More recent hyperthermia treatments involving nanoparticles include last near-infrared photothermal therapy, radiofrequency ablation and magnetic nanoparticle hyperthermia (Day, Morton et al. 2009).

1.2.2.1 NIR Photothermal Therapy

In near-infrared photothermal therapy gold-silica nanoshells are injected intravenously. Due to the leaky vasculature of the tumour they tend to accumulate in the tumour, where they are excited with a near infrared light source. The absorption of this near infrared light, between 700 nm and 900 nm, leads to generation of heat and irreversible tissue damage. (Gobin, Lee et al. 2007)

1.2.2.2 Radiofrequency Ablation

Radiofrequency ablation on the contrary relies on the administration of radiofrequency irradiation. Therefore an electrode is inserted into the tumour to apply a radiofrequency current, which leads to frictional heating (Curley 2001). The conductivity of gold nanoparticles and single-walled carbon nanotubes allow more efficient and non-invasive radiofrequency heating (Gannon, Cherukuri et al. 2007; Gannon, Patra et al. 2008).

1.3 Magnetic Nanoparticle Hyperthermia

Magnetic nanoparticle or magnetic fluid hyperthermia was first proposed in 1957 by Gilchrist *et al.* as a new method to destroy cancer in lymph nodes by injecting them with 'particulate matter' of γ-Fe_2O_3 before applying an alternating magnetic field (Gilchrist, Medal et al. 1957)

Even though this concept has been known, it was not until the early 1990s that it was rediscovered and explored in combination with other treatments. Only recently, the European Medicines Agency (EMA) approved magnetic nanoparticle hyperthermia for the treatment of glioblastoma multiforme (Maier-Hauff, Ulrich et al. 2011). While approval by the US Food Drug Administration (FDA) is still pending, there are several clinical trials exploring magnetic fluid hyperthermia for several different cancers, such as glioblastoma, prostate and pancreatic cancer (Johannsen, Gneveckow et al. 2007; Johannsen, Gneveckow et al. 2007; van Landeghem, Maier-Hauff et al. 2009; Maier-Hauff, Ulrich et al. 2011).

1.3.1 Magnetic Fields, Hysteresis and Relaxation Times

As magnetic nanoparticles are placed in an alternating magnetic field, they heat due to different magnetic losses within the particle: Hysteresis, Néel relaxation and Brownian motion (Hergt, Dutz et al. 2006). Eddy current induced heating, due to the size of the nanoparticles, is negligible (Rosensweig 2002).

1.3.1.1 Hysteresis

When a magnetic material is subjected to a magnetic field, each magnetic moments in the material contributes to the overall response also known as magnetic induction B, which is given by

$$B = \mu_0(H + M) \qquad \text{Equation 1.4}$$

where the magnetic field intensity H, generated in the centre of a current loop, is measured by A m^{-1}; the magnetization (intensity) M expressed as M = m/V is the magnetic moment m per unit volume V, which, like H, is also measured by A m^{-1} and the permeability of free space μ_0. (Rosensweig 2002; Pankhurst, Connolly et al. 2003)

The magnetization M can also be expressed as

$$M = \chi H \qquad \text{Equation 1.5}$$

where χ is the dimensionless susceptibility, which is not only dependent on M and H (as indicated in the function above, but also on temperature). However, H accounts for the typical sigmoidal shape of the MH curve.

If a ferro- or ferrimagnetic material is placed in a magnetic field the magnetic moments within the material align with the direction of the applied field. When the magnetic field is withdrawn, some magnetic moments due the crystalline anisotropy will still retain this alignment for an indefinite amount of time; the magnetization is irreversible. Only the application of magnetic field in the reversed direction will lead to a partial demagnetization. Therefore a typical MH curve for this kind of material will result in a more open hysteresis loop (Pankhurst, Connolly et al. 2003).

1.3.1.2 Néel Relaxation

In small magnetic nanoparticles (below 20 nm) the magnetic moments flip randomly under the influence of temperature. The time it takes for a nanoparticle system to flip the magnetic moment across the anisotropy barrier is given by the Néel relaxation time τ_N

$$\tau_N = \tau_0 \exp\left(\frac{\Delta E}{k_B T}\right) \qquad \text{Equation 1.6}$$

where τ_0 is the attempt time ($\tau_0 \approx 10^{-9}$ sec), ΔE is the anisotropy energy and $k_B T$ is the thermal energy: the product of the Boltzmann constant k_B (1.38×10^{-23} J K^{-1}) and absolute temperature T (Hergt, Dutz et al. 2006). The anisotropy energy ΔE can also be described as anisotropy energy density K times the particle V, this is also the reason why ΔE and therefore the Néel relaxation effect gets more and more important as the particle size decreases and superparamagnetism arises (Pankhurst, Connolly et al. 2003).

1.3.1.3 Brownian Motion

If the magnetic moment is fixed to the easy axis within the particle, when placed in a magnetic field, not only the moment aligns with the direction of the field, but also the whole particle rotates, commonly referred to as Brownian motion

$$\tau_B = \frac{3\eta V_H}{k_B T}$$ Equation 1.7

where η is the viscosity coefficient of the fluid surrounding the particle, V_H is the hydrodynamic volume or diameter and the thermal energy $k_B T$. (Rosensweig 2002; Hergt, Hiergeist et al. 2004)

Therefore the Brownian motion describes the actual rotation of the particle in the fluid in contrast to Néel relaxation the flipping of the magnetic moment within the particle without actual movement of the nanoparticle.

1.3.1.4 Effective Relaxation

During hyperthermia in a magnetic fluid with a narrow size distribution (PdI <0.1) the faster relaxation mechanism (Néel relaxation or Brownian motion) will dominate and therefore the effective relaxation time can be described by (Hergt, Andra et al. 1998)

$$\tau_{eff} = \frac{\tau_N \tau_B}{(\tau_N + \tau_B)}$$ Equation 1.8

Since most magnetic nanoparticle suspensions have a normal distribution of sizes, both Néel relaxation and Brownian motion will contribute to the heating of the fluid in the presence of an alternating magnetic field leading to the effective relaxation time (Rosensweig 2002).

$$\frac{1}{\tau} = \frac{1}{\tau_B} + \frac{1}{\tau_N}$$ Equation 1.9

The overall power dissipation of particle is described by

$$P = \mu_0 \pi \chi''(f) f H^2$$ Equation 1.10

where μ_0 is the permeability of free space, χ" is the imaginary susceptibility, f the frequency and H field strength of the applied field (Rosensweig 2002; Kallumadil, Tada et al. 2009).

1.3.1.5 Specific Absorption Rate (SAR) and Intrinsic Loss Power (ILP)

In order to compare heating rates of different magnetic nanoparticles, in the literature it is often referred to the specific loss power (SLP) or specific absorption rate (SAR) given in W/g (Ma, Wu et al. 2004; Hergt, Dutz et al. 2006).

$$SAR = c\frac{m_{sample}}{m_{ironoxide}}\frac{\Delta T}{\Delta t} \qquad \text{Equation 1.11}$$

where *c* is the heat capacity of water, m_{sample} is the mass of the sample, $m_{ironoxide}$ is the mass of iron oxide in the sample measured magnetically and $\Delta T/\Delta t$ is the slope of the time dependent heating curve (Krishnan 2010)

However, instead of reflecting the heating potential of a MNP suspension, the SAR value depends mostly on external factors such as frequency and strengths of the magnetic field applied and therefore will vary for the same sample in different magnetic fields.

So in 2009, Kallumadil *et al* (Kallumadil, Tada et al. 2009) introduced the concept of intrinsic loss power (ILP), where SAR is normalized against frequency *f* and magnetic field strength *H*, which allows the direct comparison of heating potential of MNPs, by different groups using different magnetic field parameters. As the units for field strength *H* and frequency *f* are kA/m and kHz, ILP is measured in nH m^2 kg^{-1}.

$$ILP = \frac{SAR}{H^2 f} \qquad \text{Equation 1.12}$$

1.4 Need for Targeting

A major issue with non-targeted treatment modalities is their specificity. Systemic injection of drugs often leads to unwanted side effects and limits their efficacy. Therefore, over a hundred years ago Paul Ehrlich introduced the 'magic bullet concept', proposing drugs moving directly to their intended cell-structural target. (Strebhardt and Ullrich 2008)

In magnetic nanoparticle hyperthermia the particles are either injected systemically or directly into the tumour, where the particles accumulate due to the leaky vasculature. This passive targeting approach however proves not to be very effective, as particles are rapidly cleared from the system, by uptake in reticuloendothelial system and

consequently in liver and spleen, which makes them a good contrast in magnet resonance imaging (MRI) for the diagnosis of liver tumours (Reimer and Balzer 2003).

Therefore, in the last years researchers focused on improving the stealth of the coating with polymers, such as polyethylene glycol (PEG) (Gref, Luck et al. 2000) (Khalid, Simard et al. 2006), but also to target nanoparticles by the attachment of antibodies (Kirpotin, Drummond et al. 2006).

1.4.1 Antibodies

Antibodies, also known as human immunoglobulins (IgG, IgM, IgA, IgE) are highly specific targeting molecules and the first line of defense of our immune system. The main serum antibody, the Y-shaped IgG (see Fig. 1.3) consists of two heavy and two light peptide chains, connected by disulphide bridges, together forming two antigen-binding arms with the Fc region for effector function (Edelman 1973). The variable region, Fv, contains the complementary determining regions (CDR), which define the binding specificity of the antibody.

First identified by Kabat and Tiselius (Tiselius and Kabat 1939) in the late 1930s, it was not until the development of the hybridoma technology that this field of antibodies gained momentum. By fusing mouse B cell clones with immortalised mouse myeloma cells generating hybridomas, Köhler and Milstein were the first to enable mass production of specific monoclonal antibodies (Kohler and Milstein 1975). However, due to their murine origin, these antibodies induced human anti-mouse antibodies (HAMA), when used in humans (Tjandra, Ramadi et al. 1990). This resulted in a shortened blood half life and lower treatment efficacy.

In order to overcome the immunogenicity of the murine antibodies, chimeric and humanised antibodies were developed. So, as to generate a chimeric antibody, the entire murine variable regions were fused into the human IgG (Adams and Weiner 2005), while for the humanised antibody only the CDR were engineered into the human IgG (Jones, Dear et al. 1986). These developments gave rise to first monoclonal antibodies to receive FDA approval: Rituximab (Rituxan), a chimeric antibody for the treatment of B-cell non-Hodgkin's lymphoma and Trastuzumab (Herceptin), a humanised anti-HER2/*neu* antibody for breast cancer therapy (Adams and Weiner 2005) – marking a major milestone in cancer therapy (Chabner and Roberts 2005).

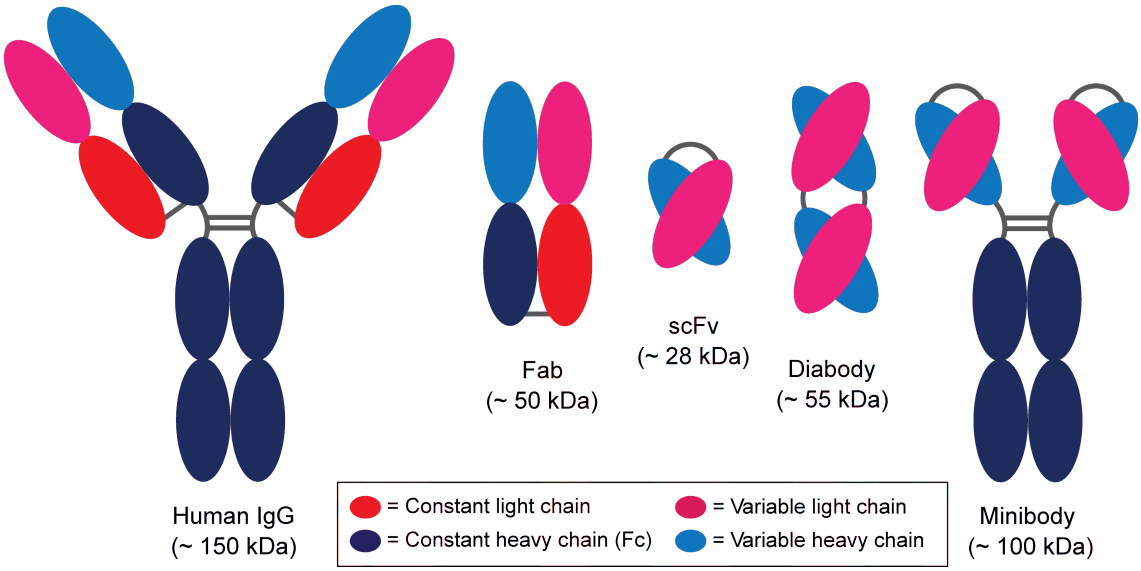

Fig. 1.3 Schematic structure of human IgG and derived antibody fragments (Kozissnik 2012) [Reprinted, with permission from, Thanh, Magnetic Nanoparticles: From Fabrication to Clinical Applications, CRC Press, 2012]

Consequently, to improve their therapeutic potential antibodies were linked to cytotoxic drugs, toxins or radionucleotides (Scott, Wolchok et al. 2012). Additionally in order to enhance penetration and tumour concentration smaller formats, such as shown in Figure 1.3, are under investigation with the most prominent being the scFv (Holliger and Hudson 2005).

1.4.2 Single chain Fv (scFv)

The single chain Fv antibody fragment, with a size of 28 kDa, consists of one variable heavy chain and one variable light chain, connected only through a flexible polypeptide linker to prevent dissociation (Holliger and Hudson 2005). The small size allows scFvs to penetrate tumours much quicker than whole IgG, as scFv are easily selected for almost any target using page display and recombinant antibody technology (Ahmad, Yeap et al. 2012) and generated in high quantities through in non-mammalian expression systems, such as yeast, *Pichia pastoris* (Tolner, Smith et al. 2006). This not only makes them a prime target for potential clinical application, but also the moiety of choice for the targeting of magnetic nanoparticles in this thesis.

1.4.3 Functionalisation Chemistries

In order to attach scFv or other molecules to magnetic nanoparticles effective functionalisation chemistry has to be formulated. This is dependent on both, the functional groups available on the surface of the nanoparticles and the accessible groups present within the scFv. In proteins, the functional groups are typically amines provided by lysines, while the functional groups available on the nanoparticles are dependent on the polymer coating (Kozissnik 2012), such as carboxydextran shown in Figure 1.4.

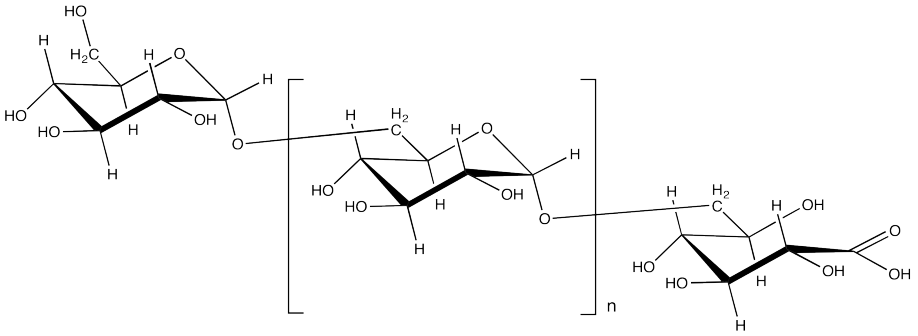

Fig. 1.4 The chemical structure of carboxydextran offers two options for attachment, multiple hydroxyl groups and one carboxyl group.

1.4.3.1 Carbodiimide Coupling

The most prevalent conjugation chemistry is carbodiimide coupling of a carboxylic acid to an amine using 1-ethyl-3-(dimethylaminopropyl)carbodiimide (EDC) in combination with *N*-hydroxysuccinimide (NHS). Even though an amide bond can be formed directly between carboxyl and amine group, NHS is added to enhance the reaction efficiency by stabilising the *O*-acylisourea intermediate through the formation of a succinimide ester (Hermanson 2008) as demonstrated in Figure 1.5.

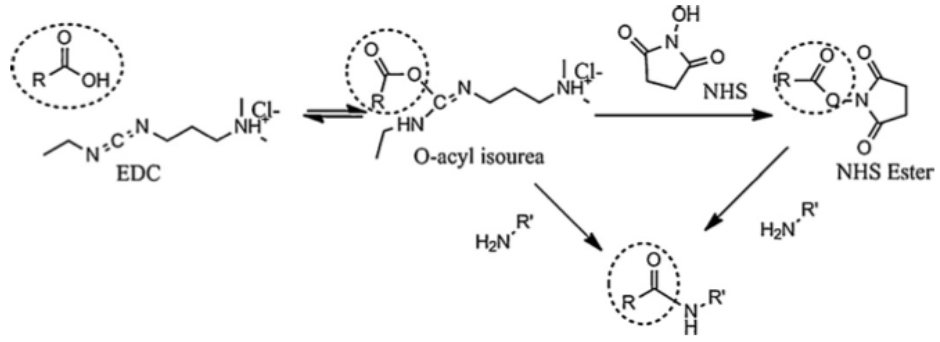

Fig. 1.5 Schematic representation of carbodiimide coupling of a carboxylic acid residue to an amine using EDC and NHS (Thanh and Green 2010) [Reprinted, with permission from, Thanh and Green, Functionalisation of nanoparticles for biomedical applications, NanoToday, 2010]

1.4.3.2 Cyanogen Bromide Conjugation

Since carboxydextran provides numerous hydroxyl groups cyanogen bromide conjugation can be used instead of the carbodiimide coupling.

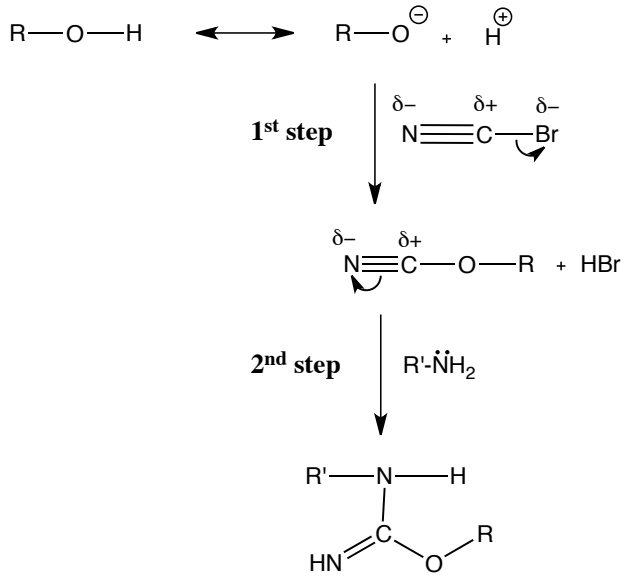

Fig. 1.6 Schematic representation of cyanogen bromide conjugation of an amine to a hydroxyl using cyanogen bromide (CNBr) to first form a cyanate ester and consequently an isourea bond with the ligand (Kozissnik 2012) [Reprinted, with permission from, Thanh, Magnetic Nanoparticles: From Fabrication to Clinical Applications, CRC Press, 2012]

The reaction occurs in two steps (see Fig. 1.6): First the nucleophilic hydroxyl group attacks the electron deficient carbon and reduces the bromine to hydrogen bromide. In a second step a nucleophilic addition of the amine to the electron-deficient cyanide group forms an isourea bond. (Kozissnik 2012)

1.4.3.3 Further Challenges

Even though the field of magnetic nanoparticle hyperthermia has seen important advances in recent years, achieving a sufficient concentration within the target tumour still remains as a challenge. Many *in vivo* studies in the past relied on direct local delivery (Jordan, Scholz et al. 1997, Johannsen, Gneveckow et al. 2007) rather than systemic delivery.

Direct injection was also the route of administration used in the first clinical trial with magnetic nanoparticle hyperthermia for the treatment of glioblastoma multiforme (Maier-Hauff, Ulrich et al. 2011).

In this study, under anaesthesia, the patients were injected with semi-passively targeted aminosilane coated iron oxide nanoparticles (0.28 ml magnetic fluid per cm^3 of tumour volume) and treated with thermotherapy for 1 hr in six semi-weekly sessions. Additionally, the patients received radiotherapy (30 Gy in 5 x 2 Gy/week) before or after the intratumoural therapy sessions.

The results showed an improvement in overall survival of the patients and lead to the clinical approval of magnetic nanoparticle hyperthermia for the treatment of glioblastoma multiforme by the European Medicines Agency (EMA).

Although this study represents an important milestone, it remains quite controversial. Soon after its results were published in the Journal of Neurooncology, a 'letter to the editor' scrutinised the set-up of the clinical trial, as the patients were not randomised and had received different courses of treatment for their cancer before being admitted into this clinical study. Additionally, the authors of the article also critised that prior to treatment, for safety reasons, all dental fillings, crowns and implants of the patients had to be removed, not aiding the quality of life perspective of the patient. (Weller, Wick 2011)

In order to move magnetic nanoparticle hyperthermia forward, nanoparticles have to be actively targeted through the attachment of a targeting moiety, such as scFv antibody fragments, potentially limiting the side effects and therefore improving the quality of life of cancer patients.

1.5 Research Aims

The central hypothesis for this thesis is that antibody targeted superparamagnetic iron oxide nanoparticles subjected to an alternating magnetic field can be used to generate hyperthermia *in situ* and therefore have the potential to achieve localised hyperthermic cancer treatments.

Therefore, Chapter 2 outlines the key methods and materials used in this thesis. This includes the selection of appropriate techniques for the characterisation of the nanoparticles, as well as the scFv antibody fragments, the functionalisation of the nanoparticles with the scFv antibody fragments, the purification and characterisation of the SPION-scFv conjugates and the antibody targeted magnetic nanoparticle hyperthermia *in vivo*.

Chapter 3 provides a detailed property analysis of different commercial nanoparticles determining characteristics, such as hydrodynamic diameter, zeta potential, core structure, atomic iron content and heating potential in order to identify the best nanoparticle for hyperthermia application.

Chapter 4 investigates the functionalisation of this nanoparticle with scFv antibody fragments evaluating different conjugation chemistries and purification techniques. Another focus in this chapter is the characterisation and verification of the functionality of the SPION-scFv conjugates.

Chapter 5 explores the therapeutic potential of the SPION-scFv conjugates *in vivo*.

Chapter 6 provides a detailed discussion of the results presented in the preceeding chapters, while Chapter 7 focuses on the challenges ahead.

Chapter 2

Materials and Methods

2.1 Introduction

The aim of this thesis was to investigate the potential of magnetic nanoparticles (MNP) to deliver targeted hyperthermia for the treatment of tumours. The work described in this chapter was to find suitable commercially available MNP candidates for hyperthermia, as well as appropriate techniques for the characterisation, functionalisation and hyperthermia application *in vivo*.

In order to ensure biocompatibility, most of the MRI contrast agents, such as Endorem® or Resovist®, were coated in dextran or dextran derivatives (Laniado and Chachuat 1995; Riemer, Hoepken et al. 2004). Therefore unformulated Resovist® (Ferucarbotran) and seven commercially available and dextran coated iron oxide nanoparticles were chosen with a hydrodynamic diameter between 50-100 nm.

Particles with sizes between 50-70 nm have been shown to have a better half life in the blood than similar nanoparticles of a larger size due to their rapid clearance by the reticuloendothelial system (RES) (Kalber, Smith et al. 2005; Boyer, Whittaker et al. 2010; Ruoslahti, Bhatia et al. 2010). The rationale behind this is that a longer half life will allow for more particles to accumulate in the tumour due to the enhanced permeability and retention (EPR) effect (Greish 2010) and are therefore potentially better suited for hyperthermia application.

Even though a smaller hydrodynamic diameter of the magnetic nanoparticles would potentially benefit hyperthermia, as especially below the size of 20 nm, as it would encourage Néel relaxation. However, an ideal core diameter between 11-15 nm (Gonzales-Weimuller, Zeisberger et al. 2009), depending on the magnetic field strength and frequency, leaves little space for coating and functionalisation. Additionally, since the coating to iron ratio is higher, a substantially higher concentration of magnetic nanoparticles would be necessary.

2.2 Objectives

The objectives of the research described in this chapter were to:

1. Identify suitable commercial nanoparticles
2. Determine appropriate techniques for the
    a. Study of properties of the nanoparticles
    b. Characterisation of the scFv antibody fragments
    c. Functionalising nanoparticles with scFv antibody fragments
    d. Purification and characterisation of SPION-scFv conjugates
    e. Antibody targeted magnetic nanoparticle hyperthermia *in vivo*

2.3 Materials

2.3.1 Nanoparticles

Details of the SPIONs investigated are shown in Table 2.12, as provided by the supplier in the specifications.

Table 2.1: Details of SPIONs investigated

Commercial Name	Supplier	Coating	Particle Conc. [mg/ml]
fluidMAG-DX 50 nm	Chemicell GmbH	Dextran	100
fluidMAG-DX 100 nm	Chemicell GmbH	Dextran	25
fluidMAG-CMX 100 nm	Chemicell GmbH	Carboxymethyldextran	25
fluidMAG-DXS 100 nm	Chemicell GmbH	Dextran-sulfate	25
nanomag-D-spio 100 nm	Micromod GmbH	Dextran	25
nanomag-CLD-spio 100 nm	Micromod GmbH	Cross-linked dextran with NH_2 groups	5
BNF-starch 100 nm	Micromod GmbH	Starch	25
Ferucarbotran	Meito-Sangyo Co Ltd	Carboxylated dextran	N/A*

[* The manufacturer only provided the atomic iron concentration]

2.3.2 Human Cell Lines

The human cell lines A375M – melanoma, SW1222 – colorectal carcinoma, and LS174T – human colorectal adenocarcinoma, were purchased from ECACC, the European Health Protection Agency Culture Collections, while Capan-1 – human pancreatic adenocarcinoma, were acquired through ATCC, the American Type Culture Collection.

2.3.3 Proteins

Carcinoembryonic antigen (CEA) was obtained in from Sigma-Aldrich, while NA1 subunits of CEA were purified as described by Sainz-Pastor *et al.* (Sainz-Pastor, Tolner et al. 2006)

2.3.4 Antibodies

ScFv variants shMFEm, shNFEm and shMFEm-Cys were produced using the methanol inducible *Pichia pastoris* production platform with secretion of the target protein into the media (Tolner, Smith et al. 2006). Briefly, linearized plasmids encoding the respective proteins were introduced into *Pichia pastoris X33* (Invitrogen)

by electroporation and clones were selected on 100 µg/ml zeocin. Out of 5-10 clones the best scFv expressing cell-line was chosen and taken forward for fermentation (Tolner, Smith et al. 2006). Radial flow bed adsorption IMAC was used as primary capture step (Tolner 2013), followed by a cross-flow concentration step. Finally, the protein was purified using size exclusion chromatography. The fraction containing the monomer scFv was collected and stored at -80 °C

Mouse tetra his (anti-His) antibody was purchased from Qiagen (Crawley, UK). Mouse anti-dextran antibody was bought from StemCell Technologies (Vancouver, Canada). Sheep anti-mouse HRP antibody was obtained from Invitrogen (Oregon, US). Rabbit cleaved caspase-3 antibody and rabbit HSP70 antibody were purchased from Cell Signaling Technology (Massachusetts, US). Goat anti-rabbit HRP antibody was kindly provided by Dr. Barbara Pedley (UCL Department of Oncology)

Further materials, as well as buffer recipes, can be found in Appendix I.

2.4 Methods

2.4.1 Nanoparticle Characterization

2.4.1.1 Hydrodynamic Diameter

The hydrodynamic diameter was determined by dynamic light scattering using a Zetasizer Nano ZS90 (Malvern, Worcestershire, UK).

Nanoparticles taken from a sample stock were diluted with dH_2O to a concentration of 100 µg particles/ml. 750 µl nanoparticle suspension were transferred to a disposable semi-micro UV-cuvette (Brand, Wertheim, DE), inserted into the Zetasizer Nano ZS90 and measured. After three measurements the cuvette was removed from the instrument and discarded.

Next nanoparticles from the same original sample were diluted with 5 mM NaCl to a concentration of 100 µg particles/ml. 750 µl of the resulting nanoparticle suspension were added to a fresh disposable semi-micro UV-cuvette, inserted and measured three times. Consequently nanoparticles from the same sample stock were diluted in PBS and measured. This procedure was repeated for all eight nanoparticle samples.

2.4.1.2 ζ-Potential

The ζ-potential was determined using a Zetasizer Nano ZS90 (Malvern).

A disposable folded capillary cell (Malvern) was washed with a 10 ml syringe containing 70% IMS, followed by two washes with 10 ml dH_2O each. Subsequently most of the liquid was forced out with nitrogen gas. Next 0.2 mg nanoparticles were suspended in 1 ml 5 mM NaCl and added to the folded capillary cell. The cell was sealed off with the stoppers provided, inserted into the Zetasizer Nano ZS90 (Malvern) and measured. After three series of measurements the folded capillary cell was removed, emptied and washed with 70% IMS and dH_2O, as previously described. The capillary cells were re-used for multiple nanoparticle samples until deposits on the electrodes started to appear.

2.4.1.3 Atomic Iron Content

The atomic iron content was determined using inductively coupled plasma atomic emission spectroscopy (ICP-AES).

Nanoparticles taken from a sample stock were diluted with ultrapure H_2O to a concentration of 100 µg particles/ml. The nanoparticle suspensions were further diluted with Aristar grade concentrated HCl. The beakers were covered with watch glasses and heated for 30 min in a sand bath until any visible particles were dissolved. In the meantime six standard solutions containing 0.1-25 mg Fe/l were prepared for calibration. After cooling the samples were further diluted 1:10, so that the resulting iron concentration was between 1-10 mg/l. The samples were inserted into the Thermo iCap 6500 Duo ICP-AES (Thermo Fisher Scientific, Waltham, MA) and measured.

2.4.1.4 Core Size

The core size of the nanoparticles was determined by transmission electron microscopy.

Therefore 100 µg/ml particles of two nanoparticle samples were diluted with dH_2O in 1.5 ml microcentrifugation tubes. Carbon coated copper grids were removed from their holder by forceps and dipped into the nanoparticle suspensions. The grids were then dried at room temperature, still held by forceps.

Once dry the two grids were inserted into the sample rod of the JEOL JEM-1200EX II Electron Microscope (JEOL, Tokyo, JP). The electron beam focused, magnification adjusted and pictures taken. This procedure was repeated for all eight nanoparticle samples.

2.4.1.5 Magnetic Properties

Magnetic properties of the nanoparticles were assessed by SQUID magnetometry using the MPMS® SQUID VSM (Quantum Design, San Diego, USA).

Samples were prepared in polycarbonate holders using a small amount of cotton fibre (1-2 mm) to absorb 2-4 µl of nanoparticle solution (as received from the manufacturer) allowed to dry at RT.

Consequently, the sample holder was assembled, fixed into a brass sample rod and mounted onto the carbon rod. Next the lid off the MPMS® SQUID VSM was taken off and the carbon rod carefully inserted.

On the computer the magnetic field was set with the set point at 1000.00 Oe, rate 700.00 Oe/s and approach linear. Next the sample was located, the sample offset determined and the measuring sequence started.

2.4.1.6 Heating Potential

The heating potential was assessed by the magnetic alternating current hyperthermia (MACH) system (see Fig. 2.1), which generates an alternating magnetic field of 1.15 MHz and 13.5 kA/m. [The MACH system was kindly provided by Dr. Paul Southern of the Royal Institution of Great Britain.]

The particular frequency chosen for this system represents the practical frequency for the theoretical maximum energy loss (X") (*see section:* 1.3.1.4 and Appendix II). Practical, because in order to achieve the theoretical maximum energy loss, particles would have to be highly monodisperse, which still remains a challenge. Additionally, the goal of the engineers behind the system was to investigate the highest attainable frequency using conventional and affordable analogue electronics, which led to 1.15 MHz.

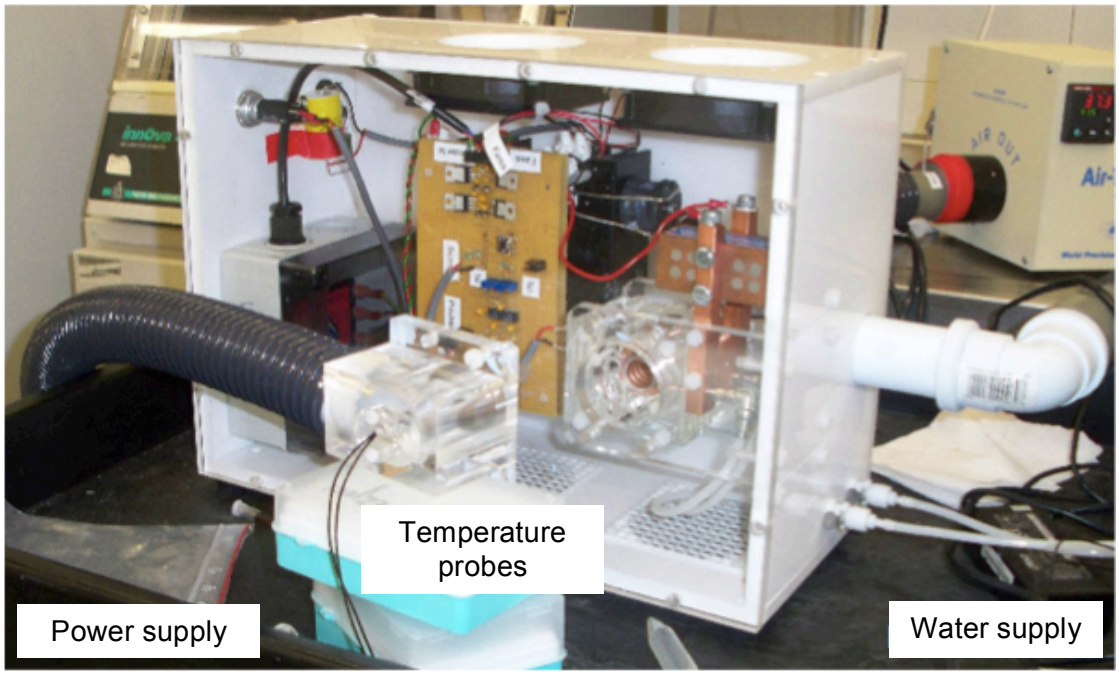

Fig. 2.1 Experimental set-up of the MACH system

In order to determine the heating potential using the MACH system, nanoparticles (1 mg Fe, according to the ICP-AES results) were transferred into a 1.5 ml microcentrifugation tube together with dH_2O to a total volume of 1 ml. A hole was drilled into the lid of the tube, before it was sealed with parafilm and an optical temperature probe (Luxtron, Santa Clara, CA) inserted into the center of the liquid sample. Next the sample was placed into the horizontal and vertical center of the copper coil of the MACH system.

The voltage on the power supply, over the course of 15 seconds, was increased to 145 V and 0.92 A to generate an alternating magnetic field of 1.15 MHz and 13.5 kA/m and the temperature recorded. After 25 min the power input was carefully decreased over the course of 15 seconds and the sample let to cool down before the procedure was repeated for another two times.

For SAR or ILP measurements, 1 ml was taken from the stock nanoparticle suspension (as received from the manufacturer) of each sample and transferred into a 1.5 ml microcentrifugation tube. A hole was drilled into the lid of the tube, before it was sealed with parafilm and an optical temperature probe (Luxtron) inserted into the center of the liquid sample. Next the sample was placed into the horizontal and vertical center of the copper coil of the MACH system. The voltage on the power supply was increased over the course of 15 seconds and the initial temperature

increase, during the first two minutes, was recorded. However, when a sample reached 65 °C before this, the measurement was stopped, to prevent the probes being damaged by the heat.

2.4.2 Protein Characterization

2.4.2.1 Protein Quantification

The concentration of proteins was determined by spectrophotometry using the following equation:

$$A_{280} = \varepsilon_{280} \cdot c \cdot l \qquad \text{Equation 2.1}$$

Where A_{280} is the absorbance at 280 nm of protein samples measured in quartz cuvettes on a Cecil CE2041 2000 series spectrophotometer, ε_{280} is the extinction coefficient (0.1%, 280 nm, 1 cm path length) of the protein calculated based on the protein primary amino acid sequence using the Expasy Protparam web tool (http://www.expasy.ch/tools/protparam.html), *c* is the protein concentration, *l* is the path length of the cuvette (1 cm). For shMFEm, shMFEm-Cys and shNFEm, ε_{280} = 1.75

2.4.2.2 Sodium dodecyl sulphate-polyacrylamide gel electrophoresis (SDS-PAGE)

Gel electrophoresis of proteins was performed under reducing conditions. Samples were prepared by the addition of 4X reducing buffer or non-reducing buffer followed by denaturation at 95 °C for 4 min. Samples were loaded onto 12% Tris-Glycine pre-cast mini-gel (Invitrogen) and separated on an XCell II™ Mini-Cell system (Invitrogen) in running buffer on an automated program of 90 min at 35 mA (125 V, 5 W) using a PowerEase® 500 power supply (Invitrogen).

Following electrophoresis, proteins were either stained with coomassie blue for two hours at room temperature. To enable visualisation of proteins the gels were de-stained with de-staining solution for another two hours with repeated de-stain solution changes. Gels were rinsed carefully with dH_2O followed by 15 min incubation in gel drying solution (Invitrogen) in preparation for drying using the Invitrogen gel drying kit. Two gel drying plastic sheets (Invitrogen) were soaked in the gel drying solution; the gel was sandwich between them and left to dry in a drying rack overnight at room temperature.

2.4.2.3 Enzyme-linked immunosorbent Assay (ELISA)

ELISA was performed on a 96-well plate (Costa, High Wycombe, UK) coated for 1 hour with 100 µl 1 µg/ml CEA in PBS or PBS only on the control wells. The wells were washed two times with PBS and blocked with 200 µl 5% milk powder (Marvel) in PBS for 1 hour at RT. 50-100 µl sample were applied to CEA or PBS coated wells in triplicate and incubated for another hour. After incubation the wells were washed three times with PBS. The wells were then incubated for 1 hour with 100 µl primary antibody diluted in 1% milk powder in PBS. Following incubation wells were washed three times with PBS-T (PBS with 0.1% Tween-20) followed by three washes with PBS. The plate was then incubated for another hour with 100 µl HRP-conjugated secondary antibody diluted in 1% milk powder in PBS. The wells were again washed with PBS-T and PBS and 100 µl OPD (O-phenylenediamine dihydrochloride; 0.4 mg/ml dissolved in phosphate citrate buffer, pH 5.0) was added. Reactions were stopped with 50 µl 4 M HCl and the absorbances were measured at 490 nm using Opsys MR™ Microplate Reader (Dynex Technologies).

2.4.3 SPION Functionalization with Antibody Fragments

2.4.3.1 Carbodiimide Conjugation

Conjugation to the available carboxyl groups on carboxylated dextran-coated particles, such as FluidMAG-CMX (Chemicell GmbH) or Ferucarbotran (Meito Sanyo) was achieved by adaptation and optimization of the carbodiimide chemistry described by DeNardo *et al.* (DeNardo, DeNardo et al. 2005) .

Ferucarbotran nanoparticle suspension (5.6 mg Fe/ml) were mixed with freshly prepared EDC/NHS activation buffer and gently mixed for 10 min at RT. The particles were then run through a PD-10 column equilibrated with 0.1 M sodium phosphate buffer. 25 µg scFv were added and the mix was put on a rotary shaker for 2 hrs at RT. Then 100 µl 50 mM glycine solution were added and the particles gently mixed for another hour. Together with 0.1 M sodium phosphate buffer the particle suspension was brought up to a volume of 5 ml. This suspension was then transferred into a Centriprep YM-50 and centrifuged at 3000 rpm for 5 min.

Before the supernatant was withdrawn and the particle concentrate again diluted down to a volume of 5 ml. These washes were repeated two times to remove the unbound scFv and glycine from the solution.

2.4.3.2 Cyanogen Bromide Conjugation

Conjugation to the available hydroxyl groups on dextran-coated particles, such as FluidMAG-DX (Chemicell GmbH) or Ferucarbotran was achieved by adaptation of the cyanogen bromide conjugation protocol recommended by Chemicell.

This involved diluting Ferucarbotran (10 mg Fe/ml) with 50 mM sodium borate buffer (pH 8.5). The particles were activated by 50 µl CNBr and incubated for 10 min on ice. The reaction was stopped running the mix through a PD-10 column equilibrated with PBS. 100 µg scFv were added and the mix was put on a rotary shaker for 24 hrs at room temperature. On the next day 100 µl of a 25 mM glycine solution were added and the mix was incubated for another hour at RT to block the unused active sites on the particles. In three overnight washes on the DynalMagnet the unbound scFv and glycine were removed.

2.4.3.3 Site-specific Attachment of scFv to Ferucarbotran

Site-specific attachment was investigated by combining sodium periodate and maleimide chemistry

10 mg sodium periodate were dissolved in 800 µl of a 50 mM sodium borate buffer (pH 8.5). Ferucarbotran nanoparticle suspension (10 mg Fe) were added and incubated on the roto-torque for 25 min at room temperature wrapped in foil, as this step is light sensitive. In the meantime a PD-10 column was equilibrated with 50 mM sodium borate buffer. To stop the reaction and remove the excess sodium periodate the particles were run through the PD-10 and collected in a fresh 2 ml micro centrifugation tube. Immediately 10 mg BMPH, the maleimide linker were added and carefully suspended in the particle mix.
The mix was incubated on the roto-torque for two hours, before 20 µl of 5 M sodium cyanoborohydride in 1 M NaOH were added. Consequently the suspension was incubated o/n on the roto-torque at RT.

On the next day 100 µl of a 0.1 M glycine in 50 mM sodium borate buffer (pH 8.5) solution were added and the mix incubated for another hour on the roto-torque. In the meantime a PD-10 column was equilibrated with 50 mM sodium borate buffer (pH 7).

The mix was run through the PD-10 column and collected in a 7 ml sterilin tube containing 100 µg shMFEm-Cys. This was gently mixed and put on the roto-torque o/n.

Subsequently 100 µl of a 0.1 M cysteine in 50 mM sodium borate buffer (pH 8.5) solution were added and the mix incubated for another hour on the roto-torque, before it was stored for purification and analysis at 4 °C.

2.4.4 FX-scFv Conjugate Purification and Characterization

2.4.4.1 Size Exclusion Chromatography with FX-scFv Conjugates

In order to purify FX-scFV conjugates size exclusion chromatography was performed. Therefore a XK 16/100 column was packed with Sephadex™ G-100 (GE Healthcare), expanded in PBS for 72 hrs at RT. The column was mounted on a lab stand and the bottom connected to a syringe filled with 70% IMS. Carefully the IMS was pushed up resulting in a 1 cm level of IMS inside the column. The syringe was removed and the end capped. Next a packing reservoir was mounted on top the column and the Sephadex™ G-100 sludge carefully poured into the column avoiding the generation of bubbles. The reservoir was filled completely by adding some PBS, before the lid was screwed on and the column connected to the ÄKTA prime plus FPLC system (Amersham Biosciences). Then sterile filtered PBS was pumped through the column at 2 ml/min and not exceeding a pressure of 0.9 mbar. Consequently the flow was stopped, the column disconnected and the bottom capped, before the reservoir was carefully screwed off and the top (incl. a flow adapter) attached. The flow adapter similar to the bottom previously was connected to a syringe containing 70% IMS in order to prevent bubble formation. Once the top was screwed on the syringe was removed and the flow adapter carefully lowered onto the Sephadex™ G-100.

The column was then connected again to the ÄKTA prime plus and run at 1.5 ml/min with a pressure limit of 0.9 mbar over night. On the next day a gel filtration protein standard was prepared, injected and run at 0.5 ml/min to establish an elution profile.

To purify FX-scFv conjugates, the conjugation mix (1-2 ml) was applied to the column and run at 0.5 ml/min, as shown in Fig. 2.2. The fractions coming out with the void were collected and consequently concentrated using a Centriprep YM-50 (Millipore) and multiple centrifugation runs, depending on the total volume, at 4000 rpm for 10 min.

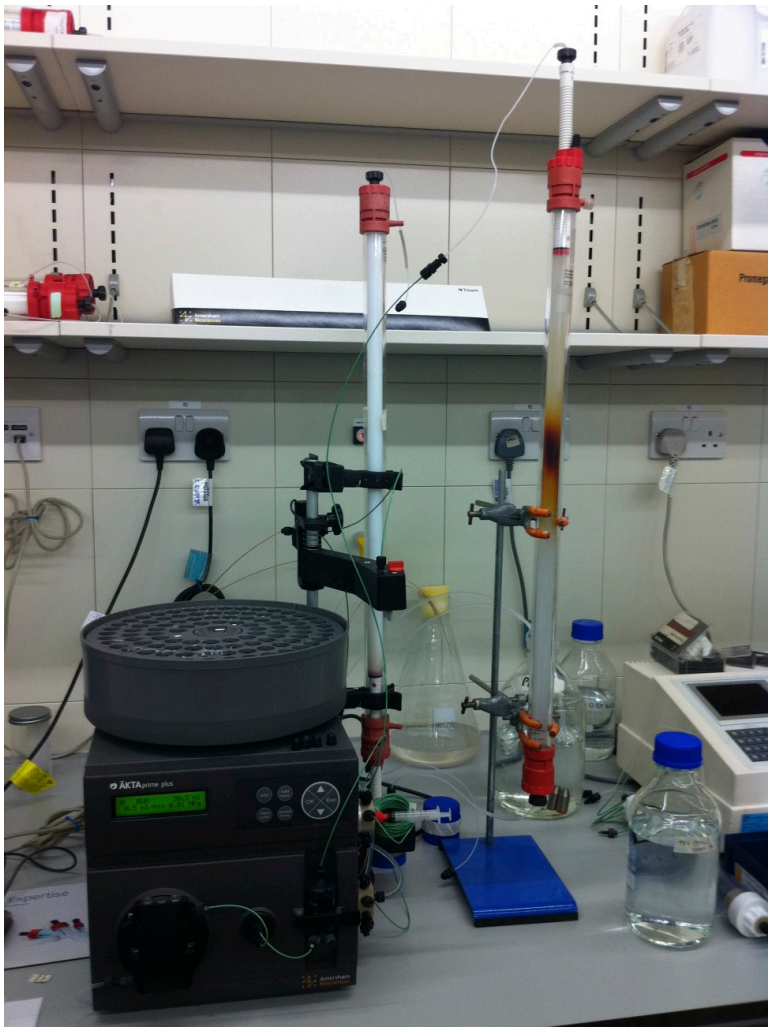

Fig. 2.2 Experimental set-up for the purification of the FX-scFv conjugates consisting of an ÄKTA prime plus FPLC system and XK 16/100 column was packed with Sephadex™ G-100.

2.4.4.2 Enzyme-linked immunosorbent assay (ELISA) with FX-scFv Conjugates

ELISA with FX-scFv conjugates was performed on 96-well MaxiSorp™ plates (Nunc). Therefore the plate was divided in two halves and each coated in triplicates with 100 µg/ml FX, FX-shMFEm, FX-shNFEm; 100 µg/ml shMFEm, shNFEm; and PBS and incubated for 1 hour at RT. The wells were washed two times with PBS and blocked with 200 µl 5% milk powder (Marvel) in PBS for 1 hour at RT. After incubation the wells were washed three times with PBS. The wells of the one half of the plate were then incubated for 1 hour with 100 µl anti-His antibody (1:500) diluted in 1% milk powder in PBS, while the wells on the other half were incubated for 1 hour with 100 µl anti-dextran antibody (1:1000). Following incubation wells were washed three times with PBS-T (PBS with 0.1% Tween-20) followed by three washes with PBS.

The plate was then incubated for another hour with 100 µl HRP-conjugated secondary antibody diluted in 1% milk powder in PBS (1:1000). The wells were again washed with PBS-T and PBS and 100 µl OPD (O-phenylenediamine dihydrochloride; 0.4 mg/ml dissolved in phosphate citrate buffer, pH 5.0) was added. Reactions were stopped with 50 µl 4 M HCl and the absorbances were measured at 490 nm using Opsys MR™ Microplate Reader (Dynex Technologies).

2.4.4.3 ECL Western Blotting with FX-scFv Conjugates

In order to perform an enhanced chemiluminescence (ECL) western blot with FX-scFv conjugates first native gels were cast using a hand casting gel kit (Bio-Rad Laboratories Ltd.).

A 2% agarose in dH_2O solution was prepared and heated up in a microwave. About 15 ml hot agarose solution were poured onto the cleaned bench top, before the kit was carefully placed in it and the agar left to gel and cool. In the meantime in order to prepare a 12% resolving gel 3.25 ml dH_2O, 5.6 ml 1 M Tris pH 8.8, 150 µl 10% SDS, 6 ml Acrylamide stock and 50 µl 10% APS were added to tube and mixed. Then 10 µl TEMED were mixed in the solution carefully poured into the immobilized kit. Quickly a couple of ml 100% IMS were added to the kit. After a couple minutes a sharp edge between gel and IMS developed. The kit was carefully removed from the agar on the bench top, the IMS emptied out. Next 3.65 ml dH_2O, 625 µl 1 M Tris pH 6.8, 50 µl 10% SDS, 820 µl acrylamide stock and 25 µl 10% APS were mixed for a 4% stacking gel. 5 µl TEMED were mixed into the solution before it was carefully poured on top of the resolution gel in the kit. Quickly the comb for the wells was inserted.

After gelation the glass plates with gel were transferred into the gel electrophoresis chamber. The comb removed and the chamber filled with running buffer. FX-scFv conjugates and controls were mixed with 4X non-reducing buffer, loaded onto the hand cast gel and run for 90 min at 35 mA (125 V, 5 W).

Then proteins were transferred to polyvinylidene difluoride (PVDF) membrane (Bio-Rad Laboratories Ltd.), pre-treated by soaking in methanol for 10 min. Gels were sandwiched with the PVDF membrane between several sheets of pre-wetted chromatography filter paper (Whatmen, Maidstone, UK) and sponges. The “sandwich” was then submerged in an XCell II Blot Module (Invitrogen) filled with transfer buffer. Proteins were transferred using an automated program of 90 min at 125 mA (25 V, 17 W).

Following electro-transfer, PVDF membranes were blocked in 5% milk powder in PBS for one hour. Next the membranes were washed in PBS and incubated on a rocker at room temperature for another hour subjected to an anti-His antibody (1:500) diluted in 1% milk powder in PBS. Consequently the membranes were washed with three times with PBS-T (0.1% Tween-20 in PBS) and three times with PBS only. Next they were incubated again on the rocker for another hour in 1% milk powder in PBS containing a horseradish peroxidase (HRP) conjugated secondary antibody (1:1000).

Finally, the membranes were washed again with PBS-T and PBS and treated with ECL Plus Western Blotting Detection Reagents (GE Healthcare) to allow the proteins to visualize. The Western Blots were put into plastic wrap and imaged for 30 s using a Kodak imaging cassette (Kodak) and Kodak Bio-Max MR-1 film (Kodak) in the dark room followed by developing the film in the developer.

2.4.4.4 Quartz Crystal Microbalance

Quartz crystal microbalance (QCM) was performed by immobilizing the scFvs or FX-scFv conjugates on sensor chip and treating them with different concentrations of the antigen NA1 using the Attana A200® Biosensor (Attana, Sweden).

For immobilization and analysis of the scFvs the carboxyl sensor chips were inserted into channel A and B of the Attana A200 and equilibrated by running sterile filtered PBS over them at 20 µl /min until the baseline stabilized. Next 50 µl EDC/NHS were injected to both channels followed by shMFEm in channel A and shNFEm in channel B. The chips were then blocked with 35 µl BSA each. In between each step buffer was run over the sensor chips at 10 µl /min.

For the measurements 35 µl of concentration 1 of the antigen NA1 (5 ng/ml) were injected on both channels followed by PBS at 10 µl/min for 10 min. The sensor chips were regenerated pulsing them for 15 sec with 100 mM glycine pH 3, before they were equilibrated again with PBS. This procedure was repeated for all concentrations of antigen ranging from 5 – 50 ng/ml.

The FX-scFv conjugates were immobilized by manually injecting two PS sensor chips with 1 mg particles/ml FX-shMFEm and FX-shNFEm and incubating them overnight at 4 °C. Then the sensor chips were inserted into Channel A and B of the Attana A200 and equilibrated with PBS at 20 µl/min until the baseline stabilized. Next the sensor chips were blocked with 35 µl BSA each and followed by PBS.

2.4.5 Cell Culture

2.4.5.1 Thawing Cell Stock from Cryostorage

In order to start a fresh cell line a laminar class II cabinet was started and disinfected. Next the appropriate media (see Table 2.9) was prepared and warmed up to 37 °C in a water bath. 18 ml medium were transferred into a T-75 cell culture flask left for one hour in the incubator at 37 °C and 5% CO_2 to equilibrate.

A frozen stock vial was removed from the liquid nitrogen tank and quickly thawn in the waterbath. The cells were resuspended, transferred into the cell culture flask and incubated o/n. On the next day the cells were checked under the microscope and the medium was replaced.

2.4.5.2 Sub-culturing Cell Lines

Once about 70% confluency was reached, cells were sub-cultured twice a week in a specific split ratio depending on their growth. This was achieved through withdrawal of the medium, two gentle washes with 5 ml PBS, release of the cells by addition of. The trypsin-EDTA was then neutralized by the addition of 12 ml PBS, the cell suspension spun down at 1500 rpm for 3 min, the supernatant discarded and the cell pellet resuspended in 10 ml medium. 2 ml cell suspension were transferred into a new cell culture flask together with 18 ml fresh medium and put back into the incubator.

2.4.5.3 Preparing Cell Lines for Cryostorage

In order to preserve cells, a freezing medium with 5% DMSO was prepared. Then the cells were treated as for sub-culturing. The media was withdrawn, followed by two gentle washes with 5 ml PBS and release of the cells by the addition of 3 ml trypsin-EDTA and incubation for 3-6 min at 37 °C. The trypsin-EDTA was then neutralized by the addition of 12 ml PBS, the cell suspension spun down at 1500 rpm for 3 min, the supernatant discarded and the cell pellet resuspended in 1 ml medium. 20 µl were transferred to a previously cleaned hemocytometer or counting chamber. The cells were then counted. Next the cells were diluted with freezing media to a final concentration 1 x 106 cells/ml. The cell suspension was then quickly transferred into 1.8 ml cryovials (Nunc) and frozen at -80 °C. After 1-2 hours the cells were transferred into liquid nitrogen until further use.

2.4.5.4 Immunostaining Adherent Cells

In order to fluorescently label cells, cells were seeded on 13 mm round glass coverslips (VWR) in a 24-well plate (Corning) at a density of 1 x 10^5 cells/well together with 500 µl media. Once the cells reached the desired confluency the media was carefully aspirated, the wells washed with PBS and the cells fixed with 4% paraformaldehyde for 20 min. This was followed by three washes with PBS and incubation with 50 mM glycine for 10 min. Next the wells were washed again three times with PBS and blocked with 3% BSA in PBS for one hour. The slides were washed again with PBS, before they were removed from the wells using tweezers and set on the upside down turned cut off caps of microcentrifugation tubes in a small chamber humidified by Kim wipes wetted with PBS. Quickly 100 µl of 1% BSA in PBS solution with a mouse anti-CEA antibody were added to each slide and incubated for one hour at RT. The slides were washed with PBS. Another 100 µl of 1% BSA in PBS solution with an Alexa Fluor labeled anti-mouse antibody were added to each slide. The slides were then incubated in the dark at RT for another hour. Next the slides were washed with PBS three times and treated with a drop DAPI mounting solution in 1 ml PBS for 30 sec. The slides were quickly washed again in PBS and mounted on glass slides with a drop of ProLong® Gold Antifade (Invitrogen). The slides were sealed off with transparent nail varnish and immediately imaged using the fluorescent microscope (Leica).

2.4.6 Magnetic Nanoparticle Hyperthermia *in vivo*

All animal work was carried out according to the Home Office License with the help of Mathew Robson and Mario Mazzantini (Department of Oncology) at the Wolfson Institute of Biomedical Research.

2.4.6.1 Inducing and Establishing Xenografts

In this thesis different xenograft models were investigated. The CEA positive human cell lines SW1222, LS174T and Capan-1 were used to induce tumours in the left flank of female MF1 nude mice (Charles River Laboratories International Inc). The mice were 2-3 months old, weighing 20-25 g, when 1 x 10^6 cells in saline were injected subcutaneously. Within 2-3 weeks the tumour volume increased to 0.75 – 1.1 cm^3.

2.4.6.2 Non-Targeted Magnetic Nanoparticle Hyperthermia

For this experiment seven mice carrying SW1222 xenografts were grown and split into two treatment groups and one negative control. One group of three was treated with fM-DX 100, while the other group received Ferucarbotran. In each group one mouse received a high dose (2 mg Fe per tumour) without being subjected to the alternating magnetic field, while the remaining mice received a high dose or low dose (0.5 mg Fe per tumour) together with AMF.

Therefore, one mouse at a time was anesthetized with isofluorane, injected with the adequate amount of particle and immediately transferred to the copper coil of MACH system. The alternating magnetic field was switched on and the voltage on the power supply increased over the course of 15 seconds to a maximum of 145 V and 0.92 A. The mouse was treated for 20 min. The temperature development on the surface of the mouse was monitored via thermal imaging. The experimental set-up can be found in Fig. 2.1. Additionally, an optical temperature probe was inserted into the anus of the two mice treated with Ferucarbotran (and subjected to the AMF) to record internal temperature.

Afterwards, the mouse was allowed to recover in an oxygenated environment, before it was put back into the cage. 40 min later the mouse was sacrificed, the tumour excised and put into 4% formalin for further processing (preservation in paraffin) and analysis. This procedure was repeated for every mouse according to the above mentioned treatment regimen.

2.4.6.3 Identifying Suitable Tumour Model for Magnetic Nanoparticle Hyperthermia

For this experiment a total of six mice were induced with SW1222, LS174T and Capan-1 xenografts - two mice per tumour type.

One mouse at the time was anesthetized with isofluorane and injected iT with Ferucarbotran (3 mg Fe/cm^3 tumour volume) as described by Giustini *et al.* The needle remained in place for 5 minutes post-injection. (Giustini, Ivkov et al. 2011) Afterwards the mouse was left to recover for 25 min and sacrificed. The tumour was excised, processed and put into paraffin for further analysis. This procedure was repeated with each tumour.

2.4.6.4 Antibody-Targeted Magnetic Nanoparticle Hyperthermia

For this experiment seven mice carrying LS174T xenografts were grown and split into two treatment groups and one negative control. One group of three was treated with Ferucarbotran functionalized with shMFEm (FX-shMFEm), while the other group received FX-shNFEm. The negative control was injected with PBS only.

One mouse at the time was anesthetized with isofluorane and injected iT with either FX-shMFEm or FX-shNFEm (3 mg Fe/cm^3 tumour volume). The needle remained in place for 5 minutes post-injection. The mouse was then either left to recover in the cage for 55 min before it was sacrifized (two control mice per group), or subjected to an alternating magnetic field (AMF) for 25 min, as shown in Fig. 2.1. The surface temperature of the mouse was monitored through thermal imaging.

After the hyperthermia treatment the mouse was left to recover for 30 min and sacrifized. The tumour was excised, fixed, processed and put into paraffin for further analysis. This procedure was repeated with each tumour.

2.4.7 Histology

2.4.7.1 Prussian Blue Staining

To verify the location of iron oxide nanoparticles within the tumour tissue sections were stained with Prussian blue. Therefore the tissue slides were deparaffinised in histoclear for 9 min (3 x 3 min); dehydrated in IMS (100% x 2, then 70% x 1 for 3 min each) and washed with distilled water. Next 25 ml of 2% potassium ferrocyanide were mixed with 25 ml 2% HCl in a coplin jar. The slides were placed in the jar for 30 min, before they were counterstained for 5 min in 0.1% Nuclear Fast Red. Afterwards the slides were washed again with distilled water (3 x 3 min), dehydrated in IMS (70% x 1, then 100% x 2 for 3 min each) and histoclear (3 x 3 min). The slides where subsequently mounted using DPX and imaged with the NanoZoomer Digital Pathology System (Hamamatsu, Japan)

2.4.7.2 Cleaved Caspase-3 Staining

To determine, if nanoparticles induced apoptosis the tissue sections were stained with a cleaved caspase-3 antibody. Hence the tissue slides were deparaffinised in histoclear for 9 min (3 x 3 min); dehydrated in IMS (100% x 2, then 70% x 1 for 3 min each) and washed with distilled water.

Next the slides were cooked in the microwave for 10 min in 0.01 M citrate buffer (pH 6). The slides were then thoroughly washed with tap water and PBS/T. The tissue was marked with a wax pen and the endogenous peroxidase blocked with 3 % hydrogen peroxide in methanol for 10 min. This was followed by 3 x 3 min washes with PBS/T. 3 % goat serum diluted in PBS/T was applied for 20 min at RT, then the primary antibody, Cleaved casp.-3 (Asp 175) (5A1) (Cell Signaling Technology), diluted 1/100 in PBS/T, was applied and the slides incubated at 4 °C o/n.

On the next day the slides were thoroughly washed with PBS/T (3 x 3 min) before the secondary antibody, polyclonal goat anti rabbit IgG biotinylated Ab (Abcam), diluted 1/200 in PBS/T, was applied for 30 min at RT. At the same time the AB complex was prepared by adding one drop of reagent A and one drop of reagent B to 2.5 ml PBS/T. The slides where thoroughly washed with PBS/T (3 x 3 min) and incubated with AB complex for 30 min at RT. This was followed by another series of washes (3 x 3 min with PBS/T). Next DAB (1/50) was applied for up to 10 min or when the colour was sufficient. Then the slides where thoroughly washed with tap water, counterstained with haematoxylin and thoroughly rinsed with tap water. Afterwards the slides were dehydrated in IMS (70% x 1, then 100% x 2 for 3 min each) and histoclear (3 x 3 min). Subsequently the slides were mounted with DPX and imaged.

2.4.7.3 Heat Shock Protein 70 (HSP70) Staining

To determine, if nanoparticles were inducing heat stress, the tissue sections were stained with a HSP70 antibody. Therefore the tissue slides were deparaffinised in histoclear for 9 min (3 x 3 min); dehydrated in IMS (100% x 2, then 70% x 1 for 3 min each) and washed with distilled water. Next the slides were cooked in the microwave for 10 min in 0.01 M citrate buffer (pH 6). The slides were then thoroughly washed with tap water and PBS/T. The tissue was marked with a wax pen and the endogenous peroxidase blocked with 3 % hydrogen peroxide in methanol for 10 min. This was followed by 3 x 3 min washes with PBS/T. 3 % normal rabbit serum diluted in PBS/T was applied for 20 min at RT, then the primary antibody, HSP70 (6B3) rat mAb (Cell Signaling Technology), diluted 1/200 in PBS/T, was applied and the slides incubated for 1 hour at RT.

After incubation the slides were thoroughly washed with PBS/T (3 x 3 min) before the secondary antibody, polyclonal rabbit anti rat IgG biotinylated Ab (Abcam), diluted 1/200 in PBS/T, was applied for 30 min at RT. At the same time the AB complex was prepared by adding one drop of reagent A and one drop of reagent B to 2.5 ml

PBS/T. The slides where thoroughly washed with PBS/T (3 x 3 min) and incubated with AB complex for 30 min at RT. This was followed by another series of washes (3 x 3 min with PBS/T). Next DAB (1/50) was applied for up to 10 min or when the colour was sufficient. Then the slides where thoroughly washed with tap water, counterstained with haemotoxylin and thoroughly rinsed with tap water. Afterwards the slides were dehydrated in IMS (70% x 1, then 100% x 2 for 3 min each) and histoclear (3 x 3 min). Subsequently the slides were mounted with DPX and imaged.

2.5 Summary

The aim of this chapter was to select appropriate techniques for the characterisation of the nanoparticles, as well as the scFv antibody fragments, the functionalisation of the nanoparticles with the scFv antibody fragments, the purification and characterisation of the SPION-scFv conjugates and the antibody targeted magnetic nanoparticle hyperthermia *in vivo*.

These particular techniques were selected based on recommendations, as well as specific literature and the resources available.

Chapter 3

A Study of Properties of Magnetic Nanoparticles for Hyperthermia

3.1 Introduction

The work described in this chapter shows the characterization and evaluation of the heating potential of different MNP to identify the most suitable candidate for hyperthermia application.

The most apparent difference between MNP is their hydrodynamic diameter, however also a number of other physical factors have been demonstrated to influence the heating potential of MNP (Pankhurst, Connolly et al. 2003; Krishnan 2010). In order to maximize their hyperthermic potential, the iron oxide should be between 11-15 nm depending on the field conditions (Gonzales-Weimuller, Zeisberger et al. 2009; Kallumadil, Tada et al. 2009; Krishnan 2010) to encourage Néel relaxation rather than Brownian motion as the main heating mechanism (*see section:* 1.3.1).

Another way to improve the heating potential of magnetic nanoparticles is to change the core material from iron oxide to a magnetically more favourable material, such as cobalt ferrite or manganese ferrite. Currently the best heating magnetic nanoparticles are $CoFe_2O_4$@$MnFe_2O_4$ core shell nanoparticles with a SAR of up to 4000 W/g at 500 kHz and 37.3 kA/m (Lee, Jang et al. 2011). However, the toxicity of these particles is barely understood.

Iron oxide is deemed safe, as the particles administered for imaging represent only a small fraction (1.25 – 5%) of the total human iron stores (Tsourkas 2009). Still, especially in cases of regional deposition of iron oxide nanoparticle for biomedical applications, such as hyperthermia, there remains a potential risk of local toxicity (Singh, Jenkins 2010).

Since MNP differ with regard to the coating to iron ratio, core composition and size, the atomic iron content was chosen as the common denominator to compare heating potentials.

3.2 Objectives

The objectives of the research described in this chapter were to:

1. Determine hydrodynamic diameter and size distribution of the MNP
2. Measure zeta potential of the MNP
3. Determine structure and core size of the MNP
4. Quantify the atomic iron content
5. Determine magnetic properties of the MNP
6. Determine heating potential of MNP using the MACH system.

3.3 Results

3.3.1 Hydrodynamic Diameter and ζ-Potential

The first parameter to be assessed was the hydrodynamic diameter, as it provides not only information about the overall size of the nanoparticles, but also the distribution of sizes in a suspension. The hydrodynamic diameter was determined by dynamic light scattering (DLS) using a Nanosizer ZS90 (Malvern). Therefore, 10 µg particles were suspended and measured at least three times in 1 ml dH_2O, 5 mM NaCl and PBS. These buffers were chosen, as different salt concentration is known to affect the hydrodynamic diameter of nanoparticles with certain coatings, like dextran.

[Note: Due to a limitation in the software of the Nanosizer ZS90, the raw data could not be exported; instead screenshots were taken and recorded.]

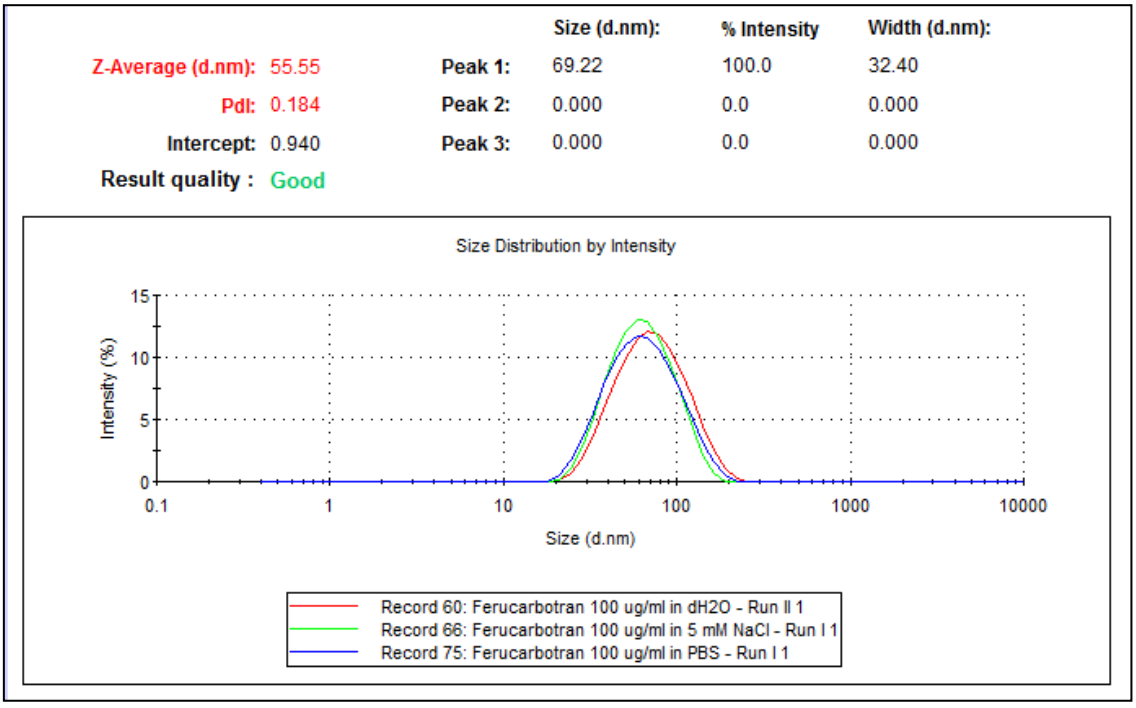

Fig. 3.1 Hydrodynamic size distributions (by intensity) of Ferucarbotran in distilled water (red line), 5 mM NaCl (green line) and PBS (blue line) showing an average size of 55.55 nm (z-average) with a PdI of 0.184, indicating polydispersity and an average intensity peak at 69.22 nm. The result quality 'good' indicates that the sample matched the requirements of the system for a successful measurement. Each line represents a single measurement. [Screenshot taken from DTS Nano program]

The Nanosizer ZS90 and its corresponding software, DTS Nano (Malvern), provided different values for interpreting the size (Fig. 3.1), such as the z-average. This particular value is an average taken from across the size distribution, while the peak

value represents the most prevalent size within the nanoparticle suspension. Therefore, the peak values were used to assess particle sizes as presented in Table 3.1 and Fig. 3.2. The polydispersity index (PdI) the width of the size distribution and suspensions with a PdI bigger than 0.100 are considered polydisperse. Since the size affects the heating mechanisms, a narrow size distribution with a low PdI is favourable (Hergt, Dutz et al. 2008). If the size distribution is too wide, only a small part of the particle suspension will contribute to the heating potential (*see section:* 1.3.1).

Table 3.1 Determined hydrodynamic diameters of nanoparticles in dH_2O, 5 mM NaCl and PBS

Sample	dH_2O	5 mM NaCl	PBS
fM-DX 50	49	50	50
fM-DX 100	197	183	184
fM-CMX 100	106	N/A	N/A
fM-DXS 100	79	N/A	N/A
nm-D-spio 100	88	87	89
nm-CLD-spio 100	147	111	102
BNF-starch 100	136	136	134
Ferucarbotran	77	68	69

As all samples were supplied suspended in dH_2O, quite surprisingly, some nanoparticles were substantially bigger than the manufacturers specifications. The biggest discrepancy between specification and determined hydrodynamic diameter was observed in the fM-DX 100 samples, as the data showed a size of 183-197 nm instead of 100 nm. Also BNF-starch 100 and nm-CLD-spio 100 were found to be considerably bigger than their name and specifications indicated. However, the values obtained from the nm-CLD-spio 100 in 5 mM NaCl and PBS were within an acceptable range of 102-111 nm.

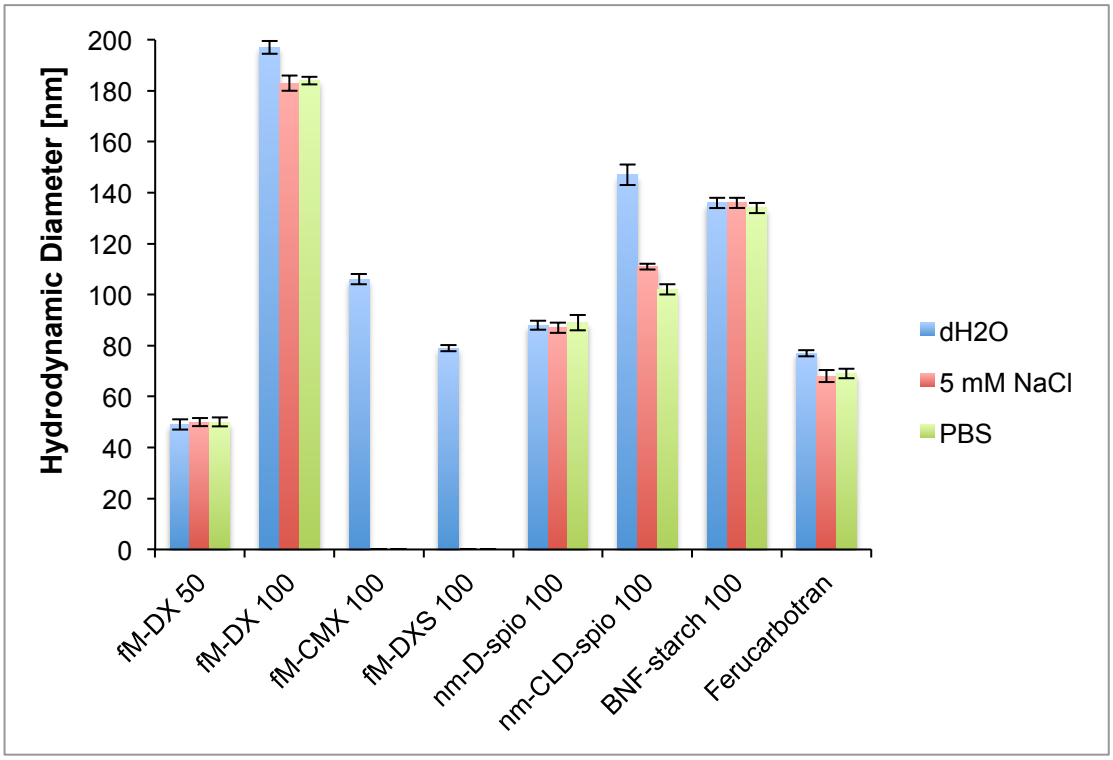

Fig. 3.2 Determined hydrodynamic diameters of commercial nanoparticles suspended in distilled water (blue), 5 mM NaCl (red) and PBS (green). The number next to the nanoparticle name represents the size specifications provided by the manufacturer. fM-CMX 100 and fM-DXS were not stable in 5 mM NaCl and PBS and precipitated, therefore no values could be obtained. fM-DX 100 with 183-197 nm demonstrated almost twice the size suggested by the specifications. Overall minor differences of particles between buffers were observed, except for fM-CLD, showing 30% bigger size in dH_2O compared to 5 mM NaCl and PBS. Detailed numbers for each particle and buffer can be found in Table 3.1.

fM-CMX 100 and fM-DXS 100 were measured only in water, as they started to precipitate immediately after suspension in 5 mM NaCl and PBS and their hydrodynamic diameter increased as shown in Fig. 3.2. The reason for this is that both, fM-CMX 100 and fM-DXS 100, had highly charged functional groups within their coating, such as carboxyl (fM-CMX) and sulphate (fM-DXS) groups, allowing sodium (Na^+) and chloride (Cl^-) ions to form solid salts.

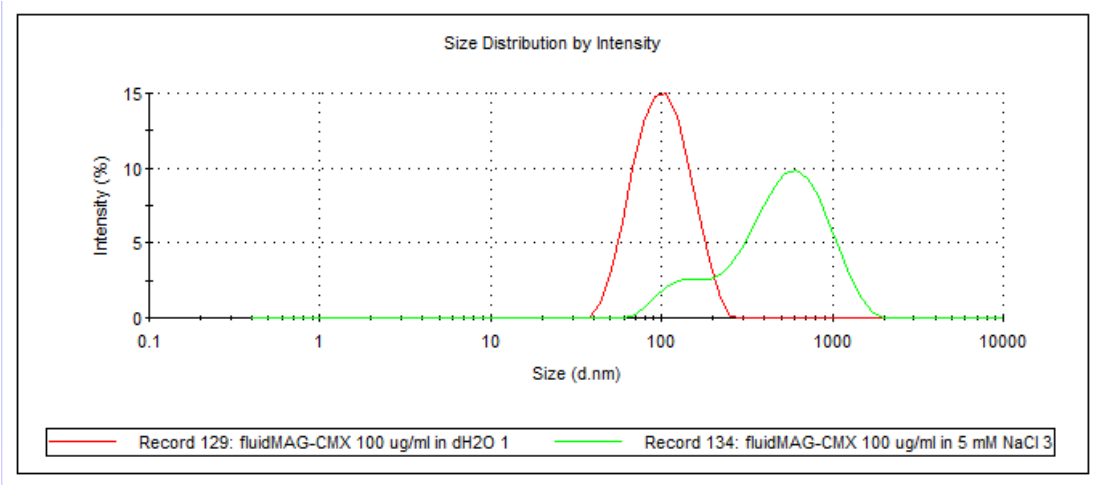

Fig. 3.3 Determined hydrodynamic size distributions of fM-CMX in dH_2O (red line) and 5 mM NaCl (green line). fM-CMX in dH_2O shows a normal distribution with a peak at 100 nm, fM-CMX suspended 5 mM NaCl shows a lower peak at around 150 nm and higher peak at around 600 nm, with an overall distribution ranging from 60 – 2000 nm revealing particle aggregation and precipitation. Each line represents a single measurement. [Screenshot taken from DTS Nano program]

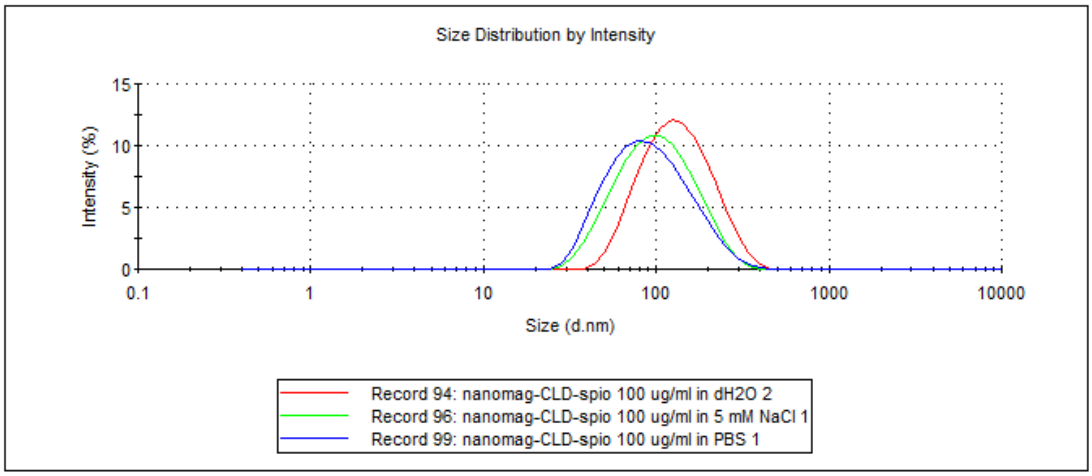

Fig. 3.4 Hydrodynamic size distributions of nm-CLD-spio in dH_2O (red line), 5 mM NaCl (green line) and PBS (blue line) showing a shift of the different distributions and thus a deviation in peak values (see Table 3.1). Each line represents a single measurement. [Screenshot taken from DTS Nano program]

Even though the different buffers did not affect most particles, in the case of the cross-linked dextran nanoparticles, nm-CLD-spio 100, their size decreased in the presence of ions by 25-30% in 5 mM NaCl and PBS (Fig. 3.3 and Table 3.1) as the shift in distribution suggests. However, size distribution did not widen, indicating that this was not caused through agglomeration of the particles.

The Nanosizer ZS90 (Malvern) also provided the option to determine the ζ-potential, which is important information on how the particles will interact with cells. Highly positively or negatively charged particles are taken up more rapidly than neutral particles (Mailander and Landfester 2009). The ζ-potential is the electric potential of a double layer of ions around the nanoparticles and therefore measured in the presence of 5 mM NaCl.

Table 3.2 Measured ζ-potential for different nanoparticles

Sample	ζ-potential [mV]
fM-DX 50	-1
fM-DX 100	-1
fM-CMX 100	N/A*
fM-DXS 100	N/A*
nm-D-spio 100	-5.5
nm-CLD-spio 100	-4
BNF-starch 100	0
Ferucarbotran	-23

[* No values were obtained for fM-CMX 100 and fM-DXS 100, as they were not stable in 5 mM NaCl]

As fM-CMX 100 and fM-DXS 100 were not stable in 5 mM NaCl the ζ-potential could not be determined. The ζ-potentials of most particles were almost neutral, as dextran and starch is not charged, except for Ferucarbotran with a ζ-potential of -23 mV coated in carboxylated dextran. This indicates that Ferucarbotran has carboxyl groups on the surface, which is important information for possible functionalization.

3.3.2 Atomic Iron Content

There are various methods of determining the iron content in nanoparticles, but as the cores are mostly a mixture of magnetite (Fe_3O_4) and maghemite (γ-Fe_2O_3) or other iron species, this becomes increasingly difficult, as most methods determine one kind of Fe ion. The ferrozine assay, for example, only quantifies Fe^{2+} ions (Riemer, Hoepken et al. 2004), while another assay, a modified version of the Prussian blue reaction, as recommended by one manufacturer [Correspondence with CEO Christian Bergemann, Chemicell, Germany] only quantifies Fe^{3+}. So, even a combination of these assays provides at best a ratio of Fe^{2+} to Fe^{3+}.

Another method is inductively coupled plasma atomic emission spectroscopy (ICP-AES), allowing quantification of all iron present independent of their charge. Therefore, this method was chosen and, with the kind help and expertise of Stanislav

Strekopytov from the Natural History Museum, the atomic iron content of the nanoparticles was determined.

Table 3.3 Atomic Fe content determined by ICP-AES compared to the estimated Fe content specified by the manufacturers.[1]

Sample	Particle conc. [mg/ml]	Estimated Fe content [%]	Fe [mg/ml]	Determined Fe content [%]
fM-DX 50	100	30-35	30.59	30.59
fM-DX 100	25	60-70	15.7	62.80
fM-CMX 100	25	60-70	17.75	71.00
fM-DXS 100	25	60-70	17.69	70.76
nm-D-spio 100	25	10	2.39	9.56
nm-CLD-spio 100	5	50	2.14	42.80
BNF-starch 100	25	60	14.83	59.32
Ferucarbotran	55	100	50.69	92.16

[Note: The results in this table represent single measurements, since the time on the instrument was limited.]

Overall the iron content of the tested nanoparticles corresponded to the estimated values stated in the manufacturer's specifications[1]. The iron content of the fM-DX 50 was significantly lower than in the fM-DX 100, which is not surprising since smaller cores require a higher amount of coating. The low iron content of nm-d-spio 100 is also a consequence of the coating. These particles have a comparably thicker shell than fM-DX 100, fM-CMX 100 or fM-DXS 100 improving their colloidal stability.

In contrast to Micromod and Chemicell, Meito-Sanyo, the manufacturer of Ferucarbotran, did not provide a particle concentration, but instead the atomic iron concentration; therefore the estimated iron content in Table 3.3 is stated as 100%.

[1] For Micromod: Corresponding technical data sheets were found at http://www.micromod.de accessed 12.01.12
For Chemicell: Personal correspondence with CEO Christian Bergemann

3.3.3 Core Size and Structure

Other important information to gain an insight into the hyperthermia potential of a magnetic nanoparticle is the core size and structure, as this will affect heating mechanism (*see section:* 1.3.1.1). Core size and structure of the nanoparticles was determined by transmission electron microscopy (TEM) using the JEOL JEM-1200EX II Electron Microscope (JEOL, Tokyo, JP). Therefore 100 µg/ml nanoparticles from the stock solution were diluted with dH_2O in 1.5 ml microcentrifugation tubes. Carbon coated copper grids were removed from their holder by forceps and dipped into the nanoparticle suspensions. The grids were then dried at room temperature, still held by forceps and consequently viewed and analysed under the TEM. Images obtained through TEM mainly show the particles' cores, as they have a much higher electron density than the polymer (Ortega 2012).

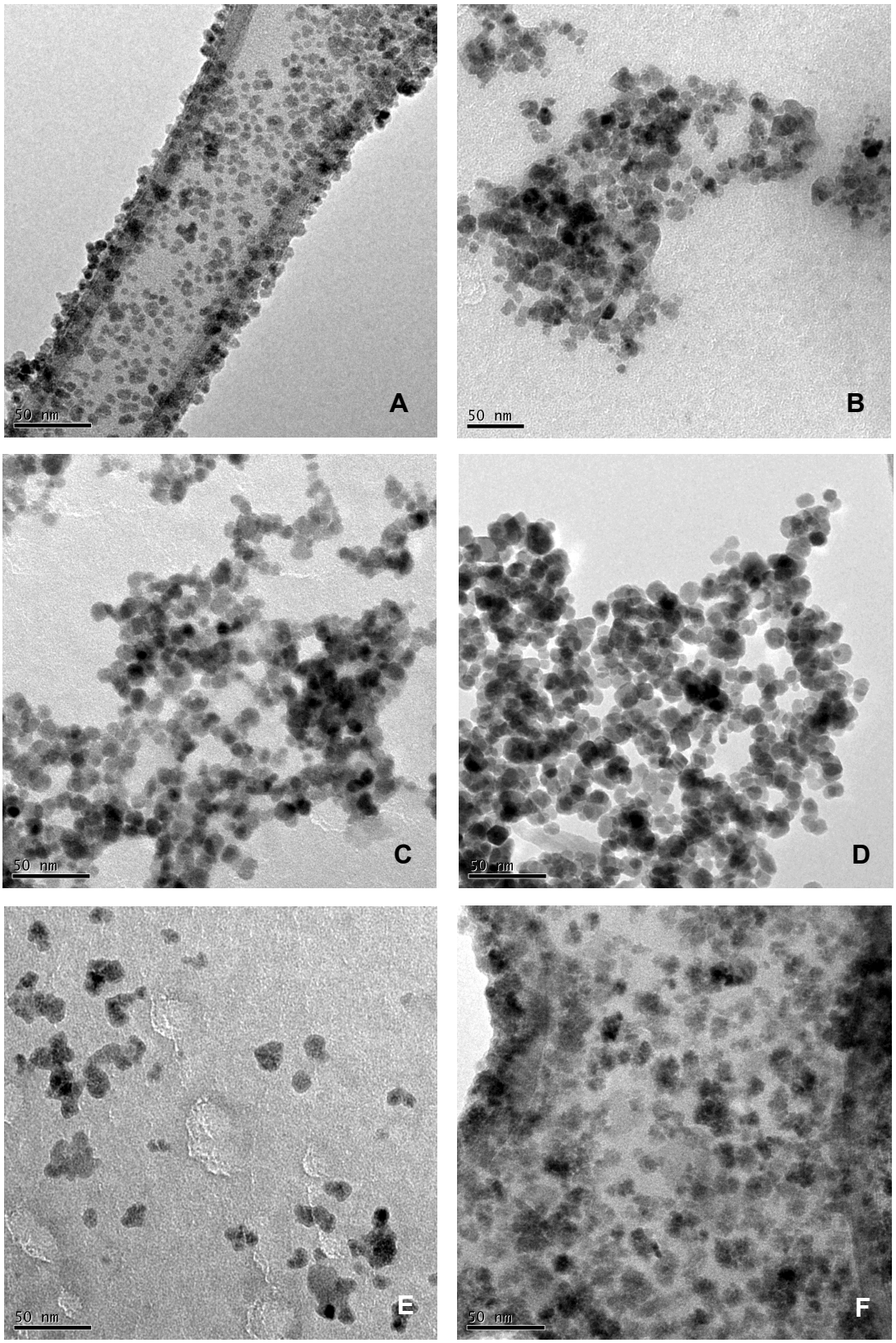

Fig. 3.5 TEM images of different nanoparticles captured on carbon coated copper grids. (A) fM-DX 50 showed core sizes ranging 2-5 nm; (B) fM-DX 100, (C) fM-CMX 100, (D) fM-DXS demonstrated similar cores with diameters between from 5-10 nm; (E) nm-d-spio 100 cores ranged 4-7 nm, (F) nm-CLD-spio 100 resembled small clusters with sizes between 10-20 nm consisting each of several 3-5 nm crystals.

While the Chemicell nanoparticles (fM-DX 50, fM-DX 100, fM-CMX 100 and fM-DXS 100) showed very similar cores (Fig.3.5), the Micromod particles varied in core size, but also in shape. nm-d-spio 100 with their round crystals resembled the Chemicell particles, nm-CLD-spio 100 resembled more mini-clusters [see (F) in Fig. 3.5].

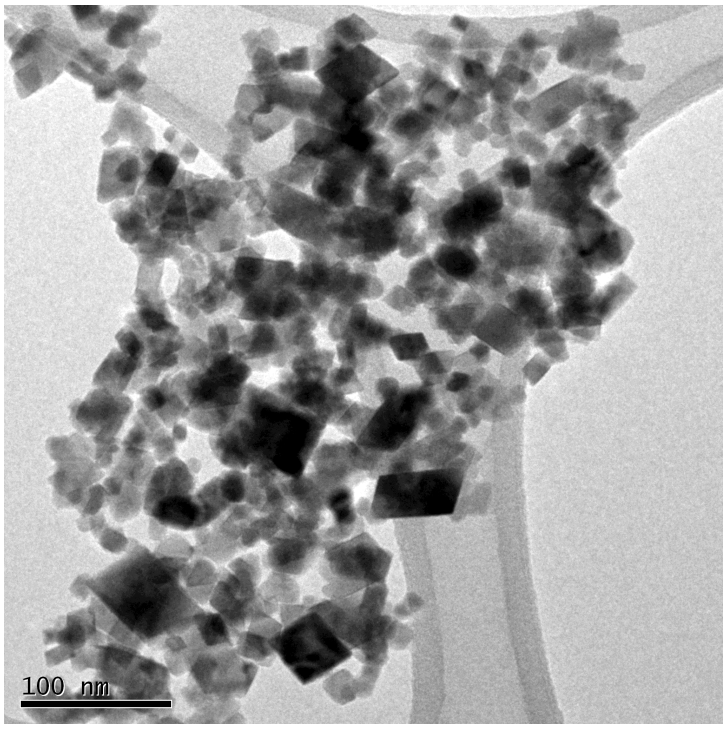

Fig. 3.6 TEM image of BNF-starch 100 presenting cubelike structure with a core size distribution between 5-50 nm, suggesting thermal blockage at room temperature.

Interestingly, the BNF-starch 100 (Fig. 3.6), specifically designed for hyperthermia application (Bordelon, Cornejo et al. 2011), showed a completely different core shape to the other nanoparticles presenting a cuboid in structure.

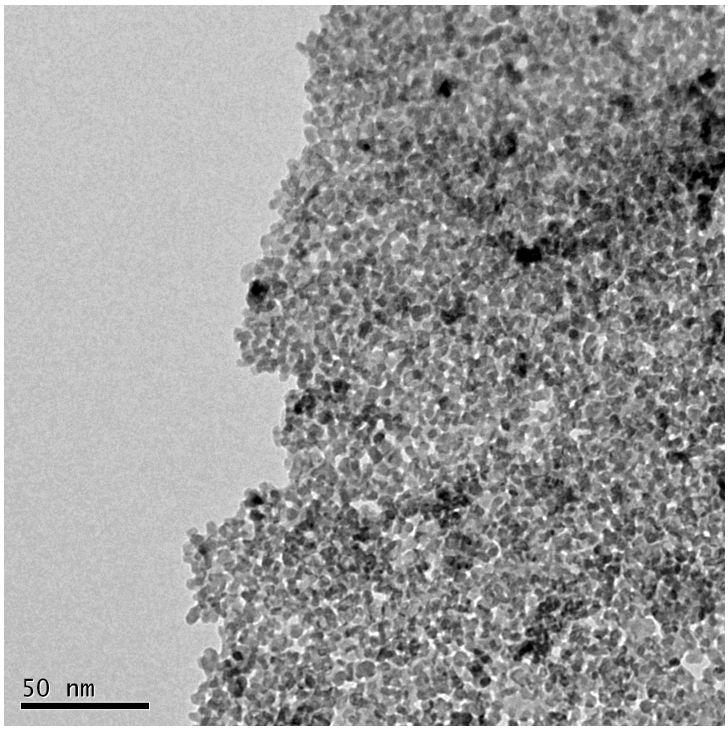

Fig. 3.7 TEM image of clustered Ferucarbotran cores 4-5 nm in size.

Ferucarbotran consisted mostly of 4-5 nm crystals (Fig. 3.7), similar to the fM-DX 50 (see A in Fig. 3.5), which is consistent with the literature (Reimer and Balzer 2003).

3.3.4 Hysteresis and Magnetic Properties

Next the magnetic properties of the nanoparticles were assessed by SQUID magnetometry using the MPMS® SQUID VSM (Quantum Design, San Diego, US). Therefore, five cotton fibers were put into a sample holder and 2-4 µl nanoparticle stock solution were added. The sample was let to dry for a couple of hours at room temperature before it was analysed in a single run using the SQUID.

The resulting MH curves, magnetisation M vs applied field H, (Fig 3.8-11) indicate superparamagnetic behaviour within Ferucarbotran particles and a mix of ferromagnetic and superparamagnetic behaviour within fM-CMX 100.

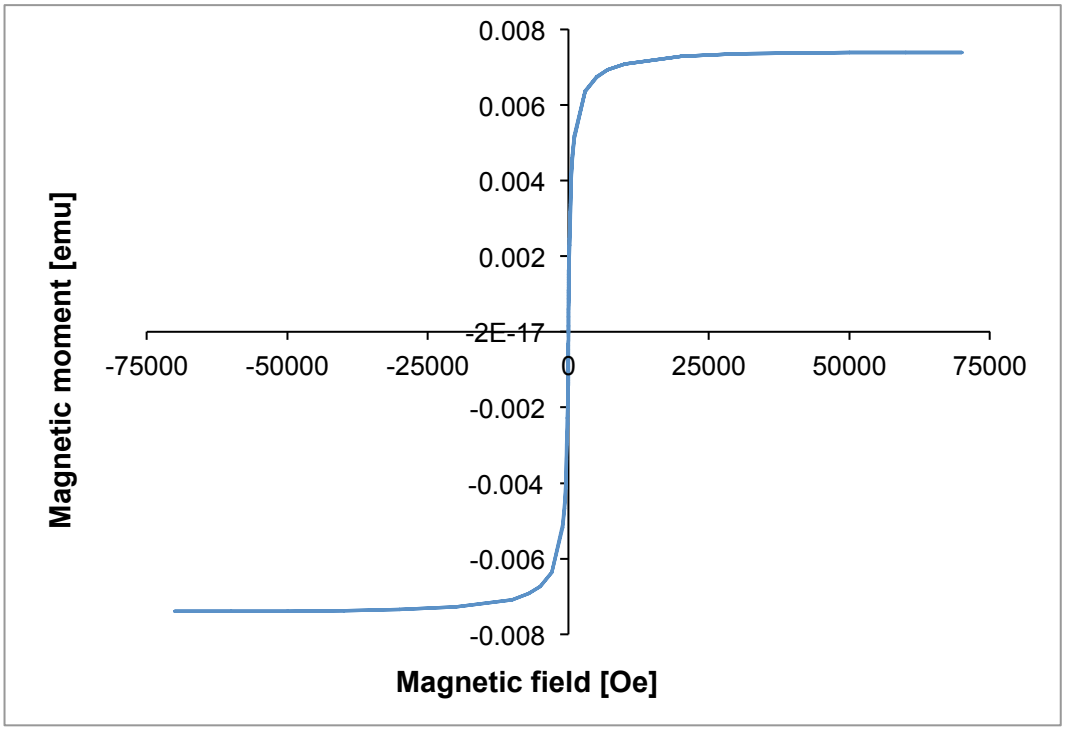

Fig. 3.8 Determined MH curves for fM-CMX 100. This MH curve represents a single measurement.

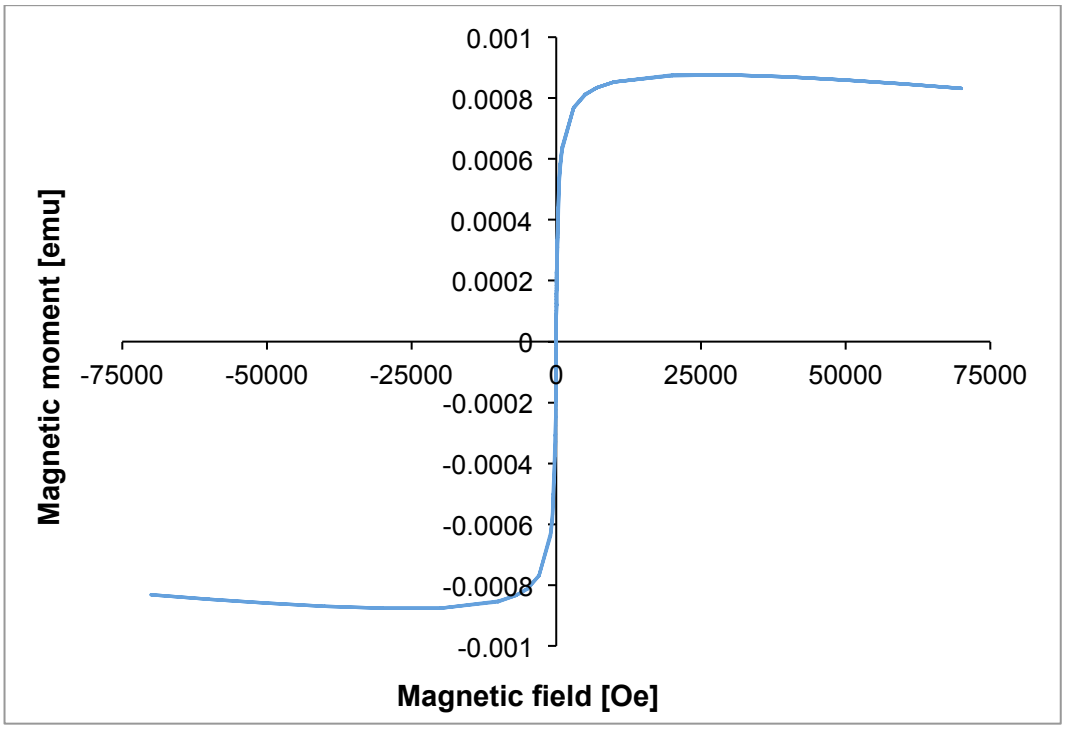

Fig. 3.9 Determined MH curves for nm-d-spio 100. This MH curve represents a single measurement.

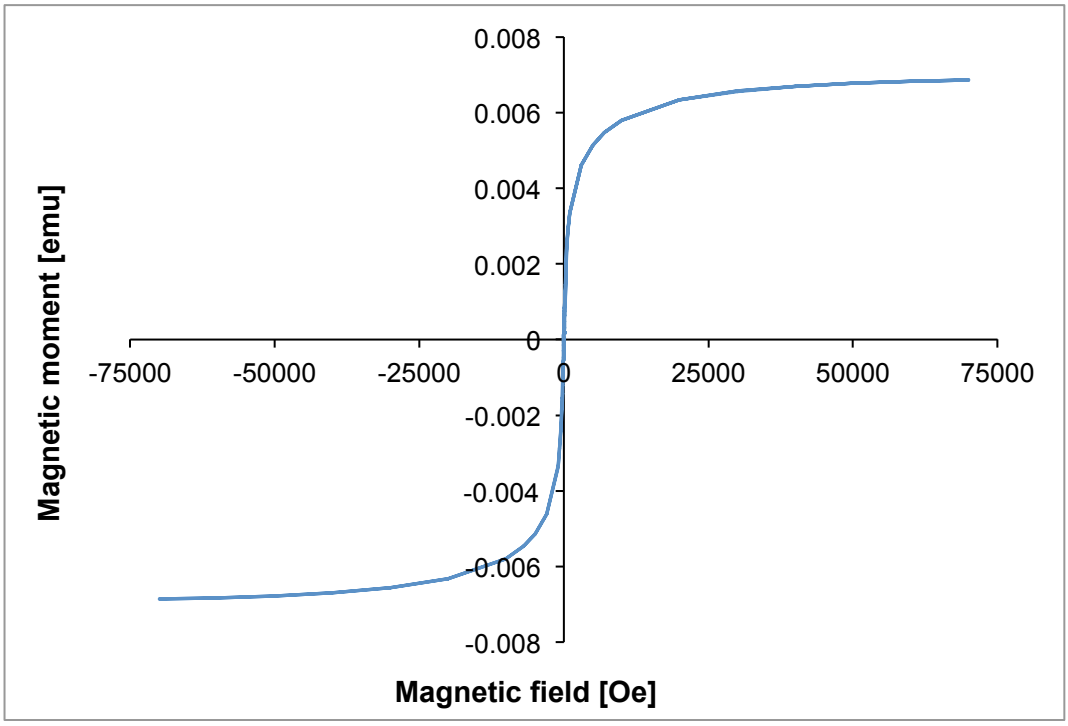

Fig. 3.10 Determined MH curves for BNF-starch 100. This MH curve represents a single measurement.

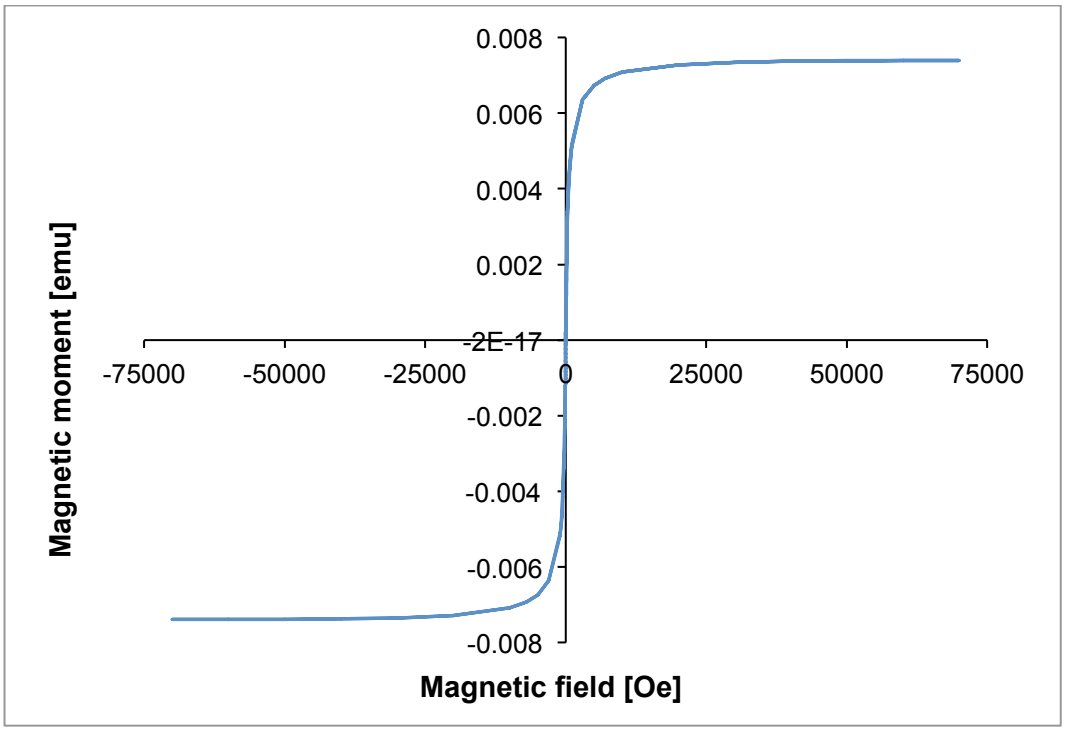

Fig. 3.11 Determined hysteresis loop for Ferucarbotran. This MH curve represents a single measurement.

3.3.5 Heating Potential

The heating potential of the nanoparticles was determined by using the Magnetic Alternating Current Hyperthermia (MACH) system, kindly provided by Dr. Paul Southern from the Royal Institution of Great Britain.

To assess the heating potential the particles were diluted according to their iron content (see Table 3.3) to 1 mg Fe/ml in dH_2O in microcentrifugation tubes. For the measurement, a temperature probe was inserted through the lid of the tube and the sample inserted into the system before it was subjected to the alternating magnetic field (AMF) with 145 V and 0.92 A applied to the coil at 1.15 MHz and peak field amplitude of 13.5 kA/m.

The temperature was recorded for 25 min resulting in a heating profile, as shown in Fig. 3.12. Afterwards the temperature probe was removed; the microcentrifugation tube sealed off and left to cool back to room temperature. This procedure was repeated twice (not shown in Fig. 3.12) for each sample resulting in three measurements per sample, from which the average and standard deviation were calculated (Fig. 3.13 and Table 3.4)

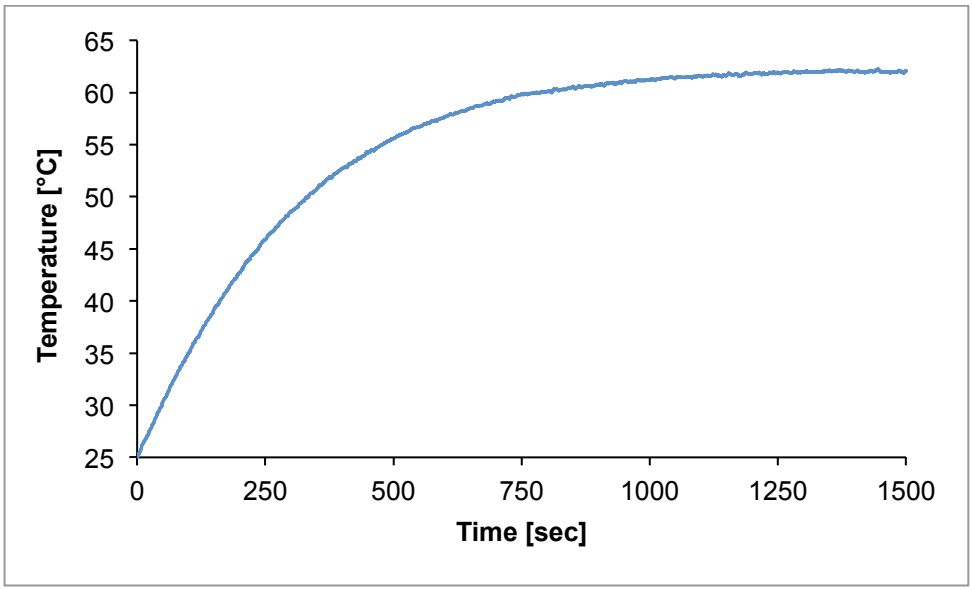

Fig. 3.12 Heating profile of Ferucarbotran (1 mg Fe/ml). Starting at room temperature, after an initial increase in temperature, the heating slowed down before it stabilized at 62 °C. This heating profile represents a single measurement.

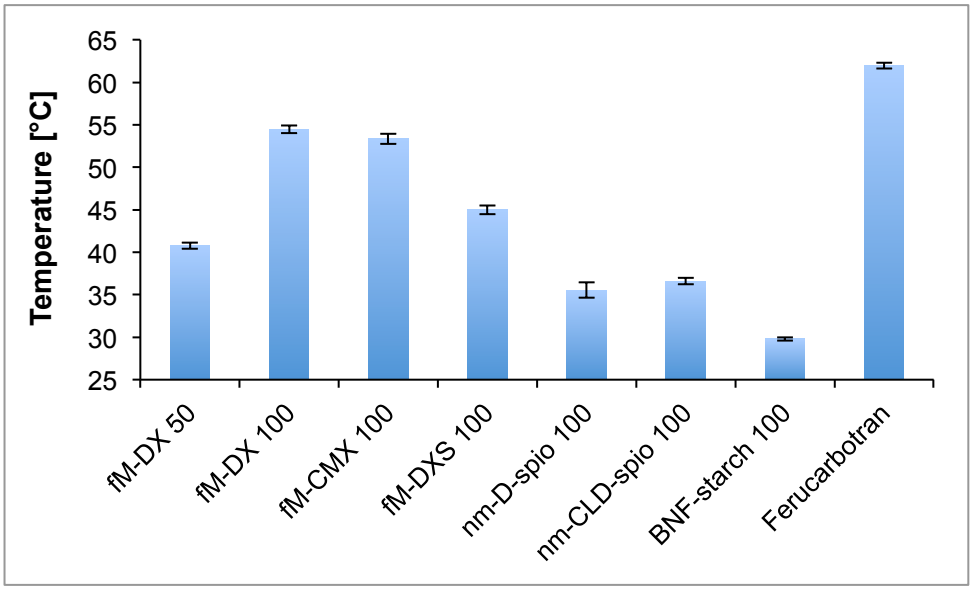

Fig. 3.13 Determined heating potentials of different nanoparticles (1 mg Fe/ml) after 25 min using the MACH system starting from 25 °C. The best heating potential was demonstrated by Ferucarbotran reaching a final temperature of 62 °C with a total temperature increase of 37 °C. fM-DX 100 and fM-CMX 100 achieved temperatures above 50 °C, while fM-DX 50, nm-d-spio 100, nm-CLD-spio 100 and BNF-starch 100 did not reach hyperthermia temperatures. (For details see Table 3.4.)

The heating profiles indicated that BNF-starch 100 was the worst heater on our system and confirmed its thermal blockage at room temperature. fM-DX 100 and fM-CMX 100 both reached temperatures above 50 °C. However, Ferucarbotran demonstrated the best heating potential reaching 62 °C.

Table 3.4 Determined heating potential of different nanoparticles at the concentration of 1 mg Fe/ml after a starting temperature of 25 °C and 25 min in the MACH system, as shown in Fig. 3.13

Sample	Temp [°C]	Std-Dev. [%]
fM-DX 50	40.8	0.9
fM-DX 100	54.5	0.8
fM-CMX 100	53.4	1.1
fM-DXS 100	45.0	1.1
nm-D-spio 100	35.5	2.5
nm-CLD-spio 100	36.6	1.1
BNF-starch 100	29.8	0.7
Ferucarbotran	62.0	0.6

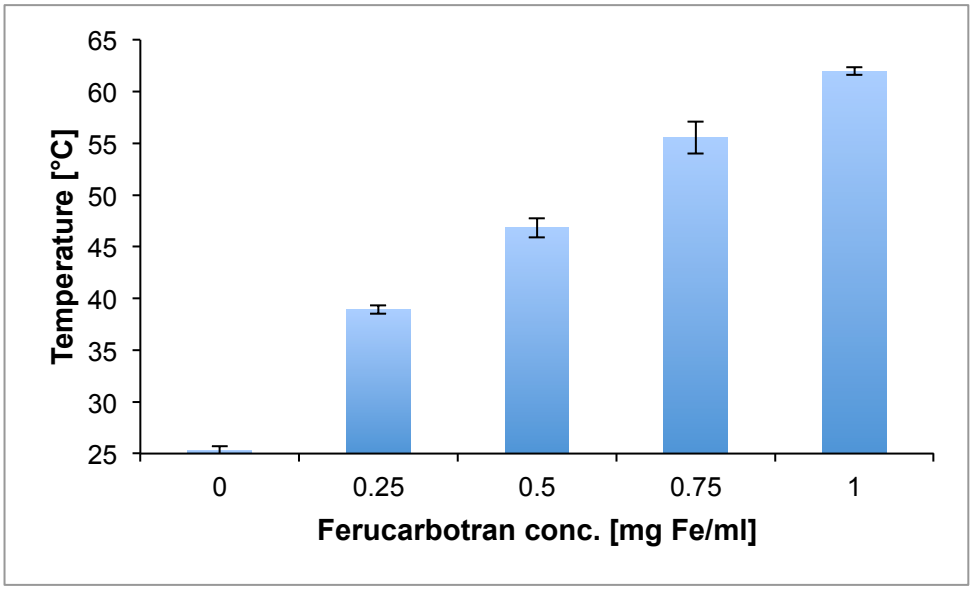

Fig. 3.14 Determined heating potential of different concentrations of Ferucarbotran, between 0-1 mg Fe/ml, after 25 min within the MACH system starting from 25 °C.

Ferucarbotran was diluted further down and additional measurements were taken with 0.25, 0.5, and 0.75 mg Fe/ml (Fig. 3.14) and, even at 0.25 mg Fe/ml, a substantial temperature increase was recorded.

Consequently, in order to be able to compare the heating potential of the nanoparticles with other nanoparticles tested in the literature, another set of hyperthermia experiments was performed using 1 ml of undiluted particles.

Depending on the shape of the resulting heating profile, for curves the Box Lucas model or for more linear data linear fits were applied to calculate the commonly used specific absorption rate (SAR) and the intrinsic loss power (ILP) [*See section:* 1.3.1.5].

The ILP is a relatively new parameter introduced by Kallumadil *et al.* (Kallumadil, Tada et al. 2009) allowing the comparison of heating profiles using different magnetic field strengths and frequencies, as SAR does not account for that.

The ILP values were calculated from the averaged temperature increases of the measurements and therefore no standard deviations are displayed in Fig. 3.15.

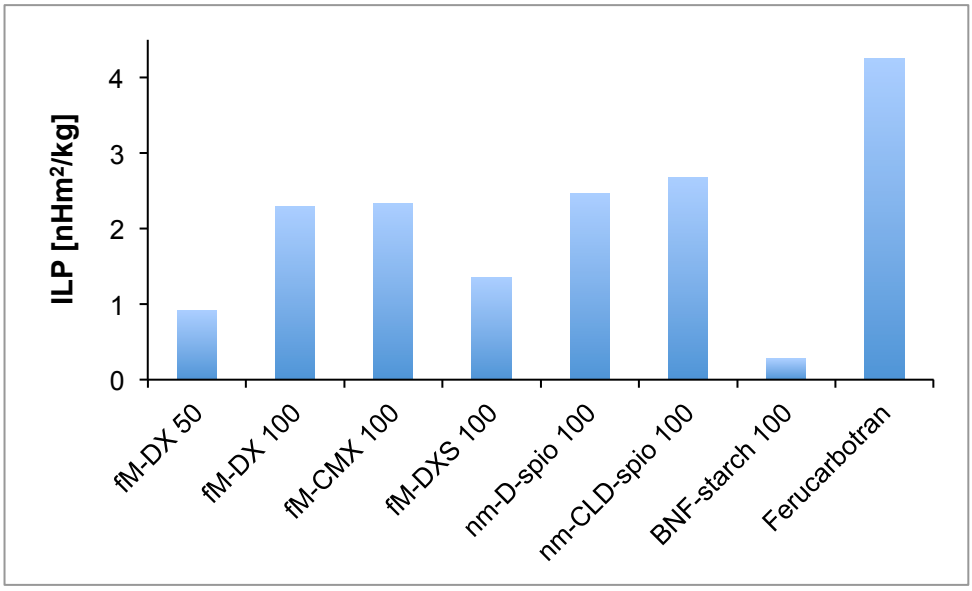

Fig. 3.15 Calculated ILP values for different nanoparticles (as shown in Table 3.5).

Interestingly, comparing the actual heating data (see Fig. 3.13) with the calculated ILP values (Fig. 3.15), nm-D-spio 100 and nm-CLD-spio 100 should have heated better than fM-DX 100 and fM-CMX 100. Still, their ILP values (see Fig. 3.15 and Table 3.5) are very similar. In contrast the ILP value for BNF-starch 100 is even lower than the heating data would suggest.

A comparison of the ILP values of nm-D-spio 100, BNF-starch 100 and Ferucarbotran (Resovist®) with the literature (Kallumadil, Tada et al. 2009) (see Table 3.5) shows that these values are comparable. However, the batch of Ferucarbotran tested in the experiments presented here seems to be more potent.

Table 3.5 Calculated SAR and ILP values

Sample	SAR [W/g]	ILP [nHm^2/kg]	ILP (Kallumadil, Tada et al. 2009)
fM-DX 50	104.25	0.92	-
fM-DX 100	260.38	2.29	-
fM-CMX 100	264.25	2.33	-
fM-DXS 100	153.39	1.35	-
nm-D-spio 100	279.83	2.46	3.12
nm-CLD-spio 100	304.38	2.68	-
BNF-starch 100	31.32	0.28	0.17
Ferucarbotran	400.60	3.53	3.1

3.4 Discussion

The aim of this study was to investigate the properties of eight commercially available nanoparticles and their heating potential to determine the most suitable candidate for therapeutic hyperthermia application.

The first characteristic to be assessed was the hydrodynamic diameter and even though all MNP samples were acquired suspended in water, only three out of the eight nanoparticles investigated tested within an acceptable size range of ±5 nm around the specified hydrodynamic diameters. In the case of fM-DX 100, the determined hydrodynamic diameter of 197 nm exceeded the intended size by 97 nm. Additionally, suspending the particles in 5 mM NaCl and PBS showed that fM-CMX 100 and fM-DXS 100 were not stable in the presence of salts. This made them unsuitable for *in vitro* or *in vivo* hyperthermia application, as aggregation affects the heating potential (Hergt, Dutz et al. 2008)

The ζ-potentials of the particles were almost neutral, as dextran is not charged, except for Ferucarbotran with a ζ-potential of -23 mV, due to its carboxylated dextran coating (Reimer and Balzer 2003). This indicated the presence of carboxyl groups on the surface of Ferucarbotran a possible target for antibody attachment.

Hydrodynamic diameter and ζ-potential are essential information for the fate of the nanoparticles *in vivo* (Mailander and Landfester 2009), while core size and structures as well its magnetic properties affect the heating potential of the nanoparticles (Gonzales-Weimuller, Zeisberger et al. 2009; Krishnan 2010; Ortega 2012).

TEM analysis of the cores revealed a variety of core structures. Chemicell particles (fM-DX 50, fM-DX 100, fM-CMX 100 and fM-DXS 100) revealed spherical cores with similar core sizes and distributions, while the particles from Micromod demonstrated a different core structure for each particle sample. Whereas nm-d-spio 100 showed spherical cores similar to the Chemicell particles, nm-CLD-spio 100 resembled miniclusters rather than isolated spheres. TEM images of BNF-starch 100 revealed a cuboid core structure, containing some as big as 50 nm, indicating thermal blockage at room temperature and requiring strong magnetic fields to induce heating, which is consistent with the literature (Bordelon, Cornejo et al. 2011).

Magnetic property analysis of the particles using SQUID showed mainly ferromagnetic and superparamagnetic responses (Pankhurst, Connolly et al. 2003; Krishnan 2010). Unfortunately, the mass of the samples analysed was not recorded, and therefore the mass of the particles (emu/g) could not be corrected to enable direct comparisons. However, the determined MH curves did reveal hyperthermia potential in some particles, such as fM-DX 100, fM-CMX 100 and Ferucarbotran.

Since MNP differ with regard to the coating to iron ratio, core composition and size, the atomic iron content was chosen as the common denominator to compare heating potentials.

The atomic iron content determined by ICP-AES and most particles corresponded with specifications provided by the manufacturer. However, two particles, fM-DX 50 and nm-D-spio 100, had a considerably lower iron content than the others. The reason for this can be found in the fact that fM-DX 50 had a substantially smaller overall hydrodynamic diameter and smaller iron oxide cores, resulting in an overall higher amount of coating present and a lower iron content.

Hyperthermia experiments, where the particles were subjected to AMF starting at room temperature (20 °C), confirmed the results of the magnetic measurements regarding the heating potential of the different particles. Ferucarbotran demonstrated the best heating rate by reaching 62 °C, at a concentration of 1 mg Fe/ml. Even with a dose as low as 0.25 mg Fe/ml a temperature of 40 °C was reached. The Chemicell particles (fM-DX 50, fM-DX 100, fM-CMX 100 and fM-DXS 100) investigated also showed respectable heating potentials reaching temperatures between 40.8 °C (fM-DX 50) and 54.5 °C (fM-DX 100). Micromod particles (nm-d-spio 100, nm-CLD-spio 100 and BNF-starch) barely achieved 36.6 °C with their best heating candidate nm-CLD-spio 100. This result was consistent with the information gained from TEM and SQUID, but renders them unsuitable for *in vivo* hyperthermia application with the MACH system.

A study by Bordelon *et al.* (Bordelon, Cornejo et al. 2011) compared BNF-starch, nm-d-spio and Feridex by subjecting them to AMF with magnetic field strengths between 8 – 97 kA/m with 650 V applied to the coil at 141 kHz. BNF-starch demonstrated substantial temperature increases subjected to magnetic field strengths between 32-90 kA/m, but at lower magnetic field strengths the results were consistent with our measurements obtained by using the MACH apparatus, providing 13.5 kA/m

at 1.15 MHz. Looking at the ILP calculated from the data provided with 0.41 nHm^2/kg is also consistent with our measurements 0.28 nHm^2/kg considering the fact that Bordelon *et al.* used a monodisperse BNF-starch suspension slightly increasing its heating potential.

All characterisation performed in this chapter established Ferucarbotran as lead candidate for hyperthermia application. Ferucarbotran, unformulated Resovist®, originally developed as an MRI contrast agent for liver (Reimer and Balzer 2003) was soon discovered by the magnetic fluid hyperthermia community (Glockl, Hergt et al. 2006; Hergt, Dutz et al. 2006) and due to its superior heating potential, which was topped only by bacterial magnetosomes (Hergt, Hiergeist et al. 2005; Hergt, Dutz et al. 2006). Ferucarbotran has been used as standard ever since in magnetic fluid hyperthermia (Kallumadil, Tada et al. 2009; Thomas, Dekker et al. 2009), but also in the development of new techniques like magnetic particle imaging (Gleich and Weizenecker 2005; Pankhurst, Thanh et al. 2009)

3.5 Summary

The aim of this study was to determine the most suitable iron oxide nanoparticles for hyperthermia application.

Eight different commercial magnetic iron oxide nanoparticles were analysed with regard to their hydrodynamic diameter, core size and structure, atomic iron content, magnetic properties and their heating potential determined.

Overall analysis established Ferucarbotran as the leading candidate and therefore it was taken forward for functionalisation.

Chapter 4

Functionalising Nanoparticles with scFv Antibody Fragments and Characterising Their Targeting Ability by Quartz Crystal Microbalance

4.1 Introduction

In the previous chapter Ferucarbotran was established as the best candidate for hyperthermia application through thorough property analysis of commercially available nanoparticles. In order to enable targeting, the aim of the work described in this chapter was to develop a method to successfully functionalize Ferucarbotran with scFv antibody fragments.

The two main scFv antibody fragments used in this thesis were shMFEm and its non-binding variant shNFEm. Both were derived from MFE-23, scFv specifically targeting the N and A1 domains of the carcinoembryonic antigen (CEA) (Boehm, Corper et al. 2000; Sainz-Pastor, Tolner et al. 2006).

CEA, a cell surface glycoprotein, was first described by Gold and Freedman (Gold and Freedman 1965) and is overexpressed in a number of different cancers, such as colorectal, lung, breast and stomach cancer, making it a prime target for antibody-directed therapy (Bates, Luo et al. 1992; Hammarstrom 1999).

MFE-23 was selected from a phage display library of anti-CEA scFvs constructed from variable region genes extracted from mice immunized with CEA (Chester, Begent et al. 1994). It has been extensively characterised (Chester, Mayer et al. 2000) and was the first murine scFv antibody fragment tested in the clinic allowing radioimmunodetection of colorectal adenocarcinoma (Meyer, Gaya et al. 2009). Additionally MFE-23 has also been investigated and used as part of the antibody-directed prodrug therapy (ADEPT) (Napier, Sharma et al. 2000; Mayer, Francis et al. 2006; Andrady, Sharma et al. 2011).

Since the negative ζ-potential of Ferucarbotran measured in the previous chapter suggested the presence of carboxyl groups on its surface, carbodiimide conjugation was the first to be evaluated. Thereby the scFv is covalently linked to the carboxyl groups within the dextran, through amines, provided by lysines present throughout the protein.

Consequently, procedures to purify the FX-scFv conjugates and to confirm the attachment of the scFv to Ferucarbotran were investigated, after which, quartz crystal microbalance (QCM) was explored to determine the functionality of the conjugate.

4.2 Objectives

The objectives of the research described in this chapter were to:

1. Functionalise Ferucarbotran with scFv antibody fragments
2. Establish method to purify the generated FX-scFv conjugates
3. Develop method to assess the functionality of the FX-scFv conjugates

4.3 Results

4.3.1 Conjugation of scFv Antibody Fragments to Ferucarbotran

4.3.1.1 Characterisation of scFv antibody fragments

shMFEm and shNFEm have been expressed in *Pichia pastoris* and were kindly provided by Dr. Berend Tolner (UCL Cancer Institute). SDS-PAGE followed by Coomassie staining and ELISA confirmed the purity, size, and immunoreactivity to CEA of shMFEm and shNFEm (Fig. 2.1). shNFEm does not bind to CEA and it is the ideal negative control, as it only differs from shMFEm by one amino acid.

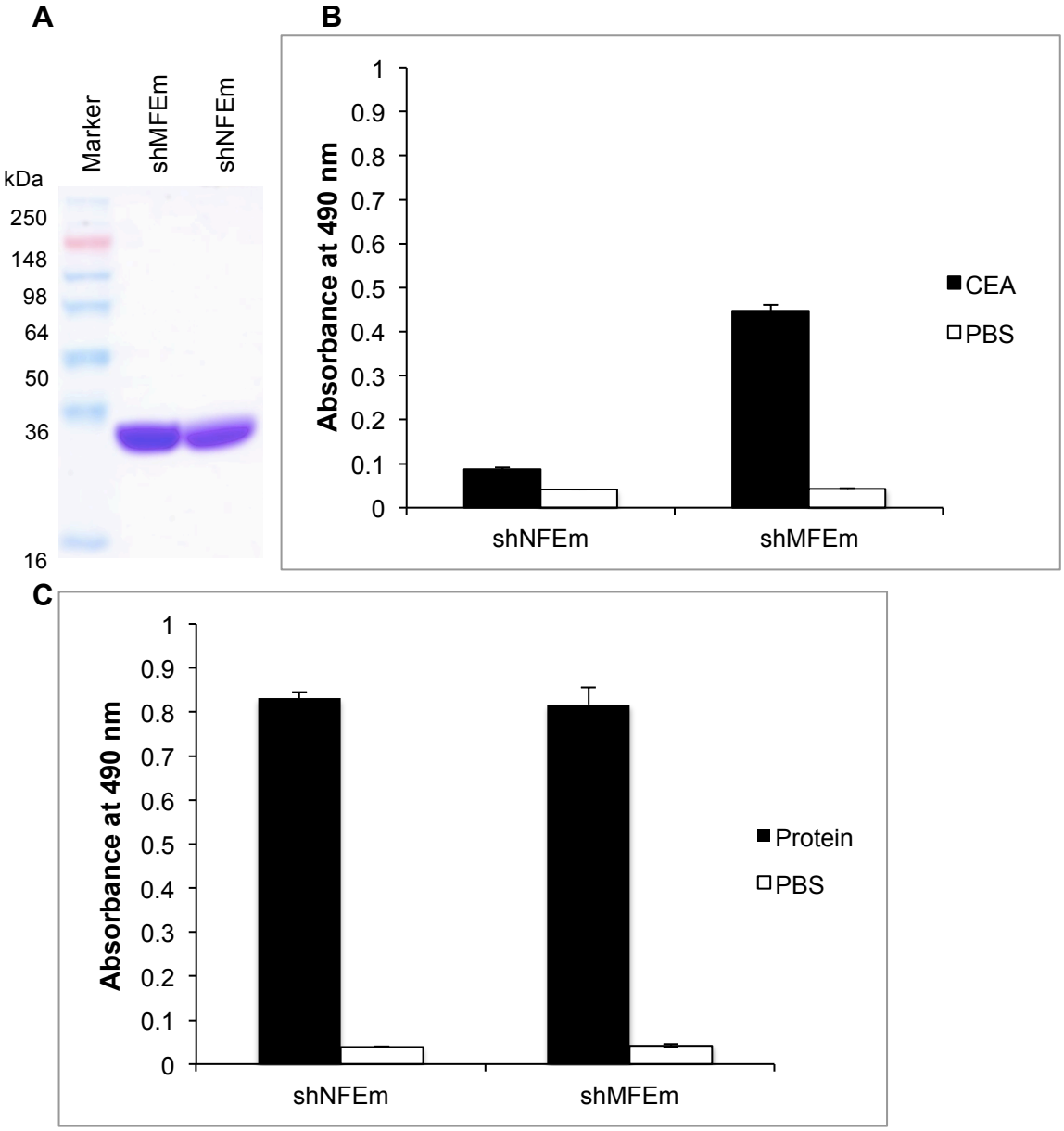

Fig. 4.1 shNFEm and shMFEm were tested for purity and binding to CEA. (A) Coomassie stained 20-4% gradient Tris glycine SDS-PAGE gel, shows the purity and size equality of shMFEm and shNFEm. (B) CEA ELISA of shMFE and shNFEm using a mouse anti-His primary antibody followed by a sheep anti-mouse HRP indicates shNFEm does not bind to CEA. To prove the presence of shNFEm, another ELISA (C) was performed, where both scFvs were immobilized directly on a 96-well plate and detected with a mouse anti-His antibody, followed by sheep anti-mouse HRP. In both ELISA PBS was used as negative control.

4.3.1.2 Stability of Ferucarbotran in Physiological Buffers

In the previous chapter (*see section:* 3.2.1), it was found that fM-CMX and fM-DXS particles were not stable in PBS and 5 mM NaCl solution, showing that different conditions can affect particle stability. This is especially important during conjugation as different buffers and pH are used, potentially altering their stability. Therefore, 1.5 mg Ferucarbotran were added to different microcentrifugation tubes containing 1.5 ml dH_2O (pH 6.4), saline (pH 7.4), PBS (pH 7.2) and 0.1 M sodium phosphate buffer (pH 8) and (pH 8.5). After 24 hrs at room temperature, the particles were put into Dynal magnetic particle concentrator for 15 min and a picture taken. This was repeated after 1 and 2 weeks (Fig 2.2).

No change in stability could be observed after 24 hrs. One week later some precipitation was recorded in the 0.1 M sodium phosphate buffers. Substantially more precipitation was noted for both Ferucarbotran suspended in saline and PBS, whereas the FX suspension in dH_2O was stable.

After two weeks, precipitation was observed in all buffers, except for dH_2O, which showed minimal precipitation. PBS appeared to cause the greatest effect on precipitation, as the change in colour indicates that most of the particles are within the precipitate.

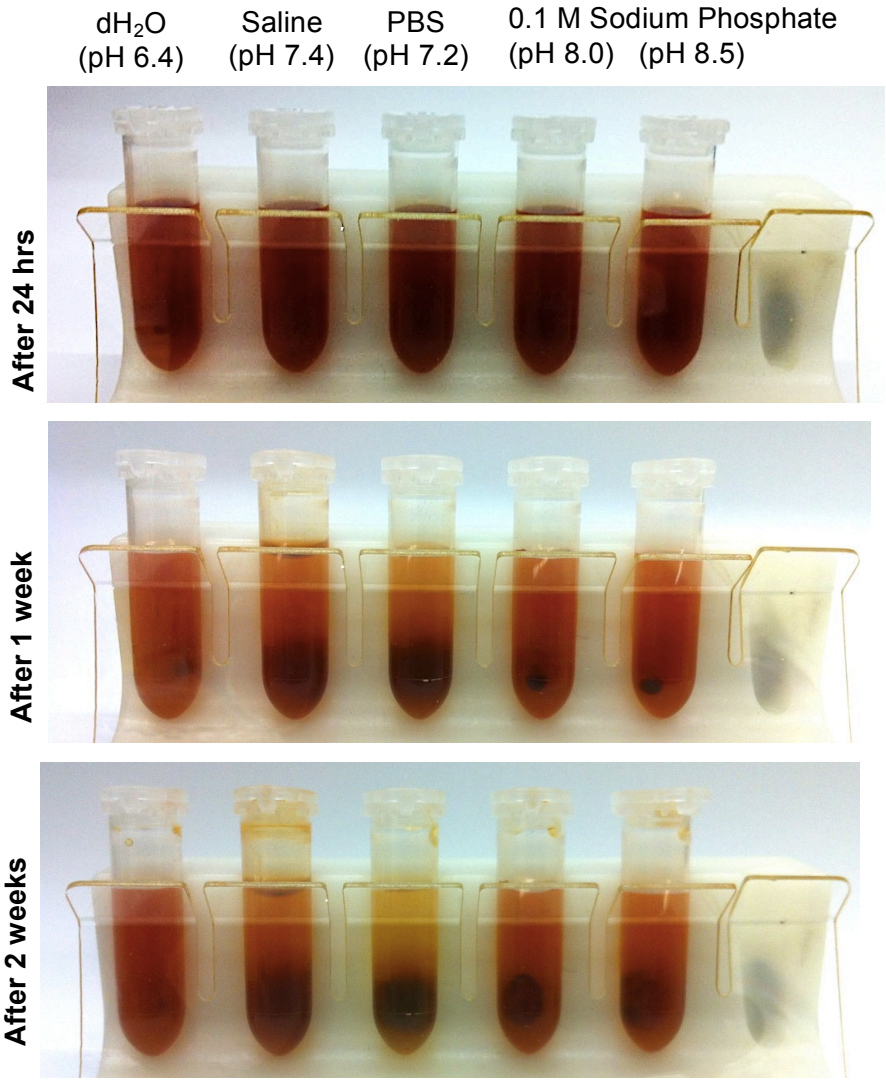

Fig. 4.2 Stability of Ferucarbotran (FX) in different buffers over the course of 2 weeks. After 24 hrs, little precipitation was observed with FX in PBS. A week later, almost all samples showed amounts of precipitation with substantial precipitation in PBS and saline and minimal precipiation in all other buffers. After two weeks, every sample showed considerable precipitation. The least amount of precipitation was observed in dH_2O.

4.3.1.3 Carbodiimide Conjugation of shMFEm to Ferucarbotran

The negative ζ-potential of Ferucarbotran, shown in the previous chapter, indicated the presence of carboxyl groups available for conjugation. Therefore carbodiimide conjugation chemistry represented schematically in Fig. 2.3 and detailed in 1.4.2 was investigated.

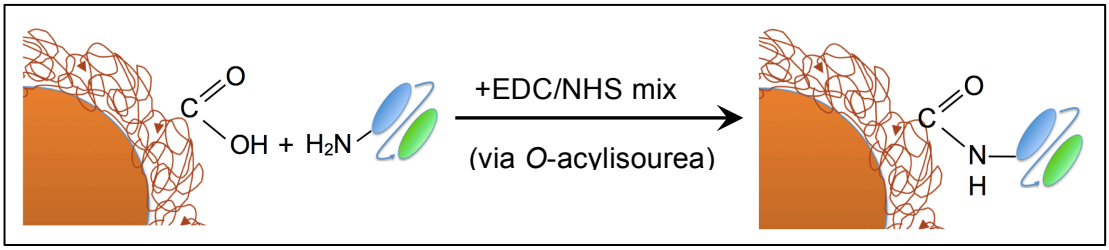

Fig. 4.3 Schematic representation of carbodiimide chemistry using 1-ethyl-3-(3-dimethylaminopropyl) carbodiimide (EDC) and N-hydroxysuccinmide (NHS).

To establish and optimise this conjugation method fM-CMX, iron oxide nanoparticles covered in carboxymethylated dextran were used, as this coating provides multiple carboxyl groups for attachment, compared to FX. However, as fM-CMX are not stable in PBS, the preferred buffer for the carbodiimide reaction. The stability of fM-CMX in 0.1 sodium phosphate buffer at pH 7.4 was tested. As the particles stayed in suspension over the course of a couple of days, a conjugation protocol to attach shMFEm to fM-CMX was established.

With the knowledge obtained about the stability of FX in PBS (*see section:* 4.3.1.2), the carbodiimide conjugation protocol for fM-CMX was applied. Although minimal precipitation was shown at 24 hrs for non-conjugated FX, shMFEm conjugated FX started to precipitate 2 hrs after the conjugation. A week later, most of the conjugated FX had dropped out of solution suggesting that the conjugation chemistry destabilized the nanoparticles.

4.3.1.4 Cyanogen Bromide Conjugation of shMFEm to Ferucarbotran

As the conjugation to carboxyl groups destabilised the Ferucarbotran, a different conjugation chemistry utilizing hydroxyl groups was investigated: cyanogen bromide conjugation (Hermanson 2008), shown schematically in Fig 2.4.

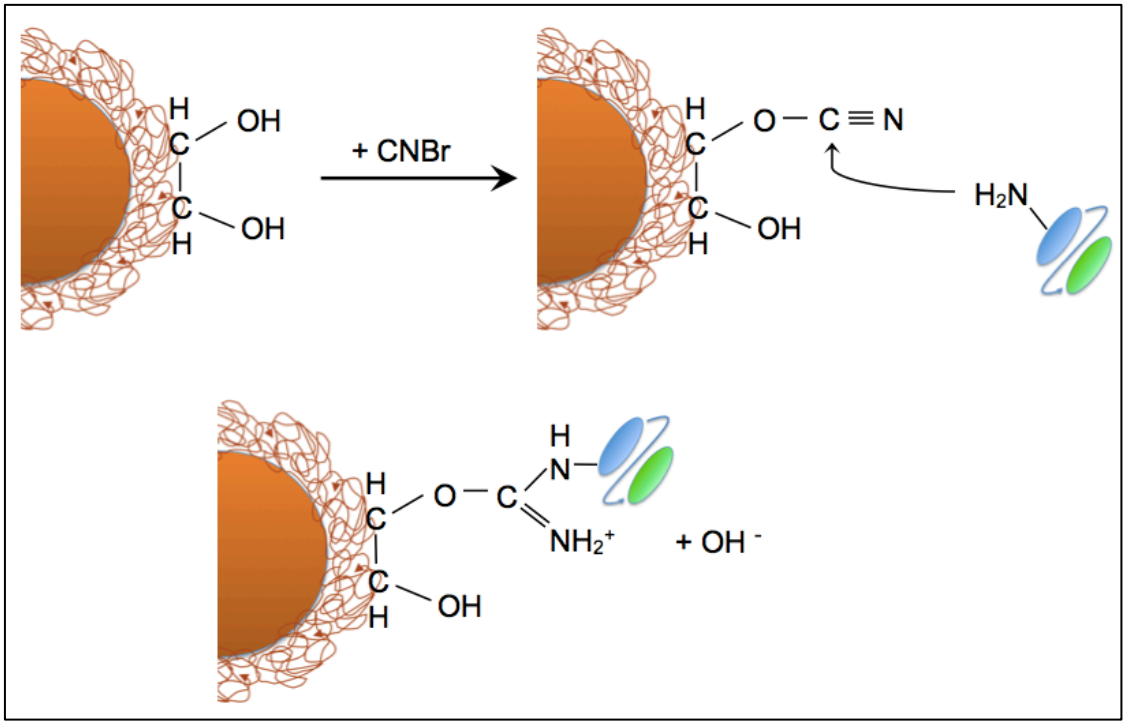

Fig. 4.4 Schematic representation of cyanogen bromide conjugation.

After conjugation, in contrast to the carbodiimide conjugation, the particle suspension seemed stable, little precipitation was observed. The conjugates were still stable a week after the conjugation. This method was therefore far superior to carbodiimide chemistry and the first successful functionalisation of FX.

4.3.2 Purification of FX-scFv Conjugates

4.3.2.1 Size Exclusion Chromatography

Concentrated Ferucarbotran behaves as a ferrofluid due to the superparamagnetic behaviour of the single domain core crystals. However, when the particles are diluted with buffer, as it is the case during conjugation, the distance between the cores increases, the magnetic interactions become weaker. Therefore, stronger magnetic field gradients are required to enable magnetic washing. These gradients cannot be achieved through magnetic separators, like the Magna-Sep™ (Invitrogen). More sophisticated, time consuming and expensive methods, like a High Gradient Magnetic Separator (Miltenyi), are required. Additionally the mass of the single particles is too small to be concentrated by centrifugation. Hence different purification methods were investigated.

One commonly used method to purify particles is dialysis, where molecules are separated by diffusion, driven by different concentrations of molecules on either side

of a membrane. It is a time consuming and expensive method, but, most importantly, unwanted substances are not effectively eliminated and only merely diluted out, which does not enable adequate analysis of the conjugates.

An alternative method found in the literature was size exclusion chromatography (SEC) (Tiefenauer, Kuhne et al. 1993; Kresse, Wagner et al. 1998; Lutz, Stiller et al. 2006). To establish a suitable SEC protocol for the purification of Ferucarbotran different column matrix (Fig. 2.5-6) and lengths (Fig. 2.7-10) were scrutinized.

Fig. 4.5 Ferucarbotran trapped in a column for size exclusion chromatography, HiPrep™ 16/60 filled with Sephacryl™ S-300 High Resolution matrix.

Unconjugated FX loaded onto a SEC column filled with Sephacryl™ S-300 High Resolution matrix showed that the particles were irreversibly trapped within the column (Fig. 4.5).

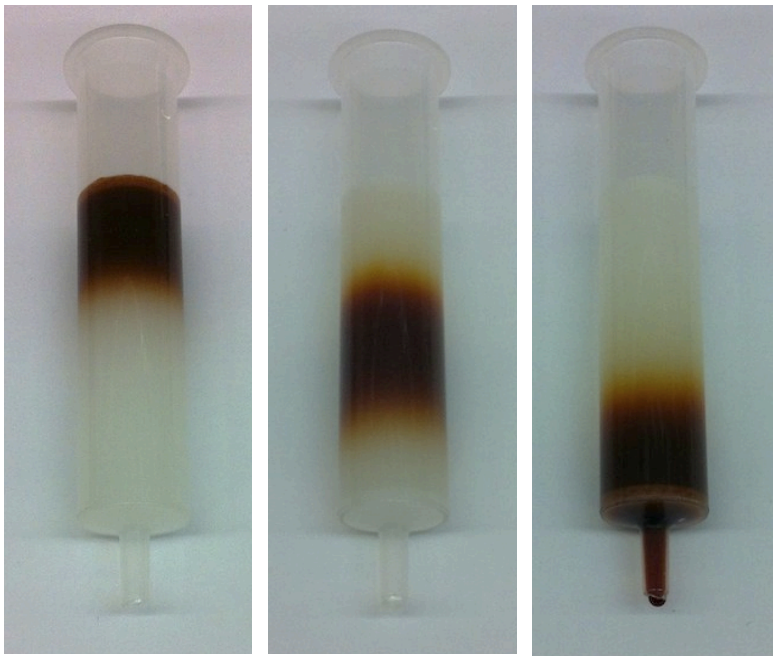

Fig. 4.6 Ferucarbotran moving through a PD-10 desalting column filled Sephadex™ G-25 and equilibrated with PBS during a cyanogen bromide conjugation.

During the conjugation process, in order to remove the excess cyanogen bromide, the activated particles were applied to a PD-10 desalting column filled with Sephadex™ G-25, a dextran matrix where the particles were able to move through easily (Fig. 4.6). Therefore Sephadex™ was investigated as separation matrix. Due to the size of shMFEm and shNFEm of 27 kDa, Sephadex™ G-100 was chosen instead of Sephadex™ G-25, with a fractionation range for globular proteins between 4 – 150 kDa.

Using the ÄKTA prime system an empty XK 16/70 column was packed with Sephadex™ G-100. To assess the quality of the packing and also to determine the volume after which the proteins leaves the column, a gel filtration protein standard was applied to the column and the SEC profile recorded (Fig. 4.7)

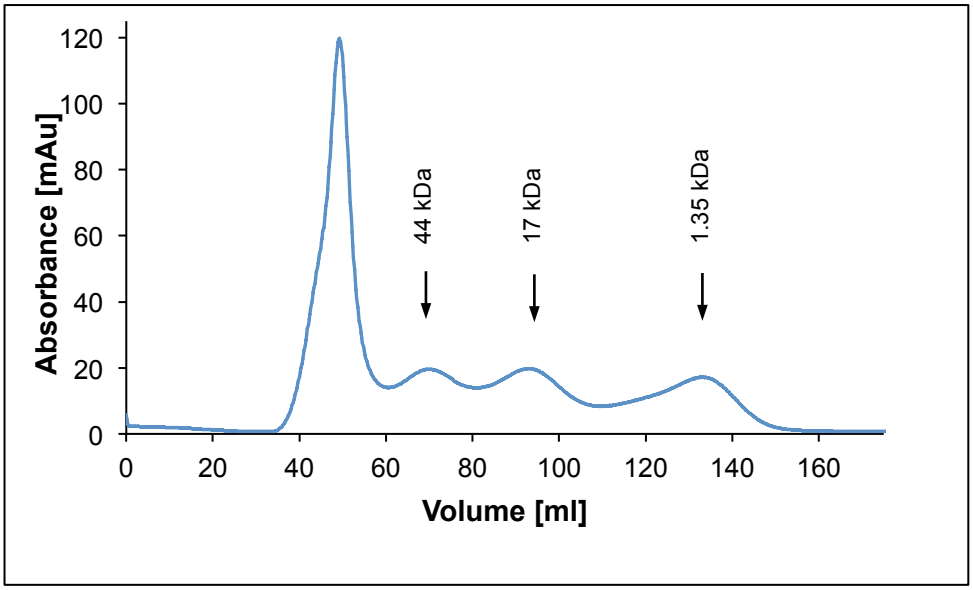

Fig. 4.7 SEC profile of gel filtration protein standard running through a XK 16/70 column filled with Sephadex™ G-100 at flow rate 0.5 ml/min in PBS elution buffer. Proteins bigger than 100 kDa, the purification limit of Sephadex™ G-100, come off the column in the 'void' marking the big peak after the first 35 ml buffer passed through the column. The little distance and overlap between peaks indicates the need for a longer column to gain a better resolution. This SEC profile represents a single measurement.

Consequently, in a second run, 1 ml PBS containing 5 mg unconjugated Ferucarbotran were applied to the column to determine the location and width of the particle peak (Fig. 4.8). It was found that the particles were trailing into the range where the scFv fragments were expected to leave the matrix. Therefore, in order to

achieve a clear separation between conjugate and free antibody, a longer column length had to be chosen.

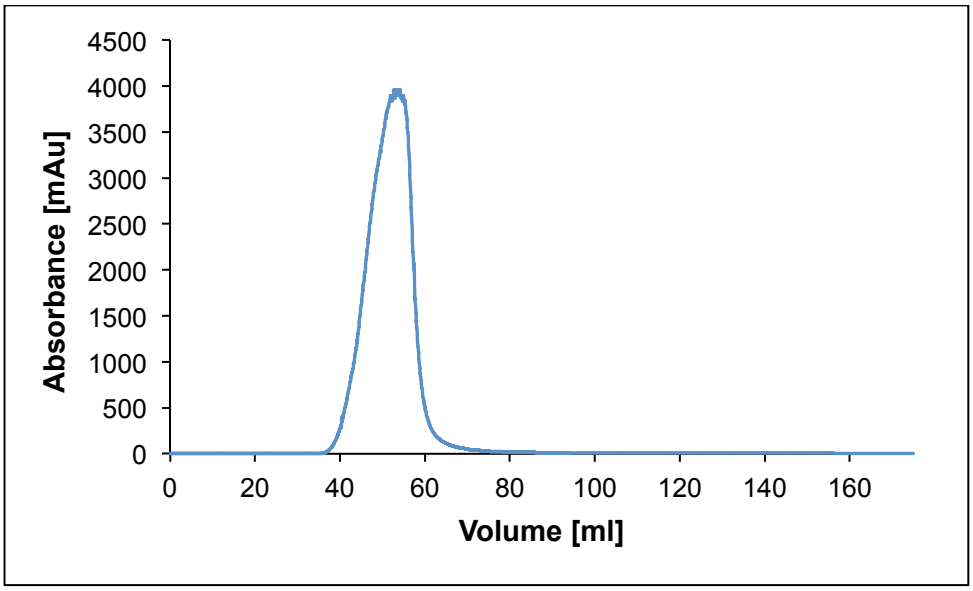

Fig. 4.8 SEC profile of Ferucarbotran running through a XK 16/70 column filled with Sephadex™ G-100 at flow rate 0.5 ml /min in PBS elution buffer. Ferucarbotran came off the column as part of the void, as it is bigger than 100 kDa, the purification limit of Sephadex™ G-100. This SEC profile represents a single measurement.

An XK 16/100 column was packed with Sephadex™ G-100 and the applied gel filtration standard (Fig. 4.9) revealed a clearer separation of the proteins and an expected peak for shMFEm after about 125 ml. Another run of unconjugated Ferucarbotran (Fig. 4.10) showed that the majority of particles were leaving the matrix after 70 – 90 ml elution buffer. So for the first run of Ferucarbotran functionalized with shMFEm (FX-shMFEm) only fractions between 70 – 85 ml were collected (Fig. 4.11) preventing an overlap with free scFv.

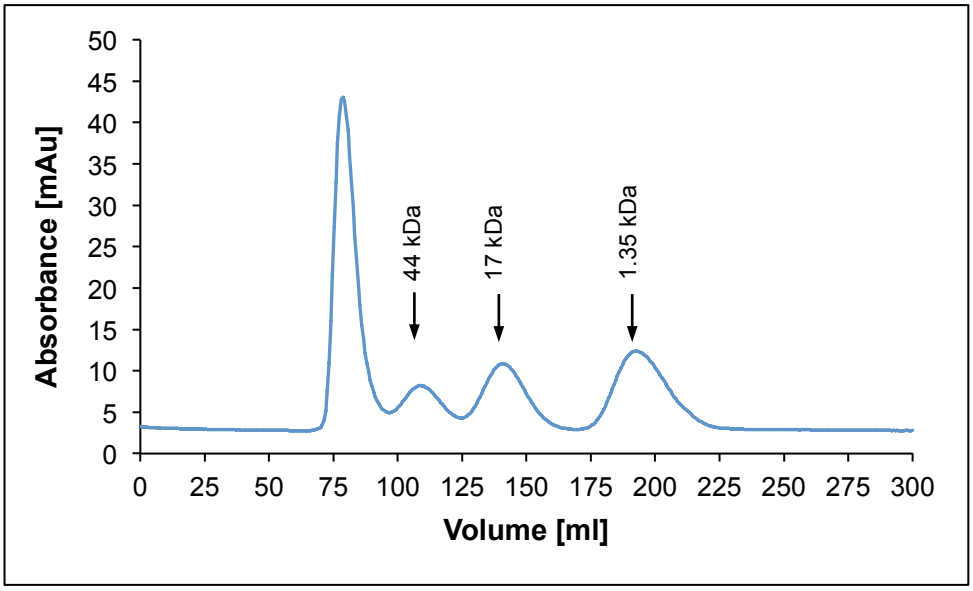

Fig. 4.9 SEC profile of gel filtration protein standard running through a XK 16/100 column filled with Sephadex™ G-100 at flow rate 0.5 ml /min in PBS elution buffer. Proteins bigger than 100 kDa, the purification limit of Sephadex™ G-100, come off the column in the 'void' marking the big peak after the first 70 ml buffer passed through the column. The distinct peaks indicated that the column was well packed and ready to purify samples. This SEC profile represents a single measurement.

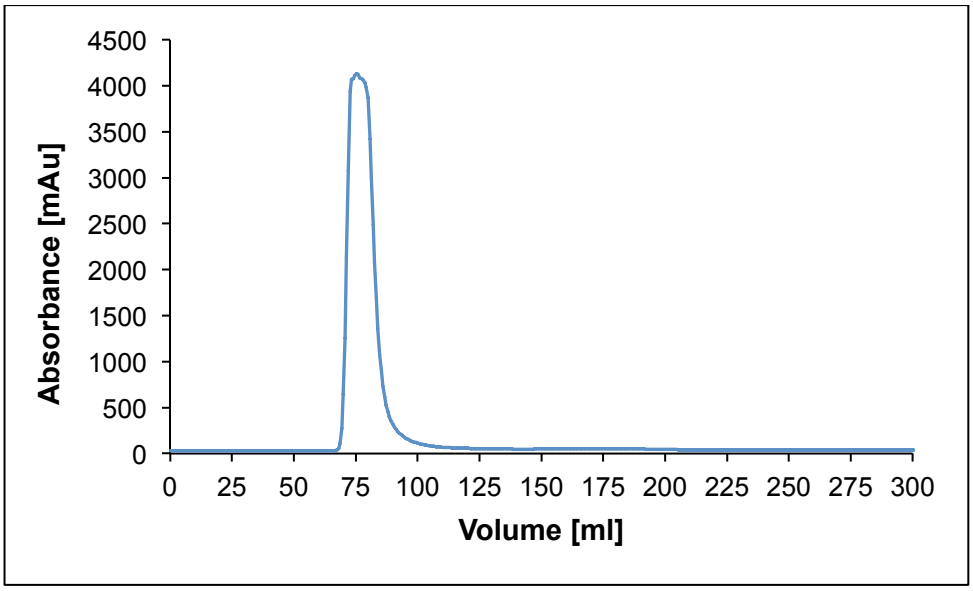

Fig. 4.10 SEC profile of Ferucarbotran running through a XK 16/100 column filled with Sephadex™ G-100 at flow rate 0.5 ml /min in PBS elution buffer. Ferucarbotran came off the column as part of the void, as it is bigger than 100 kDa, the purification limit of Sephadex™ G-100. This SEC profile represents a single measurement.

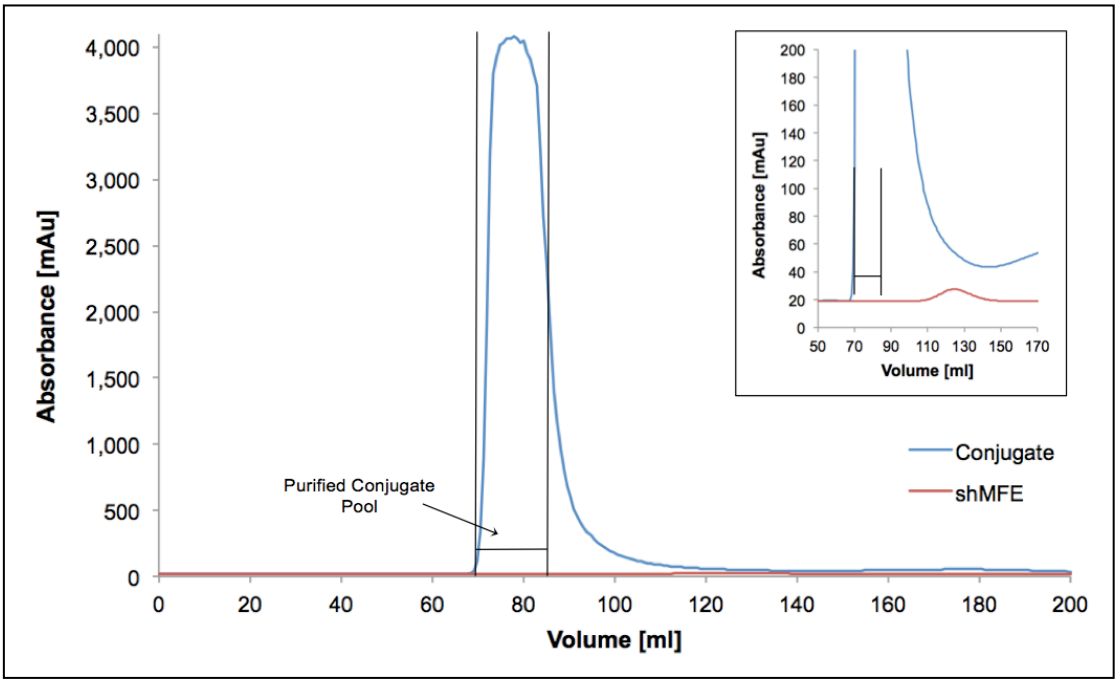

Fig. 4.11 SEC profile of purified FX-shMFEm conjugates. To avoid contamination of the conjugates with unbound shMFEm, only fractions between 70 – 85 ml were collected and pooled. The inset shows a magnified view of the base of the conjugate 'void' peak (blue line), with the collected conjugate fractions with 20 ml volume 'distance' to the shMFEm elution peak (red line)

4.3.2.2 Concentration of the Purified FX-scFv Conjugate Pool

After eluting off the SEC column, the concentration of the conjugates was below 0.5 mg/ml, so a method to re-concentrate them had to be established. Millipore Amicon Ultra-4 centrifugal filter units and Millipore Centriprep YM-50 were investigated.

Amicon Ultra-4 centrifugal filter units were not suitable, as particles got stuck to the filter, which resulted in a considerable loss of conjugate, whereas the Centriprep YM-50 filter membrane did not interact with particles minimalizing the loss of conjugate.

4.3.2.3 Determining the Purity of FX-scFv Conjugates

To demonstrate the purity of the FX-scFv conjugates, a western blot (Fig 2.12) was performed.

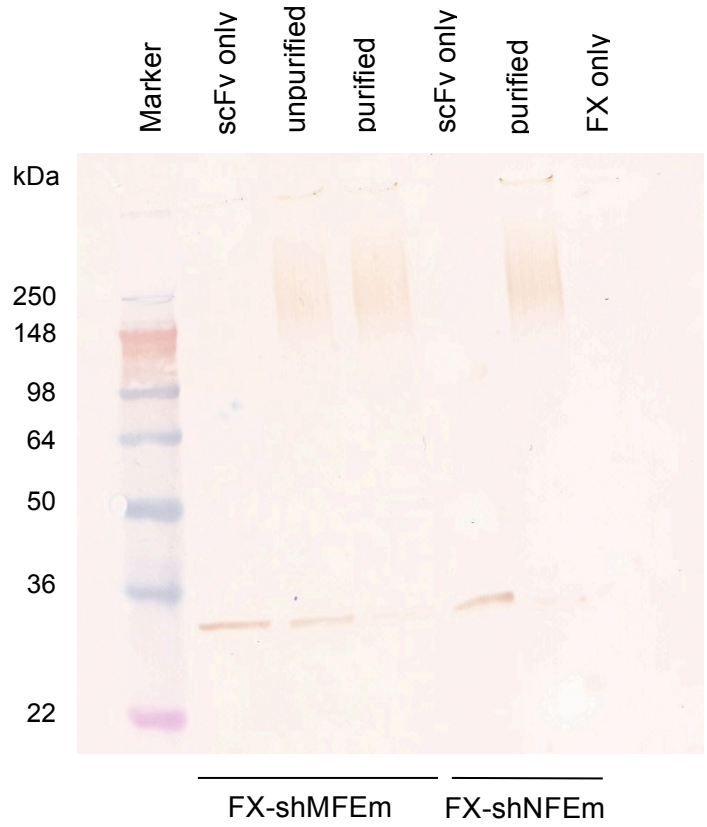

Fig. 4.12 Western blot using an anti-His Ab showing samples of purified FX-shMFEm and FX-shNFEm conjugates. In all functionalised particle samples a smear from the particles can be seen as well as faint band at the same size of the scFv.

The faint bands in the western blot (Fig. 4.12) suggested that the purification was not successful. However dissection of the procedure leading to this western blot indicated a different cause for the bands. Samples had been boiled for 4 min at 90 °C under reducing conditions before they were applied on a precast SDS-PAGE gel, which could have destroyed the link between particle and scFv. Therefore a native PAGE gel was cast and samples from the same conjugation experiments were run without boiling and under non-reducing conditions followed by an ECL western blot (Fig. 4.13).

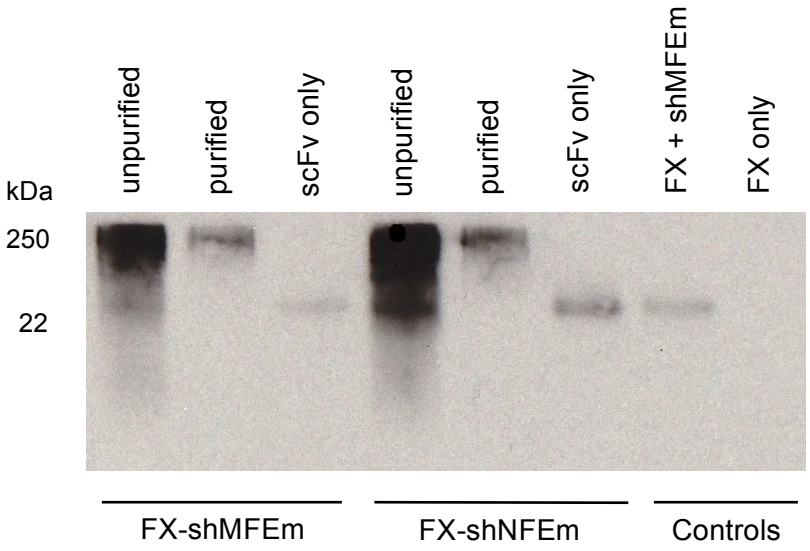

Fig. 4.13 ECL western blot using an anti-His Ab showing samples of the FX-shMFEm and FX-shNFEm conjugates before and after purification. Both unpurified samples show a band at the same size as the corresponding scFv, while no bands at this size were observed. Controls indicate no interaction of anti-His Ab with the FX on its own, demonstrating successful purification.

In the unpurified samples, a smear from the particles can be seen as well as faint band at the same size of the scFv. Purified samples show the conjugates stuck at the top of the gel and controls confirm that nanoparticles without scFv attached to their surface cannot be detected by an anti-His Ab.

4.3.3 Characterisation of FX-scFv Conjugates

4.3.3.1 Antibody Presence of FX-scFv conjugates

After successful purification and concentration of the conjugates, ELISA confirmed the presence of scFv on the suface of the FX-scFv, where the conjugates and the corresponding controls were directly immobilized on a 96-well MaxiSorp™ plate and consequently treated with an anti-His or anti-dextran antibody. It is important to point out that MaxiSorp™ (according to the manufacturer's homepage (Nunc)) is a modified polystyrene surface with high affinity to polar groups and therefore proteins.

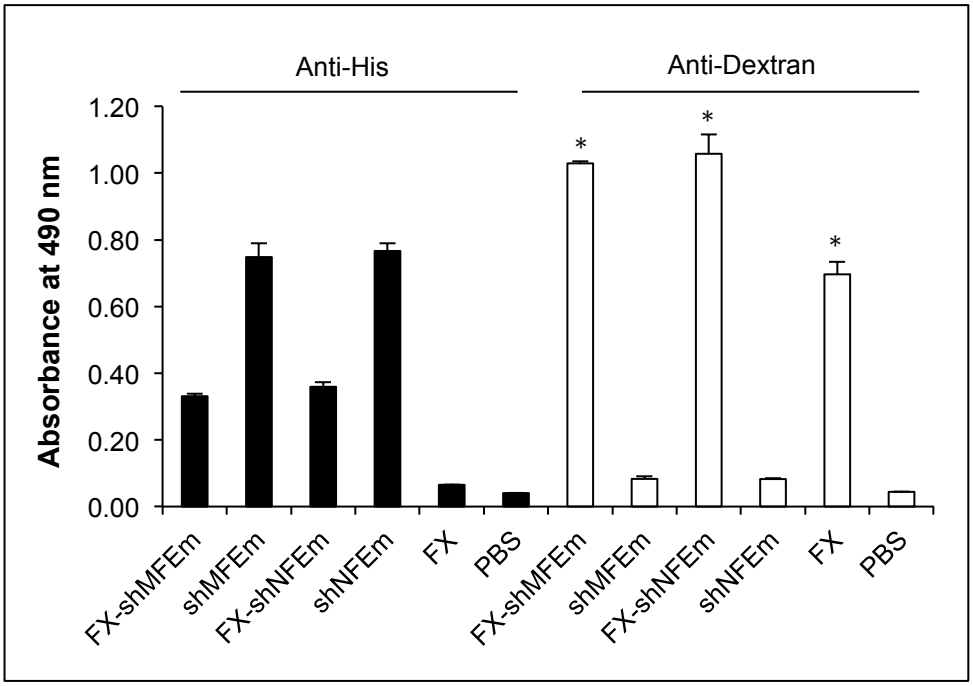

Fig. 4.14 Determination of the presence of scFv on FX-scFv conjugates by ELISA. FX-shMFEm and FX-shNFEm were immobilized directly on a 96-well MaxiSorp™ plate (Nunc) and detected with a mouse anti-His or mouse anti-dextran antibody, followed by sheep anti-mouse HRP. PBS was used as negative control.

A closer look at the anti-dextran results in Fig. 4.14 show that substantially more particles can be detected in the conjugate carrying lanes, than in the pure FX lane, as the attached protein within the coating allows the particles to interact better with the MaxiSorp™ plate confirming the presence of scFv on the particles.

4.3.3.2 Binding Affinity of scFv and SPION-scFv

To determine the binding affinity of the conjugated antibody fragments quartz crystal microbalance (QCM), in collaboration with Attana SA, was explored.

In the first set of experiments, the binding kinetics of shMFEm and shNFEm were determined, by immobilising the scFvs onto two carboxyl sensor chips. Consequently, the sensor chips were treated with different concentrations of the cognate antigen NA1, resulting in the interaction profiles shown in Fig. 4.14. This clearly showed NA1 binding to shMFEm, while barely any interacting with shNFEm.

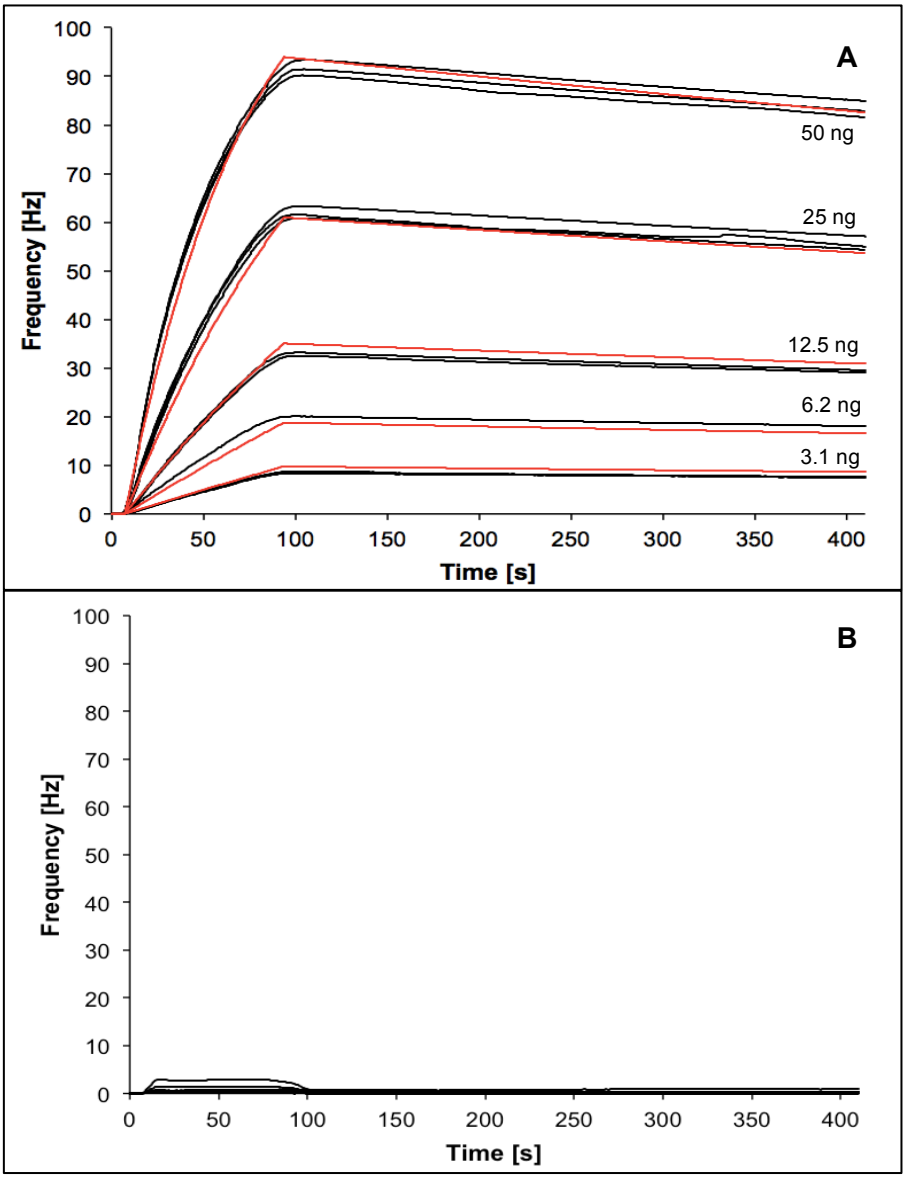

Fig. 4.15 (A) Interaction profile of immobilized shMFEm with different concentrations of NA1 ranging from 3.1 to 50 ng/ml. (B) Reference chip carrying shNFEm subjected to the same concentrations of NA1. While each black line indicates a single measurement, each red line represent the best calculated fit for this particular concentration.

Next the two conjugates FX-shMFEm and FX-shNFEm were immobilised on two polystyrene sensor chips and treated with the same concentrations of NA1 ranging from 6.2 to 50 ng/ml.

The resulting interaction profiles (Fig. 4.15) also showed that the NA1 was binding to the FX-shMFEm conjugate, while only little interaction with the negative control, the FX-shNFEm conjugate. The little interaction observed could be due to mass transfer, as 50 ng NA1 is quite a high concentration in a QCM experiment (Personal comment

for reasonings derived from conversation with Attana application specialists Liselotte Kaiser and Staffan Grenklo).

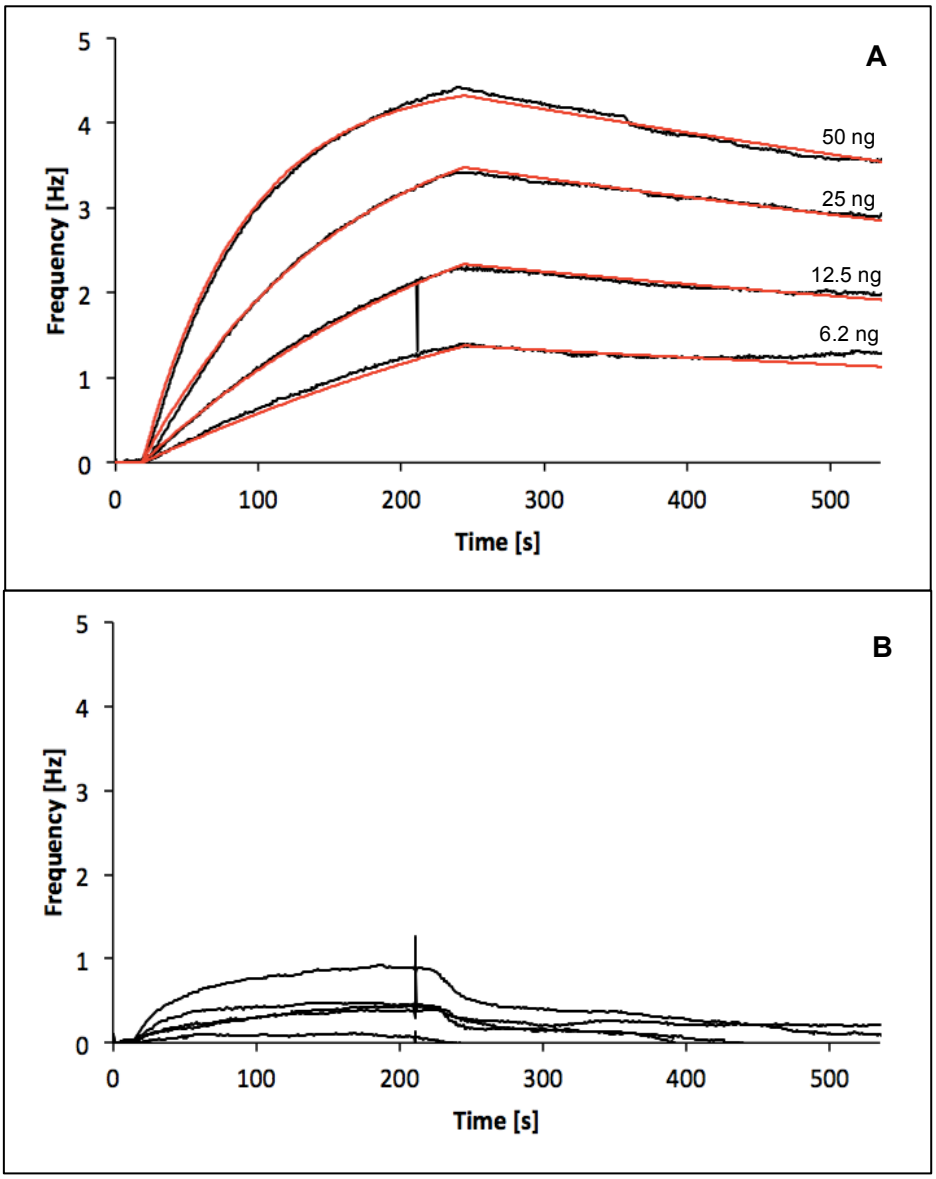

Fig. 4.16 (A) Interaction profile of captured FX-shMFEm conjugates subjected to different concentrations of NA1 ranging from 6.2 to 50 ng/ml. (B) Reference channel showing the interaction profile of FX-shNFEm conjugate with NA1. While each black line indicates a single measurement, each red line represent the best calculated fit for this particular concentration.

Table 4.1 Key values describing the interactions from Fig. 4.15 and Fig. 4.16

	shMFEm	FX-shMFEm
Association rate constant k_a [M^{-1} s^{-1}]	9.07E+3 ±2	7.31E+3 ±6
Dissociation rate constant k_d [s^{-1}]	4.01E-4 ±3E-6	7.01E-4 ±8E-7
Dissociation constant KD [M]	4.42E-8 ±3E-10	9.6E-8 ±1E-10

The association rate constant, k_a, in Table 4.1 shows that antigen is attaching to the scFv on the particles at a slightly slower rate compared to the native scFv, while in contrast the dissociation is almost twice as fast resulting in a significantly lower binding affinity.

4.3.4 Site-specific attachment of shMFEm to Ferucarbotran

Additionally to carbodiimide and cyanogen bromide conjugation another attachment route was investigated: site-specific attachment.

Carbodiimide and cyanogen bromide conjugation chemistries both aim to attach a protein via available amine groups found throughout the structure (Fig 4.17), in contrast to site-specific attachment utilizing a functional group found only once within the structure in a particular location, such as a cysteine tag.

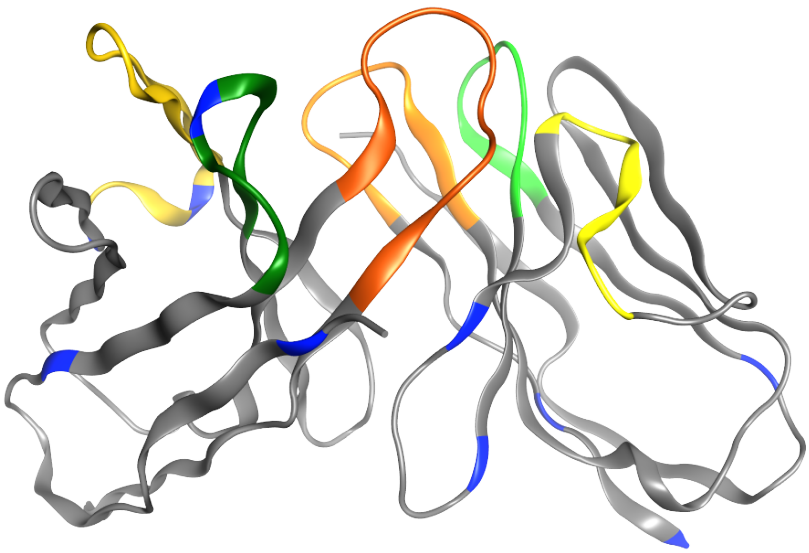

Fig. 4.17 Structure of MFE-23 (Boehm, Corper et al. 2000). Available amines provided through lysines were highlighted in blue, while yellow, orange, and green represent complementary determining regions (CDR). This illustrative model was kindly provided by Paul. J. Gane.

4.3.4.1 shMFEm-Cys

To enable site-specific attachment, a cysteine tag was engineered into the structure of shMFEm. shMFEm-Cys has been expressed in *Pichia pastoris* and was kindly provided by Dr. Berend Tolner (UCL Cancer Institute).

The profile from the protein purification by the size exclusion chromatography (Fig. 4.18) showed two peaks, which were collected separately as Pool 1 and 2 indicated in the figure.

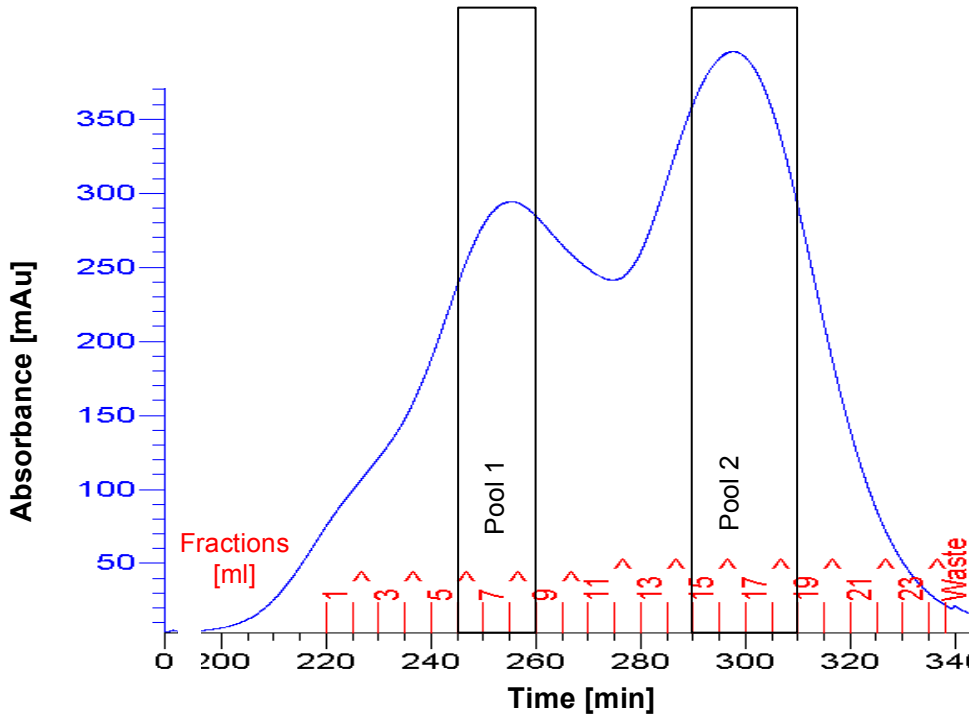

Fig. 4.18 SEC profile of shMFEm-Cys showing two peaks suggesting the presence of dimers and monomers. Fractions 6-9 ml were combined as Pool 1, while fractions 15-19 ml were combined as Pool 2. This SEC profile represents a single measurement.

Since multiple peaks often indicate dimerization, samples from both pooled scFv fractions were run on an SDS-PAGE followed by Coomassie staining (Fig. 4.19).

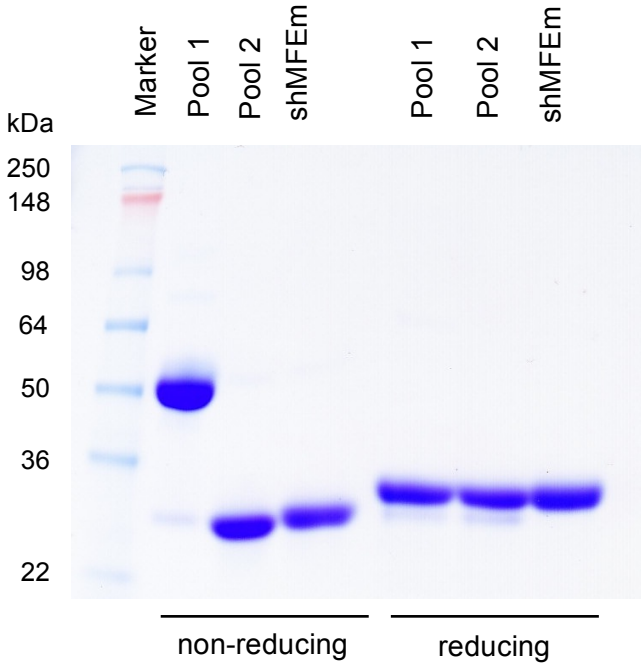

Fig. 4.19 Pooled fractions taken from different SEC peaks were tested for puritiy by a Coomassie stained 4-20% gradient Tris glycine SDS-PAGE gel under reducing and non-reducing conditions. shMFEm was used a positive control. The thick band of Pool 1 at around 50 kDa under non-reducing conditions indicated that the these pooled fractions mainly consisted of dimer, while the band of pool 2 around 27 kDa suggested primarily monomers.

4.3.4.2 Site-specific attachment of shMFEm-Cys to Ferucarbotran

In order to conjugate shMFEm-Cys via its cysteine tag, two conjugation chemistries had to be combined. First, sodium periodate chemistry was used to attach the maleimide linker BMPH to Ferucarbotran and, in a second conjugation step, the maleimide reacted with the available cysteine within shMFEm-Cys forming a thiol bond.

For attachment of the maleimide linker 10 mg sodium periodate were dissolved in 800 ul of a 50 mM sodium borate buffer (pH 8.5). 10 mg Ferucarbotran nanoparticle suspension were added and incubated on the roto-torque for 25 min at room temperature wrapped in foil, as this step is light sensitive. To stop the reaction and remove the excess sodium periodate the particles were run through the PD-10 equilibrated with 50 mM sodium borate buffer. The particles were collected in a fresh

2 ml micro centrifugation tube before immediately 10 mg maleimide linker BMPH were added and suspended in the particle mix. The mix was incubated on the roto-torque for two hours before 200 µl of 5 M sodium cyanoborohydride in 1 M NaOH were added. Consequently, the suspension was incubated o/n on the roto-torque at RT. On the next day, 100 µl of a 0.1 M glycine in 50 mM sodium borate buffer (pH 8.5) solution were added and the mix incubated for another hour on the roto-torque in order to block the unreacted sites.

The maleimide was activated, by running the particle mix through a PD-10 column equilibrated with 50 mM sodium borate buffer (pH 7). 100 µg shMFEm-Cys were added to the nanoparticles and mixture incubated on the roto-torque o/n.
Subsequently 100 µl of a 0.1 M cysteine in 50 mM sodium borate buffer (pH 8.5) solution were added and the mix incubated for another hour on the roto-torque before it was stored for purification and analysis at 4 °C.

4.3.4.3 Purification of the FX-shMFEm-Cys

The FX-shMFEm-Cys conjugates were concentrated using a Centriprep YM-50 and purified by size exclusion chromatography, as shown in Fig. 4.20.

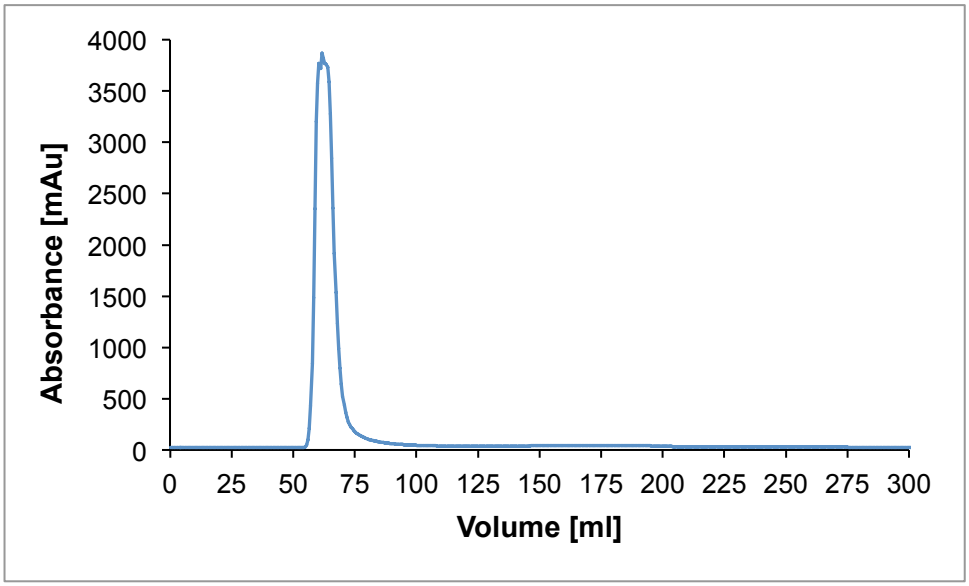

Fig. 4.20 SEC profile of FX-shMFEm-Cys running through a XK 16/100 column filled with Sephadex™ G-100 at flow rate 0.5 ml /min in PBS elution buffer. FX-shMFEm-Cys came off the column as part of the void, as it is bigger than 100 kDa, the purification limit of Sephadex™ G-100. Fractions were collected between 55 – 65 ml elution volume to avoid contamination with the unbound shMFEm-Cys. This SEC profile represents a single measurement.

The collected fractions were again concentrated using a Centriprep YM-50 before their purity was evaluated by SDS-PAGE followed by ECL western blot (Fig. 4.21)

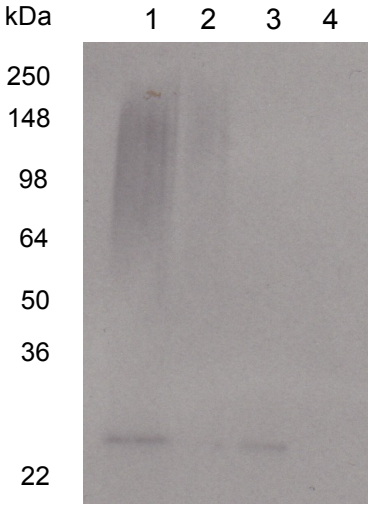

Fig. 4.21 ECL western blot using an anti-His Ab showing FX-shMFEm-Cys before (1) and after (2) purification with shMFEm-Cys (3) and unconjugated FX (4) as controls. SDS-PAGE was performed using 4-20% gradient Tris glycine gel for this western blot. This explains the long particle smears seen in lane 1 and 2, as FX is not a monodisperse particle suspension. A clear band can be seen in lanes 1 and 3, but not in lane 2 indicating a successful purification.

4.3.4.4 Analysis of FX-shMFEm-Cys Conjugates

After successful purification and concentration of the conjugates, ELISA confirmed the presence of shMFEm-Cys on the surface of the FX-shMFEm-Cys conjugates. For this ELISA, conjugates and corresponding controls were directly immobilized on a 96-well MaxiSorp™ plate and consequently treated with an anti-His or anti-dextran antibody (*see section:* 4.3.3.1).

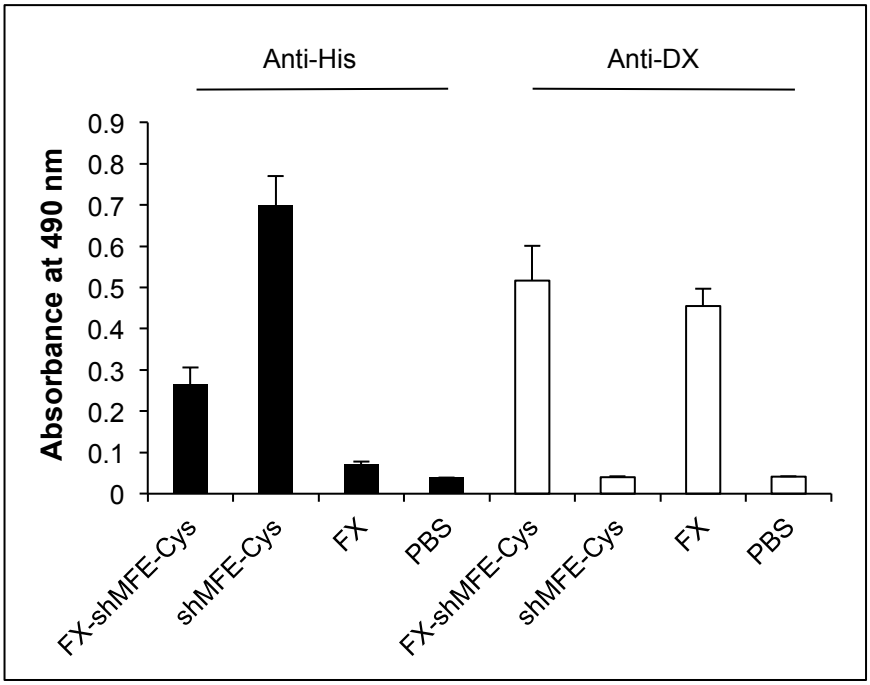

Fig. 4.22 Determination of the presence of scFv on the surface of the FX-scFv conjugates by ELISA. FX-shMFEm and FX-shNFEm were immobilized directly on a 96-well maxisorp plate and detected with a mouse anti-His antibody or mouse anti-dextran antibody, followed by sheep anti-mouse HRP. PBS was used as negative control.

In Figure 4.22, the anti-His antibody confirmed the presence of shMFEm-Cys on the surface of Ferucarbotran. However, a closer look at the anti-dextran results in the same figure showed only slightly more particles were detected in the conjugate carrying lane, than in the pure FX lane (detected with the anti-DX antibody). As the attached protein within the coating allows the particles to interact better with the MaxiSorp™ plate, the FX-shMFEm-Cys conjugates should have bound better in comparision to the pure FX yielding a higher signal.

4.4 Discussion

This chapter investigated the stable functionalisation of Ferucarbotran with scFv antibody fragments shMFEm and shNFEm. Different conjugation chemistries and strategies were evaluated. The FX-scFv conjugates were purified, concentrated, and analysed for their targeting ability.

In the previous chapter, in order to determine the hydrodynamic diameter and ζ-potential, particles were suspended for a short amount of time in dH2O, PBS, and 5 mM NaCl. Even though the particles were analysed immediately after suspension in the different buffers, it was shown that some particles (fM-CMX and fM-DXS) were not stable in PBS or 5 mM NaCl. While no immediate precipitation was observed with Ferucarbotran, for any applications these particles might have to be stored for at least week. Therefore, stability of Ferucarbotran in dH_2O (pH 6.4), saline (pH 7.4), PBS (pH 7.2), and 0.1 M sodium phosphate buffer (pH 8 and pH 8.5) was examined. Although no change in stability could be observed after 24 hrs, after one week minor precipitation was recorded in the 0.1 M phosphate buffer samples and considerably more precipitation in PBS. One week later, precipitation was observed in all buffers, with the most precipitate in the PBS samples and the least in dH_2O. These results lead to the conclusion that Ferucarbotran should be stored in dH_2O or 0.1 M phosphate- buffer, but PBS, as a storage buffer should be avoided, if possible.

Since the negative ζ-potential of Ferucarbotran (-23 mV) in the previous chapter indicated the presence of carboxyl groups, carbodiimide chemistry (DeNardo, DeNardo et al. 2005) was the first to be investigated for the attachment of shMFEm and shNFEm to Ferucarbotran.

Carboxyl groups on the nanoparticles are activated by the addition of 1-ethyl-3-(dimethylaminopropyl)carbodiimide (EDC) to form an *O*-acylisourea intermediate, which then reacts with accessible amines provided by lysines within the structure of an antibody or scFv antibody fragment. The reaction efficiency of this process is improved through the addition of *N*-hydroxysuccinimide (NHS), which stabilises the *O*-acylisourea intermediate through the formation of a succinimide ester. (Hermanson 2008)

First, experiments with Ferucarbotran using this chemistry showed a substantial amount of precipitation indicating that the carbodiimide conjugation destabilised the nanoparticle itself. This result suggested that some of the carboxydextran chains of Ferucarbotran were attached to the iron oxide core; the EDC/NHS chemistry activates these carboxylic groups and therefore destabilizes the nanoparticle.

Consequently, a different conjugation chemistry utilizing hydroxyl groups within the dextran chains was examined: cyanogen bromide conjugation (Hermanson 2008). A nucleophilic elimination attack of the hydroxyl group on the cyanogen bromide results in cyanate ester and bromide. This is followed by a nucleophilic addition of the amine to electron deficient cyanide group resulting in an isourea linkage (Kozissnik 2012).
Using this chemistry to functionalise Ferucarbotran with shMFEm and shNFEm resulted a stable particle suspension, where only little precipitation was observed.

In order to enable characterization of the FX-shMFEm conjugates, the particles had to be separated from the unbound scFv antibody fragment and so different purification techniques were investigated. Ferucarbotran cannot be washed magnetically or by centrifugation requiring a different approach. In the literature, the most commonly presented method to purify particles is dialysis (Xie, Gu et al. 2005; Chandran, Chaudhary et al. 2006; Nash, Lai et al. 2010; Thomassen, Aerts et al. 2010), where particles are separated by diffusion. It is a time consuming and expensive method and does not provide elimination of the unwanted substances, as it is merely a dilution.

Another method described in the literature was size exclusion chromatography (SEC) (Tiefenauer, Kuhne et al. 1993; Kresse, Wagner et al. 1998; Lutz, Stiller et al. 2006). To establish a suitable purification protocol for the FX-shMFEm and FX-shNFEm, conjugates different matrix and column lengths were investigated. A first experiment by applying unconjugated Ferucarbotran on a HiPrep™ column filled with Sephacryl™ S-300 high resolution matrix failed as the particles were irreversibly trapped within the column.

Since, during conjugation, change of particles buffers was required, it was observed that Ferucarbotran easily travelled through a PD-10 desalting column filled with Sephadex™ G-25. So a Sephadex™ matrix was the next to be examined. Due to the size of shMFEm and shNFEm with 27 kDa, Sephadex™ G-100 was chosen instead of Sephadex™ G-25, with a fractionation range for globular proteins between

4 – 150 kDa. Next different column lengths were evaluated and the optimal setup for Ferucarbotran was found in XK 16/100 column filled with Sephadex™ G-100.

In order to confirm that SEC was suitable to separate the FX-shMFEm and FX-shNFEm from the unbound scFv antibody fragments, a Western blot was performed. However, the SDS-PAGE, under standard reducing conditions followed by a Western blot with an anti-His antibody, showed clear bands in purified and unpurified samples indicating the presence of unbound scFv, suggesting that purification had failed. Thorough dissection of the procedure leading to the respective Western blot found that since the samples had been boiled for 4 min at 90 °C under reducing conditions, this could have destroyed the link between particle coating and scFv. Therefore, a native PAGE gel was cast and samples from the same conjugation were run without boiling and under non-reducing conditions followed a by a slightly more sensitive ECL western blot. The results confirmed successful purification through SEC enabling characterization of the FX-shMFEm and FX-shNFEm conjugates.

In 2009, Vigor *et al.* (Vigor, Kyrtatos et al. 2009) proposed the use of an ELISA to confirm the presence and immunoreactivity of antibodies on nanoparticles. The wells are coated with the antigen, particles are added and the antibodies detected with specific antibodies. In their experiment they used PEG and dextran coated nanoparticles, which have a neutral surface charge.

However, a first experiment with Ferucarbotran showed high non-specific interaction of the particle with the polystyrene 96-well plate. Therefore Vigor's method was slightly modified and the nanoparticles directly immobilized onto a 96-well MaxiSorp™ plate. It is important to point out that MaxiSorp™, according to the manufacturer's homepage (Nunc), is a modified polystyrene surface with high affinity to polar groups and therefore proteins. Hence, nanoparticles with functionalised with antibodies or antibody fragments were "sticking" better to the plate and therefore yield a more intense signal, then the unconjugated particles.

Using this technique, it was confirmed that antibodies were bound to the surface of the nanoparticle, however, since there was no interaction with the antigen, no conclusion about the immunoreactivity of the FX-scFv conjugates could be drawn.

When characterising antibodies, binding kinetics (Malmborg, Michaelsson et al. 1992) are an important part and often determined through surface plasmon resonance (SPR) (Boozer, Kim et al. 2006) or quartz crystal microbalance (QCM) (Guilbault and O'Sullivan 1999). SPR is a purely optical technique. Polarized light is shone through a prism onto a sensor surface with a gold film on which the sample ligand is immobilized. An optical detection unit senses the reflected light. When an analyte interacts with the immobilized ligand, there is a change of mass causing a change in the refraction or resonance (angle) and therefore in the recorded signal. (Jonsson, Fagerstam et al. 1991; Myszka 1997; Myszka 2000)

QCM is based on the piezoelectric effect. An electric charge is applied to a quartz crystal inducing mechanical stress and causing it to oscillate at a specific frequency. A change of mass on the crystal's surface initiates a change in frequency. This non-optical technique enables the investigation of thicker layers like nanoparticles or even cells. (Guilbault and O'Sullivan 1999; Cooper and Singleton 2007)

In the first set of QCM experiments, the scFv, shMFEm and shNFEm, were directly immobilized onto two sensor chips and subjected to different concentrations of NA1. The interaction profiles showed a clear interaction between shMFEm and NA1, while on the control channel with shNFEm almost no interaction was detected.

Next the conjugates were directly immobilized onto two sensor chips and treated with the same concentrations of NA1 as the pure scFv, enabling the first visualisation of the interaction between a SPION-scFv conjugate and cognate antigen in real-time.
Quartz crystal microbalance has been combined with nanoparticles in the past, however the nanoparticles were mainly used as signal enhancers to amplify the signal and therefore improve the sensitivity of this technique. (Lin, Zhao et al. 2000; Mao, Yang et al. 2006; Kim, Baek et al. 2007)

The interaction profiles gained from the FX-scFv conjugates showed a significantly weaker interaction between the shMFEm functionalized conjugates and the NA1. Additionally, the binding kinetics revealed a slightly slower association rate, in comparison with the pure shMFEm results and an almost twice as fast dissociation rate. An explanation for this phenomenon can be found in the different paths of the NA1 in both cases. While the pure scFv immobilized on the chip provide a planar surface with multiple interaction points for the cognate antigen, the conjugates with their spherical shape and dextran coat offer a much more difficult geometry for the

NA1 to interact with the attached shMFEm. Some scFv molecules might only be partially accessible due to the particle shape, but also due to physical hindrance, caused by the flexible dextran matrix (Livney, Ramon et al. 2001) shifting and partially covering the rather small scFv.

A solution to this issue could be the use of iron oxide nanoparticles with a more stealth coating such as polystyrene or PEG or site-specific attachment of the targeting moiety (Kozissnik 2012). Whereas conventional conjugation techniques, such as carbodiimide chemistry, establish covalent bonds randomly between any available carboxyl and amine group, site-specific attachment uses a unique target, such as a tag, in a specific location within the target molecule to create a single connection. The advantage site-specific attachment, over the random attachment, is that the orientation of the conjugated antibody or targeting moiety is known ensuring its functionality. Therefore, site-specific attachment was also investigated as an option to functionalize Ferucarbotran with shMFEm. To realise this specific conjugation method, two chemistries were combined: Sodium periodate conjugation and maleimide chemistry.

Using sodium periodate, the maleimide linker BMPH was attached to the Ferucarbotran, utilizing the primary hydroxyl groups within the dextran and the one amine group within the linker. In a second step, the maleimide was activated and reacted to the cysteine tag of shMFEm-Cys. SEC purified the resulting FX-shMFEm-Cys conjugate and ELISA confirmed the presence of shMFEm-Cys.

Even though the attachment and purification were proven successful, the ELISA revealed a less efficient overall conjugation. Since for Ferucarbotran this required a two-step conjugation, substantially more particles were lost through the buffer exchanges and handling. Additionally, as a chemical reaction is never 100% efficient, there was a considerably lower amount of linker attached to nanoparticles and consequently much less scFv. Therefore, cyanogen bromide conjugation was put forward to functionalize Ferucarbotran with shMFEm and shNFEm for targeted hyperthermia *in vivo*.

4.5 Summary

The aim of this chapter was to establish a conjugation method to attach scFv antibody fragments to Ferucarbotran and characterize the resulting conjugates.

After showing that carbodiimide chemistry destabilized the particles, cyanogen bromide conjugation proved to be a suitable method to functionalise Ferucarbotran.

FX-scFv conjugates were purified by size exclusion chromatography and their immunoreactivity analysed by quartz crystal microbalance. QCM provided closer evaluation of the binding affinity of the attached scFv confirming the targeting potential of FX-scFv.

Chapter 5

Antibody Targeted Magnetic Nanoparticle Hyperthermia *in vivo*

5.1 Introduction

The work in the previous chapters demonstrated the superior *in vitro* heating potential of Ferucarbotran and established that it can be successfully functionalised with scFv antibody fragments to enable targeting. The aim of this chapter was to investigate whether these findings could be applied *in vivo*.

When *in vitro* results are taken to *in vivo* application, a number of fresh variables are introduced. Since tumours are heterogeneous tissues often containing areas of necrosis and/or hypoxia, particle distribution within the tumour and possible cooling through blood vessels affect the treatment potential of the nanoparticles applied.

Therefore the first experiment was set up to determine Ferucarbotran's (FX) heating potential *in vivo*. A high and low concentration of FX was injected into SW1222, human colorectal carcinoma cell line, xenografts subjected to an AMF. During the experiment the tumour and body temperature were monitored. Post-mortem particle distribution within the tumour and apoptosis were assessed.

This experiment highlighted the importance of tumour architecture and the need to find a method to keep the nanoparticles within the tumour. So, in a second experiment particle retention and distribution in different tumour types were investigated before, in a third experiment, non-targeted nanoparticle conjugates (FX-shNFEm) were compared with targeted nanoparticle conjugates (FX-shMFEm).

5.2 Objectives

The objectives of the research described in this chapter were to:

1. Determine heating potential of Ferucarbotran *in vivo*

2. Investigate nanoparticle distribution within *in vivo* xenograft models of human tumours

5.3 Results

5.3.1 Non-Targeted Magnetic Nanoparticle Hyperthermia *in vivo*

Ferucarbotran demonstrated a superior heating potential *in vitro.* Thus, the purpose of this experiment was to understand how the *in vitro* heating potential of Ferucarbotran and the second best heating particle fM-DX 100 translates *in vivo* on a macroscopic level. Other parameters, like particle distribution within the tumour as well induction of apoptosis, were also investigated.

MF1 nude mice were induced with SW1222 xenografts and separated into two groups of three, one treated with FX and the other one with fM-DX 100. In each group, two mice were injected with a 'high dose' of nanoparticles (2 mg Fe per tumour) injected iT, but only one was treated with the AMF for 20 min. The third mouse received iT a 'low dose' of nanoparticles (0.5 mg Fe per tumour) and was also subjected to the AMF. Additionally, a control mouse was grown, injected with saline only, but was not treated with AMF.

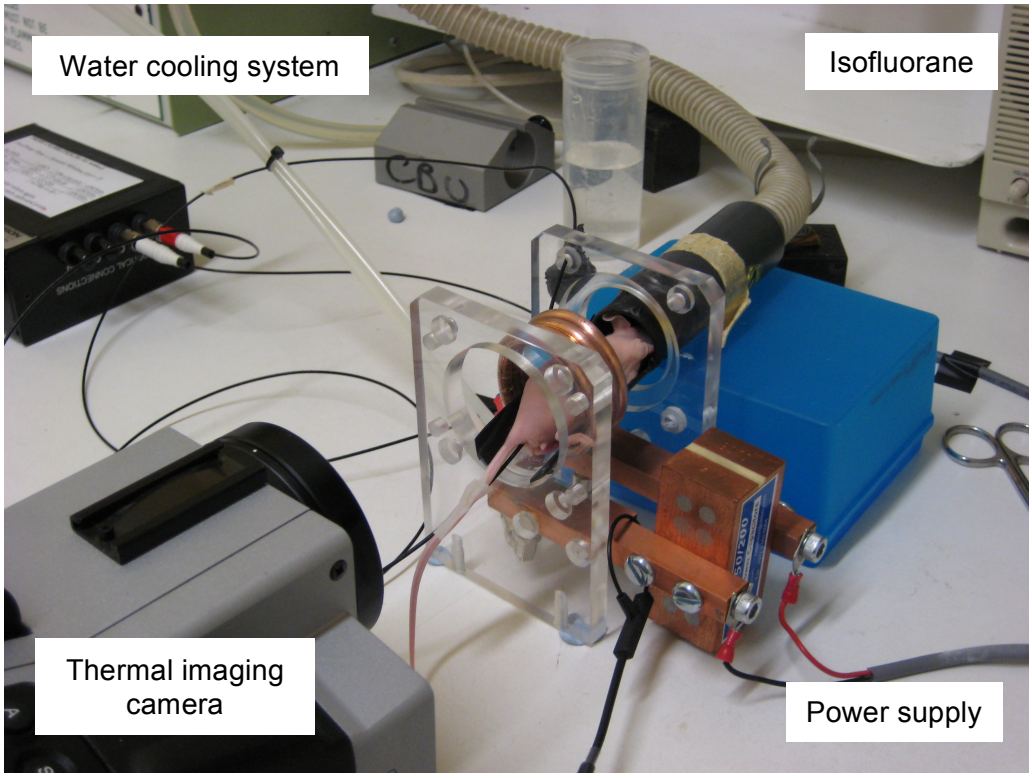

Fig. 5.1 Experimental set-up for non-targeted magnetic nanoparticle hyperthermia *in vivo* consisting of the MACH system (not in the picture) with an external copper coil, a water cooling system, isofluorane as anesthetic and a thermal imaging camera.

The mice were anaesthetised during the procedure and a thermal imaging camera monitored the temperature changes in the tumour. The camera faced the backside of the mouse surrounded by the copper coil of the MACH system as shown in Fig. 5.1.

5.3.1.1 Thermal Imaging

The thermal imaging pictures in Fig. 5.2 taken from the mice injected with FX, confirm an immediate temperature increase in the tumour in the presence of the alternating magnetic field (AMF), in the tumour treated with the high dose and in the tumour treated with the low dose.

After 20 min, the temperature in the tumour treated with 2 mg FX was 7.2 °C above the average body surface temperature of the mouse. In the tumour injected with the low dose of 0.5 mg FX, the temperature showed a 5.8 °C increase.

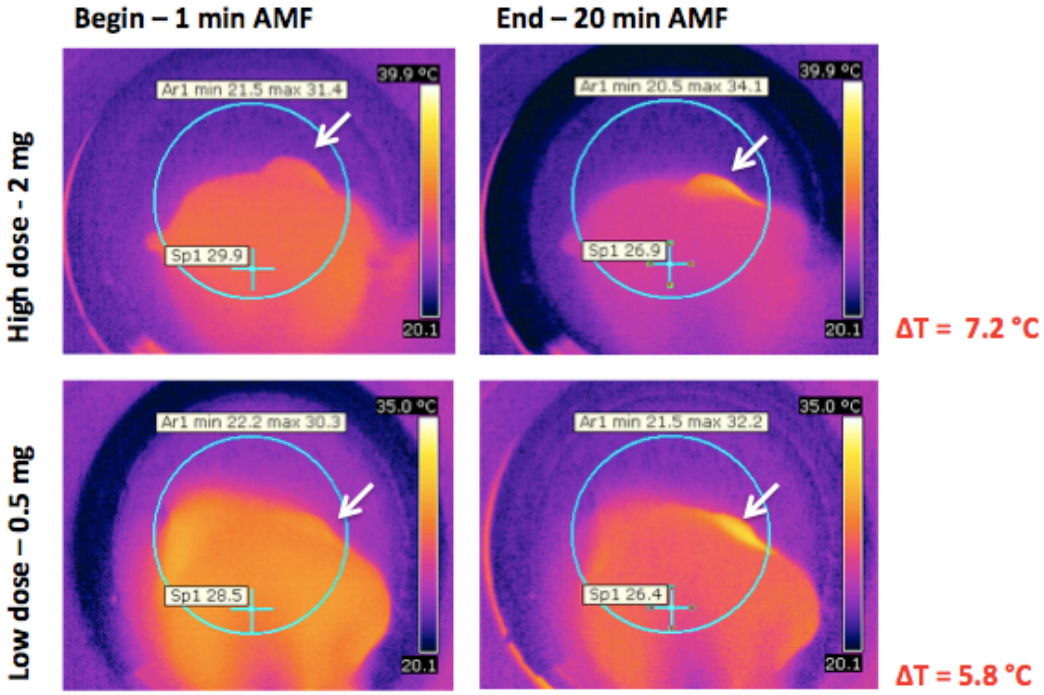

Fig. 5.2 Thermal imaging pictures of two SW1222 xenografts injected with FX inside the MACH system after 1 min and 20 min treatment with AMF. The tumour (indicated by the arrow) received 2 mg FX iT and showed a surface temperature increase of 7.2 °C after 20 min, while the second tumour (presented in the bottom row) received 0.5 mg FX iT displayed a surface temperature increase of 5.8 °C.

In addition, to the thermal imaging pictures taken of both mice treated with FX combined with the AMF, a temperature probe was inserted into the rectum in order to monitor the body temperature.

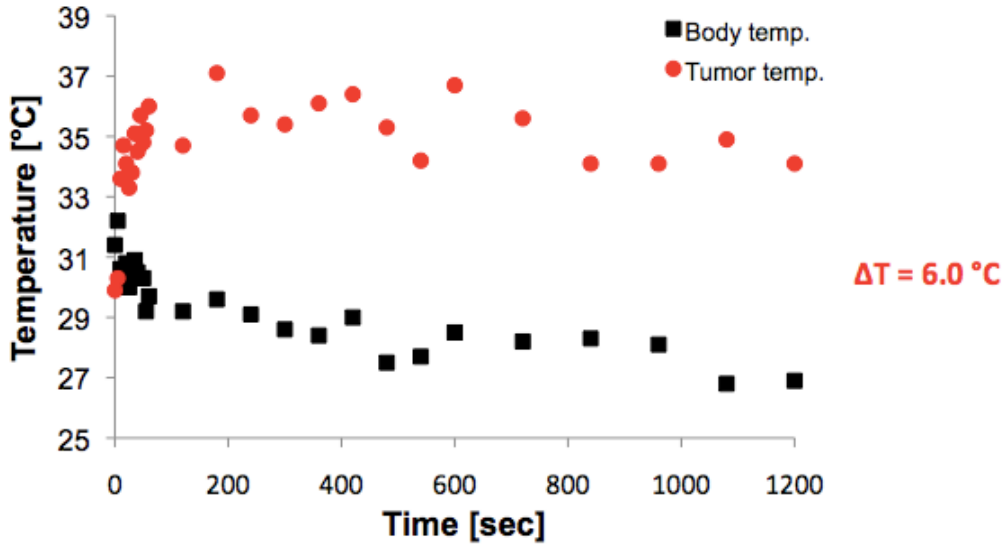

Fig. 5.3 Progression of tumour and body temperature during the treatment inside the MACH system of a mouse injected with 2 mg FX and subjected to AMF. ΔT represents the temperature difference between the averaged body temperature and the averaged tumour temperature.

The temperature changes in Fig. 5.3, showed body and tumour temperatures of the 2 mg FX mouse, indicating a sharp temperature increase in the tumour area during the first minute followed by a slight decrease over the duration of the treatment. Interestingly, tumour and body temperature decreased at the same rate.

In contrast, the temperature measurements of 0.5 mg FX mouse (Fig. 5.4) revealed, after an initial temperature increase within the first minute, an overall rise of the temperature in the tumour area as well as the body surface till the end of the treatment.

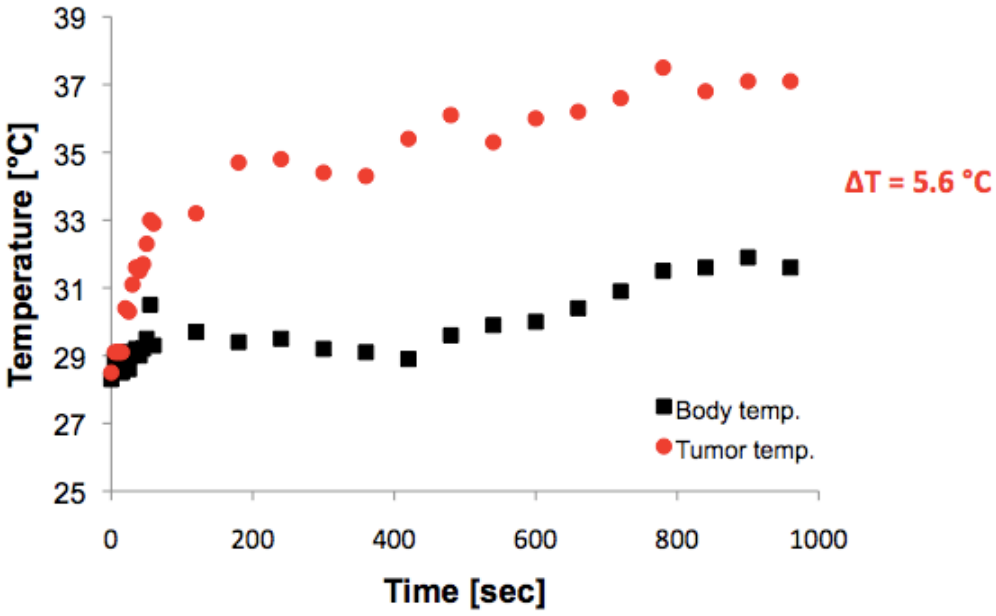

Fig. 5.4 Progression of tumour and body temperature during the treatment inside the MACH system of a mouse injected with 0.5 mg Ferucarbotran and subjected to AMF. ΔT represents the temperature difference between the averaged body temperature and the averaged tumour temperature.

The thermal imaging pictures from the mice treated with fM-DX 100 in Fig. 5.5 showed a temperature increase of 4.7 °C in the mouse treated with the high dose and 1.4 °C with the low dose in the tumour area.

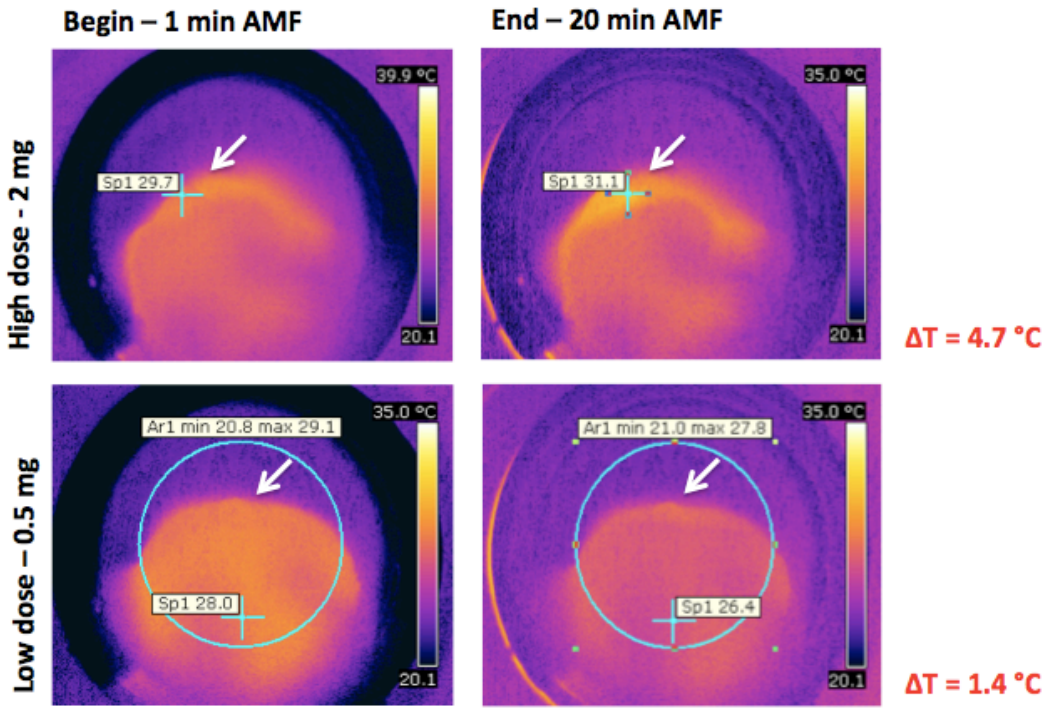

Fig. 5.5 Thermal imaging pictures of two SW1222 xenografts injected with fM-DX 100 inside the MACH system after 1 min and 20 min treatment with AMF. The tumour (indicated by the arrow in the top row) received 2 mg fM-DX 100 iT and showed a surface temperature increase of
4.7 °C after 20 min, while the second tumour (presented in the bottom row) received 0.5 mg fM-DX 100 iT displayed a surface temperature increase of 1.4 °C.

Independently of the temperature changes in the tumour regions observed in all mice treated, the body temperature dropped after anaesthesia and further during treatment indicating the need for a heating supply for consequent hyperthermia experiments (eg. through cooling the copper coil of the MACH system to 37 °C instead of 20 °C used in this experiment.)

5.3.1.2 Histology

After the magnetic nanoparticle hyperthermia the tumours were excised, processed, and cut for further analysis. The tissue sections where then stained with Prussian blue to localise the particles in the tumour and cleaved caspase 3 to visualise apoptosis.

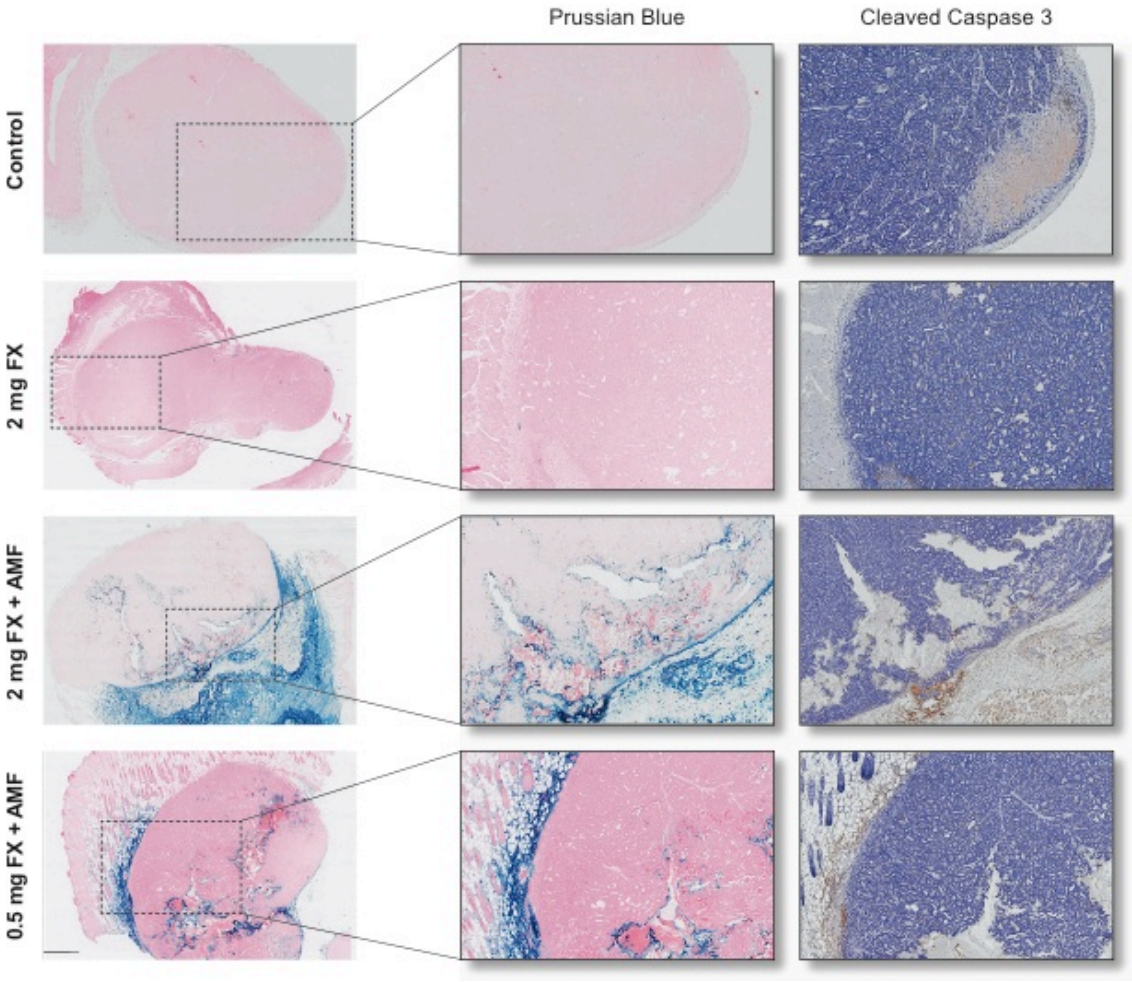

Fig. 5.6 Histology results of tumours treated with Ferucarbotran (FX) with and without the presence of the AMF. The tumours were stained with Prussian Blue to reveal the location of the particles (blue), as well as immunohistochemistry with a cleaved caspase 3 antibody to visualise apoptosis (brown) in the control tumour. In the particle treated tumours apoptosis could not be distinguished from the nanoparticles, due to their brown colour, when unstained.

In the Ferucarbotran treated tumours, shown in Fig. 5.6, no particles were found in tumours that had received no AMF treatment. In the tumours subjected to the AMF, particles were mainly located in the stroma surrounding the tumour, rather than the center of the tumour. This suggested that the temperature increase observed through

thermal imaging was indeed a reflection of the heating achieved by the Ferucarbotran.

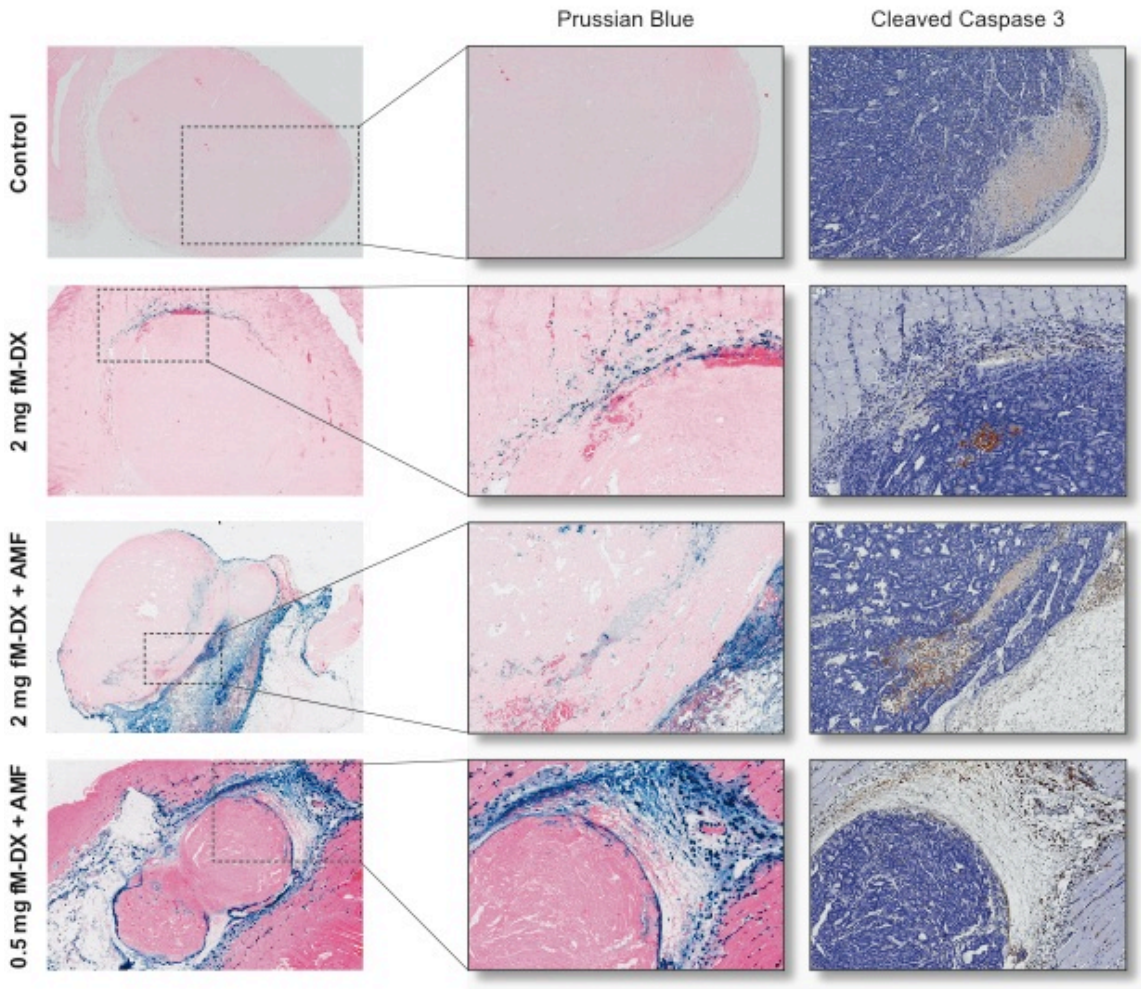

Fig. 5.7 Histology results of tumours treated with fM-DX 100 with and without the presence of the AMF. The tumours were stained with Prussian Blue to reveal the location of the particles (blue), as well as immunohistochemistry with a cleaved caspase 3 antibody to visualise apoptosis (brown) in the control tumour. In the particle treated tumours apoptosis could not be distinguished from the nanoparticles, due to their brown colour, when unstained.

Similarily to the tumours injected with Ferucarbotran, in the tumours treated with fM-DX 100, the majority of particles were found in the tumours subjected to the AMF (seen in Fig. 5.7). While no particles could be located within the tumour centers, the majority was found in the tissue surrounding the tumours. This suggested that, immediately after injection, the particles, forced by the interstitial pressure, followed the needle out of the tumour.

Unfortunately, the cleaved caspase 3 staining only indicated apoptosis in the control tumour, as in the particle treated tumours, due to the brown colour of the unstained particles, no distinction between apoptosis and nanoparticles could be made.

5.3.2 Identifying a Suitable Tumour Model for Magnetic Nanoparticle Hyperthermia *in vivo*

In the previous experiment, SW1222 xenografts were chosen for their homogenous tumour growth without or with small areas of apoptosis in order to observe possible apoptosis caused by the heating particles. However, the results unfortunately suggested a 'leak' of the particles into the tissue surrounding the tumour, possibly due to high interstitial pressure. Hence, a suitable model and technique had to be found to keep the nanoparticles within the tumour.

Therefore, in this experiment six MF1 nude mice were induced with three different tumour cell lines: SW1222, human colorectal carcinoma; Capan-1, human pancreatic adenocarcinoma and LS174T, human colorectal adenocarcinoma. Consequently, the tumours were injected using the technique previously described by Giustini *et al.* (Giustini, Ivkov et al. 2011). The nanoparticle suspension was injected iT under anaesthesia over the course of 30 sec, keeping the needle in place for another 5 min in order to optimize particle distribution within the tumour.

Afterwards the mice were left to recover and sacrificed 25 min after withdrawal of the needle. The tumours were excised, processed, and stained with Prussian blue and haematoxylin and eosin (H&E) for further analysis.

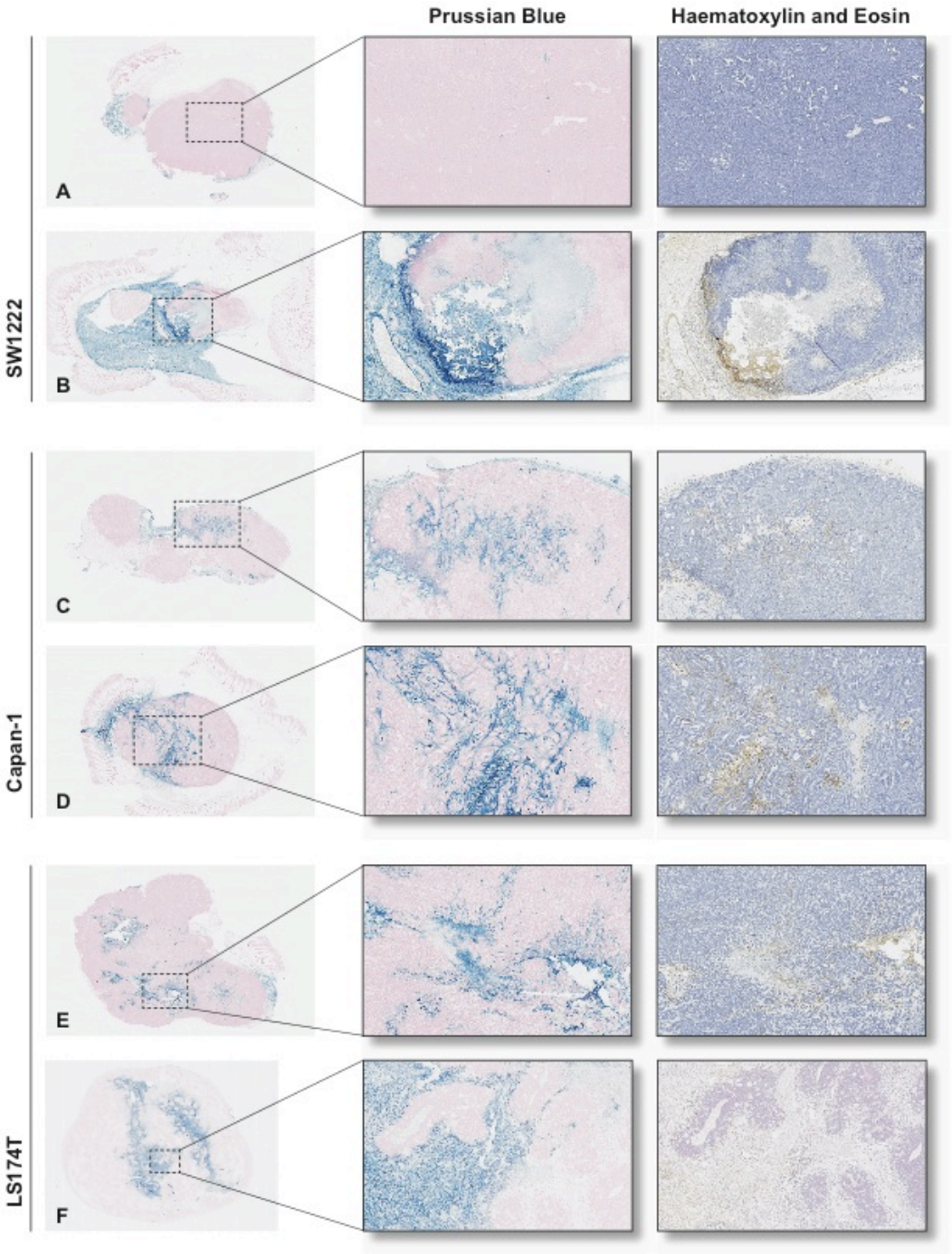

Fig. 5.8 Histology results of different xenograft tumours (SW1222 – A and B; Capan-1 – C and D; LS174T – E and F) injected with FX. The tumours were stained with Prussian blue to enable location of the nanoparticles (blue) and H&E visualise tumour architecture. Tumour sizes were different, however the magnification of the staining was kept constant at x2.5.

Histology (Fig. 5.8) revealed an almost even distribution of particles within Capan-1 and LS174T xenografts, however no improvement was observed within the SW1222 tumours compared to the first *in vivo* experiment (*see section:* 5.3.1). Encouragingly, as H&E, revealed the tumour architecture, indicated, particles penetrated deeper into

the tumour and substantially more Ferucarbotran was found within the tumour, rather than its surrounding stroma.

To investigate the particle distribution throughout the tumour in more detail, the second LS174T xenograft (see F in Fig. 5.8) was completely sectioned as shown in Fig. 5.9.

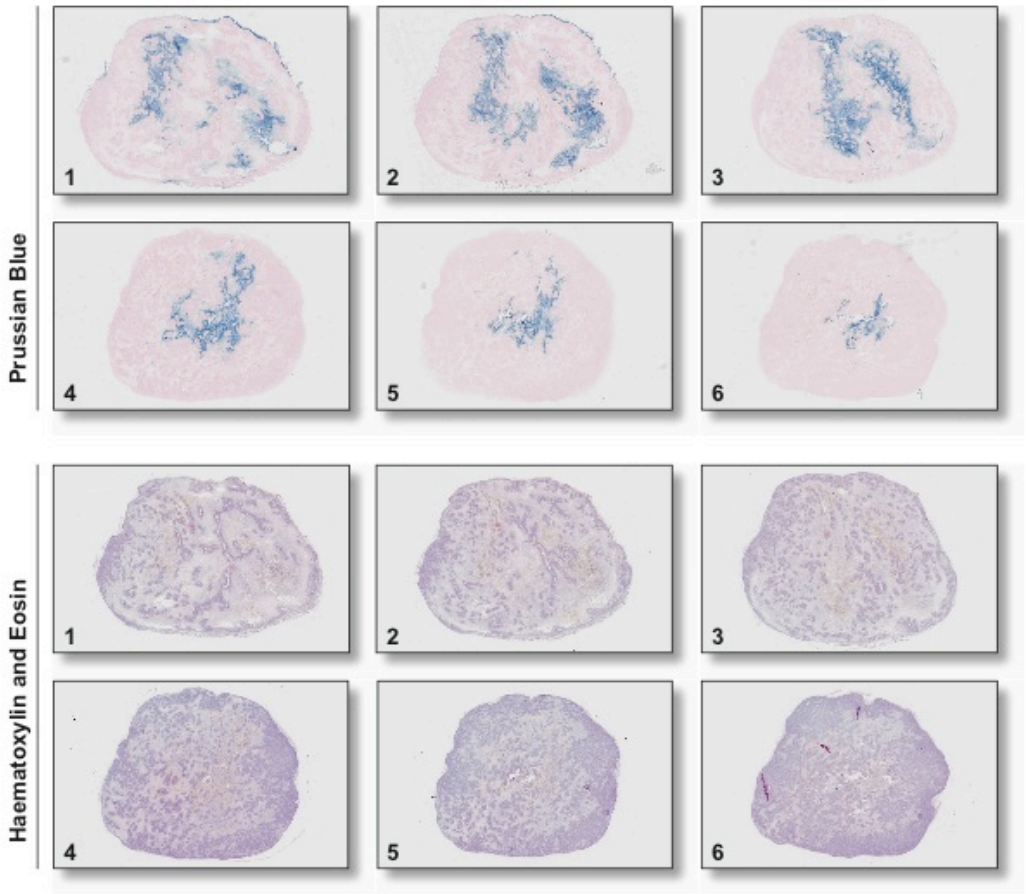

Fig. 5.9 Histology results of a fully sliced LS174T xenograft. The tumours were stained with Prussian blue to enable location of the nanoparticles (blue) and H&E to visualise tumour architecture.

Within the slices 1-3 of the second LS174T xenograft (Fig. 5.9), the particles seemed to penetrate major areas of the tumour, however, the consecutive slices 4-6, showed that the particle distribution in the lower half of the tumour was less optimal. Nevertheless, the LS174T xenograft appeared to be the most promising tumour model for a targeted nanoparticle injection approach.

5.3.3 Intra-tumoural Distribution of Antibody Targeted Magnetic Nanoparticle Hyperthermia

For this experiment FX nanoparticles were conjugated with either shMFEm or shNFEm through cyanogen bromide conjugation, purified and characterised as described in Chapter 4. Consequently, LS174T xenografts were raised in six MF1 nude mice. The mice were divided into two groups of three and under anaesthesia injected with either FX-shMFEm or FX-shNFEm using the technique described in 5.3.2. Subsequently, two mice of each group were left to recover for 55 min before they were sacrificed and tumours excised. One mouse of each group was subjected to the AMF for 25 min. During the hyperthermia, the thermal imaging camera monitored treatment the surface temperature of the mouse. Afterwards, the mouse was left to recover for 30 min, sacrificed and the tumour excised. The tumours were processed, put into paraffin and stained with Prussian blue and H&E for further analysis.

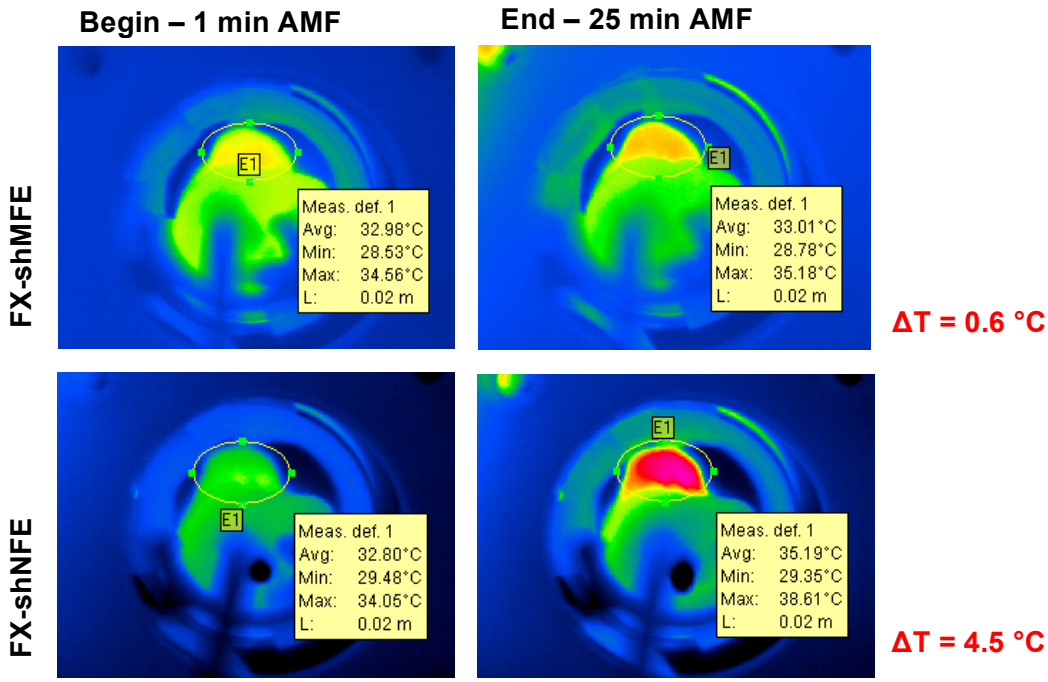

Fig. 5.10 Thermal imaging pictures of tumours injected with FX-shMFEm and FX-shNFEm inside the MACH system after 1 min and 25 min treatment with AMF. The tumour shown within the yellow elipse received FX-shMFEm (3 mg Fe/cm^3 tumour) iT and showed a surface temperature increase of 0.6 °C after 25 min, while the second tumour (presented in the bottom row) received equivalent amount of FX-shNFEm iT displayed a surface temperature increase of 4.5 °C.

Thermal imaging results showed a minor increase (less than 1 °C) in surface temperature of the tumour treated with FX-shMFEm as shown in Fig. 5.10, but a

considerable temperature increase (more than 4 °C) in the non-targeted control tumour treated with FX-shNFEm.

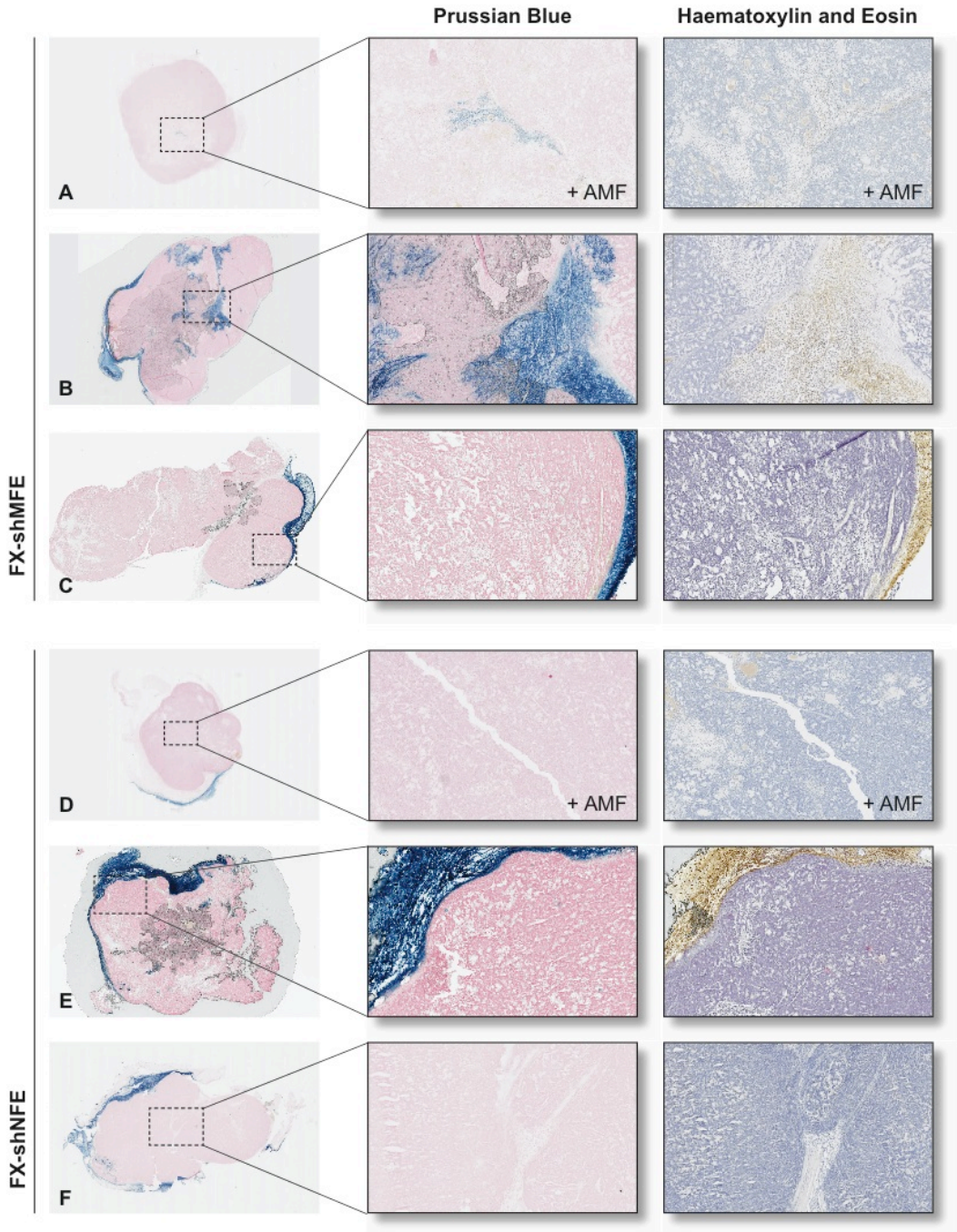

Fig. 5.11 Histology results of different tumours injected with FX-shMFEm and FX-shNFEm conjugates. Tumours A and D were subjected to the AMF for 25 min, while tumours B, C, E and F received no treatment. The tumours were stained with Prussian blue to enable location of the nanoparticles (blue) and H&E to visualise tumour architecture. Tumour sizes were different, however the magnification of the staining was kept constant at x2.5.

Histological analysis of the tumours (Fig. 5.11) treated with the AMF revealed that only a small amount of FX-shMFEm conjugates had stayed in the tumour, while no FX-shNFEm conjugates were found within the tumour only in the surrounding tissue. The control tumours, which were not subjected to the AMF showed a similar picture.

Interestingly, even though in both cases, tumours were treated with targeted and non-targeted nanoparticle conjugates, most particles were found in the periphery of the tumours, it seemed as if more FX-shMFEm conjugates stayed within the tumour tissue than its FX-shNFEm counterpart.

5.4 Discussion

The work presented in this chapter examined the heating potential of Ferucarbotran *in vivo*. It also investigated the localisation of nanoparticles within the tumour and further examined the effects of targeting on the intratumoural distribution of Ferucarbotran.

Ferucarbotran demonstrated a superior heating potential *in vitro*. So the first experiment evaluated how this potential translates *in vivo.* Using a 'high dose' (2 mg Fe per tumour) or a 'low dose' (0.5 mg Fe per tumour), nanoparticles were injected iT into SW1222 xenograft model subjected to an alternating magnetic field (AMF) for 20 min. Afterwards, the tumours were excised, processed, and cut for further analysis.

Thermal imaging results of the surface of the tumour treated with 2 mg Ferucarbotran showed a temperature increase in the tumour area of 7.2 °C. Interestingly, thermal imaging of another tumour treated with 0.5 mg Ferucarbotran still demonstrated a difference between start and end temperature of 5.8 °C. Staining with Prussian blue of the excised tumours provided a possible explanation. While most of the particles of the 'low dose' stayed within the tumour and its rim, the majority of particles in the tumour treated with the 'high dose' leaked into the surrounding tissue. Remarkably, Prussian blue staining also revealed that almost no particles stayed in the tumours injected with nanoparticles not treated with the AMF. Johannsen *et al.* acquired similar results, when they examined the feasibility of magnetic fluid hyperthermia treatment of prostate cancer (Johannsen, Jordan et al. 2004).

Since in the first experiment it looked like the particles left the tumour with the removal of the needle after iT injection, a new injection technique, as well as different

tumour cell lines was evaluated. Therefore three different CEA expressing xenograft tumour types were raised. Additionally to the SW1222, human colorectal carcinoma; Capan-1, human pancreatic adenocarcinoma and LS174T, human colorectal adenocarcinoma were induced. The nanoparticle suspension was injected iT over the course of 30 sec, while keeping the needle in place for a total of 5 min in order to optimize particle distribution within the tumour, as described by Giustini *et al.* (Giustini, Ivkov et al. 2011)

Histology of the excised tumours showed again a leakage of particles into the surrounding tissue in the SW1222 xenograft. In Capan-1 and LS174T tumours particles were mainly found in the tumour centres. To gain a better understanding of the particle distribution, the second LS174T tumour was sliced up completely, revealing that the nanoparticles were able to penetrate most of the tumour. Based on these results it was decided to move forward using Giustini's injection technique and LS174T xenografts. So, for the next experiment LS174T xenografts were raised in six MF1 nude mice. The mice were divided into two groups of three and injected with either FX-shMFEm or FX-shNFEm. Subsequently, one mouse of each group was subjected to the AMF for 25 min.

During the hyperthermia treatment, the thermal imaging camera monitored the surface temperature of the mouse. Afterwards, the mouse was left to recover for 30 min, sacrificed and the tumour excised. The tumours were processed, put into paraffin, and stained with Prussian blue and H&E for further analysis.

Thermal imaging results showed a minor increase (less than 1 °C) in surface temperature of the tumour treated with FX-shMFEm, but a considerable temperature increase (more than 4 °C) in the non-targeted control tumour treated with FX-shNFEm. However, pathology revealed in both cases, tumours treated with targeted and non-targeted nanoparticle conjugates, most particles were found in the periphery of the tumours; it seemed as if more FX-shMFEm conjugates stayed within the tumour tissue than its FX-shNFEm counter parts.

5.5 Summary

The aim of the work in this chapter was to examine the *in vitro* heating potential of Ferucarbotran in a xenograft tumour model. Even though this Ferucarbotran's hyperthermia potential was confirmed, histology showed that the majority of the particle did not stay within the tumour and migrated to the stroma surrounding the tumour. So, consequently, different tumour models and a new injection method were tested. A LS174T xenograft was deemed suitable, injected with FX-shMFEm and FX-shNFEm, antibody nanoparticle conjugates and subjected to AMF.

The results supported the hypothesis of a therapeutic potential for targeted magnetic nanoparticle hyperthermia, but also indicate challenges that have to be addressed to enable clinical application of this treatment modality.

Chapter 6

Discussion and Conclusion

The work in this thesis strategically investigated the hypothesis that targeted superparamagnetic iron oxide nanoparticles (SPION) subjected to an alternating magnetic field have the potential to induce localised hyperthermia in cancer therapy.

To test this hypothesis, an array of commercially available iron oxide nanoparticles were thoroughly characterised and examined for their hyperthermia potential. The best candidate, Ferucarbotran, was then functionalised with scFv antibody fragments specifically targeting carcinoembryonic antigen (CEA). Appropriate conjugation and purification techniques were applied, evaluated and optimised; with QCM, a novel way of characterizing FX-scFv conjugates was explored yielding important information about their functionality. The superior *in vitro* heating capability of Ferucarbotran was tested and confirmed *in vivo*, before the therapeutic potential of non-targeted and targeted SPION was examined. The results supported the hypothesis of a therapeutic potential for targeted magnetic nanoparticle hyperthermia, but also highlighted challenges, which need to be addressed in order to reach its full clinical potential.

My work has highlighted the need for characterisation, in the field of biomedical applications of nanoparticles, as deviations from the manufacturer's specifications occur. It is essential to know the properties the nanoparticles possess that we use, not only for our research, but also for the comparability of results within the research community.

A difference in the hydrodynamic diameter (*see section:* 1.1.1) might change the nanoparticles' route of clearance and therefore its blood half life. For hyperthermia application the consequences might be even more severe, as the combination of hydrodynamic diameter and dispersity, core diameter and composition of the nanoparticle suspension will define its heating potential (Krishnan 2010; Ortega 2012).

Furthermore, in the literature particles are often described as 'stable in water', but as long as their stability is not shown under physiological conditions, it's impossible to draw valid conclusions. Moreover, it has been shown that aggregation negatively impacts the heating potential of nanoparticles (Dutz, Clement et al. 2009).

After thorough property analysis, Ferucarbotran was found to be the most suitable magnetic nanoparticle for a potential therapeutic hyperthermia application, due to its

superior heating capability. Consequently, Ferucarbotran, also known as unformulated MRI contrast agent Resovist®, was functionalised with the anti-CEA scFv antibody fragment shMFEm, and it's non-binding variant shNFEm, via cyanogen bromide conjugation (*see section:* 4.3.1.4). However, by adapting quartz crystal microbalance for the characterization of the FX-shMFEm conjugate, it enabled the first time real time visualisation of the interaction between the conjugate and its cognate antigen (*see section:* 4.3.3.2), delivering important information on the potential behaviour of the magnetic nanoparticle conjugate *in vivo*.

The resulting binding kinectics indicated a slightly slower association rate and an almost twice as fast dissociation rate in comparison to results of the pure shMFEm. These results suggested that some of the scFv molecules might only be partially accessible due to particle shape, but also physical hindrance due to the flexible dextran matrix potentially covering the shMFEm. This motivated not only a look into more stealth coatings, such as polystyrene or PEG, but also site-specific attachment (*see section:* 4.3.4.2), where conjugation is facilitated through a specific target residue (eg. cysteine) to create a single connection, an interesting technique ensuring the functionality of the attached targeting moiety.

The *in vivo* translation of the superior *in vitro* heating potential of unconjugated Ferucarbotran showed a substaintial temperature increase in the tumour area during treatment; however, the histological analysis revealed that even though the particles were directly injected into the tumour, most nanoparticles leaked into the surrounding tissue (*see section:* 5.3.1). This highlighted one of the biggest challenges in magnetic nanoparticle hyperthermia: delivery.

Therefore, in a second experiment, different tumour types, as well as a new injection method were tested (*see section:* 5.3.2). By injecting the nanoparticle suspension iT over the course of 30 sec, while keeping the needle in place for a total of 5 min, as described by Giustini *et al.* (Giustini, Ivkov et al. 2011), the particle distribution was optimised, enabling direct comparison of the therapeutic potential of targeted FX-shMFEm and the non-targeted control FX-shNFEm (see section: 5.3.3).

While only a minor temperature (less than 1 °C) increase was observed in the tumour treated with FX-shMFEm, a considerable temperature increase (more than 4 °C) was observed in the tumour treated with the FX-shNFEm conjugates. Pathology revealed that even though most particles were found in the surrounding tissue, more FX-

shMFEm conjugates stayed within the tumour tissue than its FX-shNFEm counter parts supporting the hypothesis of a therapeutical potential for targeted magnetic nanoparticle hyperthermia.

However, in order for magnetic nanoparticle hyperthermia to reach its full clinical potential, a number of challenges, besides the need for targeting, have to be addressed, such as the missing consensus within the field on what magnetic fields can be applied to the human body.

While a number of research groups (Andra, d'Ambly et al. 1999) are still using magnetic field strengths up to 10 kA/m (Brezovich 1988) others apply fields up to 90 kA/m, (Bordelon, Cornejo et al. 2011) which might induce eddy currents in the tissue and are therefore not safe for *in vivo* application (Hergt, Dutz et al. 2006; Hergt and Dutz 2007).

There is also a critical need to understand the biological effects of magnetic nanoparticle hyperthermia. How are magnetic particles affecting the targeted cells? How can the synergy between chemo and/or radiation therapy with hyperthermia be improved through the application of magnetic nanoparticles? Does hyperthermia really activate the immune system to induce anti-tumour immogenicity, as suggested by Ito *et al*. (Ito, Shinkai et al. 2001; Ito, Shinkai et al. 2003; Torigoe, Tamura et al. 2009)?

The beauty of using magnetic nanoparticles is that we can design and engineer them to meet the requirements of a clinical application. Especially, in hyperthermia, to have the ability to use a magnetic field, instead of infrared light or radiation (Cherukuri, Glazer et al. 2010), to achieve an increase in temperature, is a major advantage as the human body is almost transparent without limitation of maximum penetration depths.

In conclusion I have established important parameters for magnetic nanoparticles *in vivo* and provided a novel approach enabling the better characterization of the binding kinetics of nanoparticle-antibody conjugates. This thesis will provide an important guide into bringing targeted magnetic nanoparticle hyperthermia closer to the clinic.

Chapter 7

Future Challenges

In order to take the work presented in this thesis forward, next particles with a more stealth coating, such as polyethylene glycol (PEG), should be evaluated for their therapeutic potential for a targeted hyperthermia approach. This should include an extensive property analysis of the magnetic nanoparticles, examining hydrodynamic diameter, zeta potential, core diameter, iron content, as well as magnetic properties and heating potentials.

In this regard, in addition to standard techniques, such as dynamic light scattering to determine the hydrodynamic diameter, other methods like nanoparticle tracking analysis (NTA) should also be explored. In contrast to DLS, where fluctuations of the intensity of the scattered light caused by a small number of particles in the path of a laser beam are measured, NTA tracks individual particles and determines their hydrodynamic size through their Brownian motion resulting not only in higher number of measurements, but also providing a more complete picture of the size distribution within a nanoparticle suspension.

Additionally, in order to assure the functionality of the scFv antibody fragments after attachment, one-step site-specific attachment techniques should be further explored and compared to the more commonly used random conjugation chemistries, such as carbodiimide chemistry, using quartz crystal microbalance.

Further work also includes the *in vivo* evaluation of the antibody targeted and non-targeted conjugates through direct intratumoural injection. However, the final goal will be systemic delivery of actively targeted magnetic nanoparticles for hyperthermia application.

On a wider scale, in order to advance the field of magnetic particle hyperthermia, the mechanisms of magnetic nanoparticle hyperthermia have to be better understood. It still remains a mystery whether magnetic nanoparticle hyperthermia is a local heating phenomenon, or a bulk-heating phenomenon. On the one hand, theoretical modelling by Rabin (Rabin 2002) implies that the energy dissipation by nanoscale heating should have a negligible effect, while experimental data by Huang et al. (Huang, Delikanli et al. 2010) indicates otherwise. Huang et al. specifically targeted magnetic nanoparticles to activate the temperature sensitive ion channel TRPV1 through the application of an alternating magnetic field. More interestingly, by using the temperature dependence of the fluorescence intensity of fluorophores attached to the nanoparticles and free in suspension, an immediate decrease in fluorescence of the

fluorophore on the particle was reported with the application of the alternating magnetic field. However, the intensity of the free fluorophore stayed constant, indicating local heating of the particles. If this local heating phenomenon in magnetic nanoparticles is confirmed, it would transform the field magnetic nanoparticle hyperthermia, enabling a more targeted therapy and expanding its range of applications.

Appendix I

Materials

Table 2.1: Solutions for dynamic light scattering and zeta potential measurement

Buffers	**Formula**
dH_2O	500 ml distilled water sterile filtered.
5 mM Sodium chloride	Dissolve 0.15 g sodium chloride in 500 ml dH_2O. Filter to sterilize.
PBS	Add 50 ml 10x PBS to 450 ml dH_2O

Table 2.2: Solutions for SPION-scFv carbodiimide conjugation

Buffers	**Formula**
0.1 M Sodium phosphate buffer pH 7.2	Dissolve 0.44 g monosodium phosphate and 1.83 g disodium phosphate in 90 ml dH_2O. Adjust pH and bring up to 100 ml by adding dH_2O. Filter to sterilize.
EDC/NHS Activation buffer	Add 2.5 mg EDC and 1.25 mg NHS to 200 µl 0.1 M sodium phosphate buffer. Use immediately.
50 mM Glycine	Dissolve 36 mg glycine in 10 ml 0.1 M sodium phosphate buffer pH 8.5. Filter to sterilize.

Table 2.3: Solutions for SPION-scFv cyanogen bromide conjugation

Buffers	**Formula**
50 mM Sodium borate buffer pH 8.5	Dissolve 4.77 g sodium tetraborate decahydrate in 200 ml dH_2O, adjust the pH with HCl and fill up to 250ml volume. Filter to sterilize.
Cyanogen bromide	5 M cyanogen bromide in acetonitrile (Sigma)
PBS	Add 10 ml 10x PBS to 90 ml dH_2O
50 mM Glycine	Dissolve 36 mg glycine in 10 ml 0.1 M sodium phosphate buffer pH 8.5. Filter to sterilize.

Table 2.4: Solutions for SPION-scFv site-specific conjugation

Buffers	Formula
50 mM Sodium borate buffer pH 8.5	Dissolve 4.77 g sodium tetraborate decahydrate in 200 ml dH_2O, adjust the pH with HCl and fill up to 250ml volume. Filter to sterilize.
50 mM Sodium borate buffer pH 7	Dissolve 4.77 g sodium tetraborate decahydrate in 200 ml dH_2O, adjust the pH with HCl and fill up to 250ml volume. Filter to sterilize.
Stabilization buffer	Dissolve 5 M sodium cyanoborohydride in 1 M NaOH.
50 mM Glycine	Dissolve 36 mg glycine in 10 ml 50 mM sodium borate buffer pH 8.5. Filter to sterilize.
50 mM Cysteine	Dissolve 0.6 g cysteine in 10 ml 50 mM sodium borate buffer pH 7. Filter to sterilize.

Table 2.5: Solutions for SDS-PAGE

Buffers	Formula
Running Buffer Stock (10X)	Dissolve 30 g Trizma® base and 144.2 g glycine in 1 l dH_2O.
Running Buffer	Dilute 100 ml running buffer stock with 900 ml dH_2O.
4X Reducing Buffer	Make 1.25 mM Tris-HCl, pH 6.8 solution in dH_2O; add 20% glycerol; 4% β-mercaptoethanol; 0.1% bromophenol blue and 0.1% SDS. All percentages w/v.
4X Non-reducing Buffer	Make 1.25 mM Tris-HCl, pH 6.8 solution in dH_2O; add 20% glycerol; 0.1% bromophenol blue and 0.1% SDS. All percentages w/v.
Coomassie gel stain	Mix 0.1 g coomassie blue R-250 with 100 ml methanol, 20 ml glacial acetic acid and 80 ml dH_2O.
Gel de-stain solution	For 2.5 l: mix 1.25 l methanol with 1 l dH_2O and 250 ml glacial acetic acid.

Table 2.6: Solutions for Western Blot

Buffers	Formula
Transfer Buffer Stock (10X)	Dissolve 30 g Trizma® base, 144.2 g glycine and 10 g SDS in 1 l dH_2O.
Transfer Buffer	Dilute 100 ml transfer buffer stock with 700 ml dH_2O and 200 ml methanol.
5% Milk	Dissolve 2.5 g milk powder (Marvel) in 50 ml PBS.

Table 2.7: Solutions for casting a native gel

Buffers	Formula
1 M Tris pH 6.8	Dissolve 30.3 g Trizma® base in 175 ml dH_2O and adjust the pH with concentrated HCl (37.2%). Bring up to final volume by adding dH_2O accordingly.
1 M Tris pH 8.8	Dissolve 30.3 g Trizma® base in 175 ml dH_2O and adjust the pH with concentrated 1 M NaOH. Bring up to final volume by adding dH_2O accordingly.
10% APS	Dissolve 1 g ammonium persulfate in 10 ml dH_2O. Prepare 100 µl aliquots and store at -20 °C
10% SDS	Add 25 g sodium dodecyl sulfate (SDS) to 220 ml dH_2O. Place the container into water bath at 65 °C to dissolve the SDS. After cooling add dH_2O for a final volume of 250 ml.

Table 2.8: Solutions for quartz crystal microbalance

Buffers	Formula
PBS	Dissolve PBS dry powder in 1 l dH_2O.
PBS-T	Take 1 l PBS and add 0.1% Tween-20.
BSA	Dissolve 1 mg bovine serum albumin in 1 ml PBS
Glycine pH 3	Add 75 mg glycine to 10 ml dH_2O and adjust pH to 3.

Table 2.9: Solutions for tissue culture

Buffers	**Formula**
Culture Medium for Capan-1	To 500 ml Iscove's Modified Dulbecco's Media (ATCC) add 100 ml FCS
Culture Medium for LS174T, A375M and SW1222	To 500 ml MEM with Earle's Salts add 5 ml 100x L-Glutamine, 50 ml FCS and 5 ml 100x NEAA
Trypsin	1x Trypsin (0.05%) w/ EDTA
PBS	Sterile 1x PBS
Freezing medium	Culture medium with 5% DMSO

Table 2.10: Solutions for tissue culture

Buffers	**Formula**
Fixing buffer	4% paraformaldehyde in dH_2O
50 mM Glycine	Dissolve 0.36 g glycine in 100 ml PBS

Table 2.11: Solutions for Prussian blue staining

Buffers	**Formula**
Reaction mix	Dissolve 4 g potassium ferrocyanide in 20 ml dH_2O and combine with 20 ml 2% HCl shortly before use.

All chemicals were purchased from Sigma-Aldrich (St. Louis, MO, USA). All buffers were filtered through 0.2 um Nalgene filter (VWR Int., Leicestershire, UK).

The reagents for tissue culture were obtained from PAA Laboratories (Pasching, Austria) unless specified.

Appendix II

Calculations

Determining the theoretical maximum energy loss (X")

$$\chi'' = \frac{\chi_0 \Omega \tau}{1+\Omega^2 \tau} \text{ -> max at } \Omega = \frac{1}{\tau}$$

$$\tau = \tau_0 \exp\left(\frac{KV}{k_B T}\right)$$

$$V = \frac{\pi}{6} d^3$$

$$\tau \approx 10^{-8} s$$

Assumptions:

$\tau_0 = 10^{-9} s$

$K \approx 11.5 kJ/m^3$ (magnetite)

$d = 12nm = 12 \cdot 10^{-9} m$

$|\chi''|$

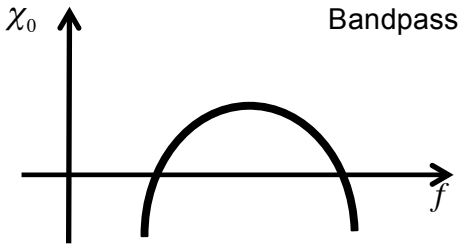

$$\left|\frac{\chi_0 j\frac{\omega}{\Omega}}{1+j\frac{\omega}{\Omega}}\right| -> \frac{\chi_0 \frac{\omega}{\Omega}}{1+\left(\frac{\omega}{\Omega}\right)^2} = \frac{\chi_0 \frac{\Omega}{\omega}}{1+\left(\frac{\Omega}{\omega}\right)^2}$$

$$\omega = \frac{1}{\tau} -> \left|\chi''\left(\omega = \frac{1}{\tau}\right)\right| = \frac{\chi_0 \Omega \tau}{1+(\Omega\tau)^2}$$

$$\omega = 2\pi f -> f = \frac{\omega}{2\pi} = \frac{1}{2\pi\tau} \approx 16MHz$$

Appendix III

References

Adams, G. P. and L. M. Weiner (2005). "Monoclonal antibody therapy of cancer." Nature Biotechnology **23**(9): 1147-1157.

Ahmad, Z. A., S. K. Yeap, et al. (2012). "scFv antibody: principles and clinical application." Clinical & developmental immunology **2012**: 980250.

Andra, W., C. G. d'Ambly, et al. (1999). "Temperature distribution as function of time around a small spherical heat source of local magnetic hyperthermia." Journal of Magnetism and Magnetic Materials **194**(1-3): 197-203.

Andrady, C., S. K. Sharma, et al. (2011). "Antibody-enzyme fusion proteins for cancer therapy." Immunotherapy **3**(2): 193-211.

Bates, P. A., J. C. Luo, et al. (1992). "A Predicted 3-Dimensional Structure for the Carcinoembryonic Antigen (Cea)." Febs Letters **301**(2): 207-214.

Biederer, S., T. Knopp, et al. (2009). "Magnetization response spectroscopy of superparamagnetic nanoparticles for magnetic particle imaging." Journal of Physics D-Applied Physics **42**(20): -.

Boehm, M. K., A. L. Corper, et al. (2000). "Crystal structure of the anti-(carcinoembryonic antigen) single-chain Fv antibody MFE-23 and a model for antigen binding based on intermolecular contacts." Biochemical Journal **346**: 519-528.

Boozer, C., G. Kim, et al. (2006). "Looking towards label-free biomolecular interaction analysis in a high-throughput format: a review of new surface plasmon resonance technologies." Current Opinion in Biotechnology **17**(4): 400-405.

Bordelon, D. E., C. Cornejo, et al. (2011). "Magnetic nanoparticle heating efficiency reveals magneto-structural differences when characterized with wide ranging and high amplitude alternating magnetic fields." Journal of Applied Physics **109**(12).

Boyer, C., M. R. Whittaker, et al. (2010). "The design and utility of polymer-stabilized iron-oxide nanoparticles for nanomedicine applications." Npg Asia Materials **2**(1): 23-30.

Brezovich, I. (1988). "Low frequency hyperthermia: capacitive and ferromagnetic thermoseed methods." Medical Physics Monograph. **16**: 82-111.

Carroll, M. R., P. P. Huffstetler, et al. (2011). "The effect of polymer coatings on proton transverse relaxivities of aqueous suspensions of magnetic nanoparticles." Nanotechnology **22**(32): 325702.

Chabner, B. A. and T. G. Roberts (2005). "Timeline - Chemotherapy and the war on cancer." Nature Reviews Cancer **5**(1): 65-72.

Chandran, S. P., M. Chaudhary, et al. (2006). "Synthesis of gold nanotriangles and silver nanoparticles using Aloe vera plant extract." Biotechnology progress **22**(2): 577-583.

Cherukuri, P., E. S. Glazer, et al. (2010). "Targeted hyperthermia using metal nanoparticles." Advanced Drug Delivery Reviews **62**(3): 339-345.

Chester, K. A., R. H. J. Begent, et al. (1994). "Phage Libraries for Generation of Clinically Useful Antibodies." Lancet **343**(8895): 455-456.

Chester, K. A., A. Mayer, et al. (2000). "Recombinant anti-carcinoembryonic antigen antibodies for targeting cancer." Cancer Chemotherapy and Pharmacology **46**: S8-S12.

Chichel, A. S., J.; Kubaszewska, M.; Kanikowski, M. (2007). "Hyperthermia - description of a method and a review of clinical applications." Rep Pract Oncol Radiother **12**(5): 267-275.

Cho, M. H., E. J. Lee, et al. (2012). "A magnetic switch for the control of cell death signalling in in vitro and in vivo systems." Nature Materials **11**(12): 1038-1043.

Cooper, M. A. and V. T. Singleton (2007). "A survey of the 2001 to 2005 quartz crystal microbalance biosensor literature: applications of acoustic physics to the analysis of biomolecular interactions." Journal of Molecular Recognition **20**(3): 154-184.

Cullity, B. D. G., C. D.; (2008). Introduction to Magnetic Materials, Wiley-IEEE Press.

Curley, S. A. (2001). "Radiofrequency ablation of malignant liver tumors." Oncologist **6**(1): 14-23.

Day, E. S., J. G. Morton, et al. (2009). "Nanoparticles for thermal cancer therapy." J Biomech Eng **131**(7): 074001.

DeNardo, S. J., G. L. DeNardo, et al. (2005). "Development of tumor targeting bioprobes (In-111-chimeric L6 monoclonal antibody nanoparticles) for alternating magnetic field cancer therapy." Clinical Cancer Research **11**(19): 7087S-7092S.

Dobson, J. (2008). "Remote control of cellular behaviour with magnetic nanoparticles." Nature nanotechnology **3**(3): 139-143.

Dutz, S., J. H. Clement, et al. (2009). "Ferrofluids of magnetic multicore nanoparticles for biomedical applications." Journal of Magnetism and Magnetic Materials **321**(10): 1501-1504.

Eberbeck, D., F. Wiekhorst, et al. (2011). "How the size distribution of magnetic nanoparticles determines their magnetic particle imaging performance." Applied Physics Letters **98**(18).

Edelman, G. M. (1973). "Antibody structure and molecular immunology." Science **180**(88): 830-840.

ESF (2004). "Nanomedicine - An ESF-European Medical Research Councils (EMRC) Forward Look Report. Strasbourg cedex, France ESF.".

Ferguson, R. M., K. R. Minard, et al. (2011). "Optimizing magnetite nanoparticles for mass sensitivity in magnetic particle imaging." Medical Physics **38**(3): 1619-1626.

Gannon, C. J., P. Cherukuri, et al. (2007). "Carbon nanotube-enhanced thermal destruction of cancer cells in a noninvasive radiofrequency field." Cancer **110**(12): 2654-2665.

Gannon, C. J., C. R. Patra, et al. (2008). "Intracellular gold nanoparticles enhance non-invasive radiofrequency thermal destruction of human gastrointestinal cancer cells." J Nanobiotechnology **6**: 2.

Gilchrist, R. K., R. Medal, et al. (1957). "Selective Inductive Heating of Lymph Nodes." Annals of Surgery **146**(4): 596-606.

Giustini, A. J., R. Ivkov, et al. (2011). "Magnetic nanoparticle biodistribution following intratumoral administration." Nanotechnology **22**(34).

Gleich, B. and R. Weizenecker (2005). "Tomographic imaging using the nonlinear response of magnetic particles." Nature **435**(7046): 1214-1217.

Glockl, G., R. Hergt, et al. (2006). "The effect of field parameters, nanoparticle properties and immobilization on the specific heating power in magnetic particle hyperthermia." Journal of Physics-Condensed Matter **18**(38): S2935-S2949.

Gobin, A. M., M. H. Lee, et al. (2007). "Near-infrared resonant nanoshells for combined optical imaging and photothermal cancer therapy." Nano Letters **7**(7): 1929-1934.

Gold, P. and S. O. Freedman (1965). "Specific Carcinoembryonic Antigens of Human Digestive System." Journal of Experimental Medicine **122**(3): 467-&.

Gonzales-Weimuller, M., M. Zeisberger, et al. (2009). "Size-dependant heating rates of iron oxide nanoparticles for magnetic fluid hyperthermia." Journal of Magnetism and Magnetic Materials **321**(13): 1947-1950.

Goodwill, P. W. and S. M. Conolly (2011). "Multidimensional X-Space Magnetic Particle Imaging." Ieee Transactions on Medical Imaging **30**(9): 1581-1590.

Gref, R., M. Luck, et al. (2000). "'Stealth' corona-core nanoparticles surface modified by polyethylene glycol (PEG): influences of the corona (PEG chain length and surface density) and of the core composition on phagocytic uptake and plasma protein adsorption." Colloids and Surfaces B-Biointerfaces **18**(3-4): 301-313.

Greish, K. (2010). "Enhanced permeability and retention (EPR) effect for anticancer nanomedicine drug targeting." Methods in molecular biology **624**: 25-37.

Guilbault, G. G. and C. K. O'Sullivan (1999). "Commercial quartz crystal microbalances - theory and applications." Biosensors & Bioelectronics **14**(8-9): 663-670.

Hammarstrom, S. (1999). "The carcinoembryonic antigen (CEA) family: structures, suggested functions and expression in normal and malignant tissues." Semin Cancer Biol **9**(2): 67-81.

Hammerstingl, R., A. Huppertz, et al. (2008). "Diagnostic efficacy of gadoxetic acid (Primovist)-enhanced MRI and spiral CT for a therapeutic strategy: comparison with intraoperative and histopathologic findings in focal liver lesions." European Radiology **18**(3): 457-467.

Hergt, R., W. Andra, et al. (1998). "Physical limits of hyperthermia using magnetite fine particles." Ieee Transactions on Magnetics **34**(5): 3745-3754.

Hergt, R. and S. Dutz (2007). "Magnetic particle hyperthermia-biophysical limitations of a visionary tumour therapy." Journal of Magnetism and Magnetic Materials **311**(1): 187-192.

Hergt, R., S. Dutz, et al. (2006). "Magnetic particle hyperthermia: nanoparticle magnetism and materials development for cancer therapy." Journal of Physics-Condensed Matter **18**(38): S2919-S2934.

Hergt, R., S. Dutz, et al. (2008). "Effects of size distribution on hysteresis losses of magnetic nanoparticles for hyperthermia." Journal of Physics-Condensed Matter **20**(38): -.

Hergt, R., R. Hiergeist, et al. (2004). "Maghemite nanoparticles with very high AC-losses for application in RF-magnetic hyperthermia." Journal of Magnetism and Magnetic Materials **270**: 345-357.

Hergt, R., R. Hiergeist, et al. (2005). "Magnetic properties of bacterial magnetosomes as potential diagnostic and therapeutic tools." Journal of Magnetism and Magnetic Materials **293**(1): 80-86.

Hermanson, G. T. (2008). Bioconjugate Techniques, Academic Press.

Hildebrandt, B. and P. Wust (2007). "Interactions between hyperthermia and cytotoxic drugs." Cancer treatment and research **134**: 185-193.

Hofmann-Amtenbrink, M. v. R., B.; Hofmann, H; (2009). Superparamagnetic nanoparticles for biomedical applications. Nanostructured Materials for Biomedical Applications. M. C. Tan, Transworld Research Network.

Holliger, P. and P. J. Hudson (2005). "Engineered antibody fragments and the rise of single domains." Nature Biotechnology **23**(9): 1126-1136.

Huang, H., S. Delikanli, et al. (2010). "Remote control of ion channels and neurons through magnetic-field heating of nanoparticles." Nat Nanotechnol **5**: 602-606.

Ito, A., M. Shinkai, et al. (2001). "Augmentation of MHC class I antigen presentation via heat shock protein expression by hyperthermia." Cancer Immunology Immunotherapy **50**(10): 515-522.

Ito, A., M. Shinkai, et al. (2003). "Heat shock protein 70 expression induces antitumor immunity during intracellular hyperthermia using magnetite nanoparticles." Cancer Immunology Immunotherapy **52**(2): 80-88.

Johannsen, M., U. Gneveckow, et al. (2007). "Morbidity and quality of life during thermotherapy using magnetic nanoparticles in locally recurrent prostate cancer: results of a prospective phase I trial." International journal of hyperthermia : the official journal of European Society for Hyperthermic Oncology, North American Hyperthermia Group **23**(3): 315-323.

Johannsen, M., U. Gneveckow, et al. (2007). "Thermotherapy of prostate cancer using magnetic nanoparticles: feasibility, imaging, and three-dimensional temperature distribution." European Urology **52**(6): 1653-1661.

Johannsen, M., A. Jordan, et al. (2004). "Evaluation of magnetic fluid hyperthermia in a standard rat model of prostate cancer." Journal of Endourology **18**(5): 495-500.

Jones, P. T., P. H. Dear, et al. (1986). "Replacing the complementarity-determining regions in a human antibody with those from a mouse." Nature **321**(6069): 522-525.

Jonsson, U., L. Fagerstam, et al. (1991). "Real-time biospecific interaction analysis using surface plasmon resonance and a sensor chip technology." BioTechniques **11**(5): 620-627.

Jordan, A., R. Scholz, et al. (1997). "Effects of magnetic fluid hyperthermia (MFH) on C3H mammary carcinoma in vivo." International Journal of Hyperthermia **13**:587-605

Kalber, T. L., C. J. Smith, et al. (2005). "A longitudinal study of R2* and R2 magnetic resonance imaging relaxation rate measurements in murine liver after a single administration of 3 different iron oxide-based contrast agents." Investigative Radiology **40**(12): 784-791.

Kallumadil, M., M. Tada, et al. (2009). "Suitability of commercial colloids for magnetic hyperthermia." Journal of Magnetism and Magnetic Materials **321**(10): 1509-1513.

Kempe, H. and M. Kempe (2010). "The use of magnetite nanoparticles for implant-assisted magnetic drug targeting in thrombolytic therapy." Biomaterials **31**(36): 9499-9510.

Khalid, M. N., P. Simard, et al. (2006). "Long circulating poly(ethylene glycol)-decorated lipid nanocapsules deliver docetaxel to solid tumors." Pharmaceutical Research **23**(4): 752-758.

Kim, N. H., T. J. Baek, et al. (2007). "Highly sensitive biomolecule detection on a quartz crystal microbalance using gold nanoparticles as signal amplification probes." Analytical sciences : the international journal of the Japan Society for Analytical Chemistry **23**(2): 177-181.

Kirpotin, D. B., D. C. Drummond, et al. (2006). "Antibody targeting of long-circulating lipidic nanoparticles does not increase tumor localization but does increase internalization in animal models." Cancer Research **66**(13): 6732-6740.

Kohler, G. and C. Milstein (1975). "Continuous cultures of fused cells secreting antibody of predefined specificity." Nature **256**(5517): 495-497.

Kozissnik, B. G., L. A. W.; Chester, K. A.; Thanh, N. T. K.; (2012). Strategies for Functionalisation of Magnetic Nanoparticles for Biological Targets. Magnetic Nanoparticles: From Fabrication to Clinical Applications. N. T. K. Thanh, CRC Press.

Kresse, M., S. Wagner, et al. (1998). "Targeting of ultrasmall superparamagnetic iron oxide (USPIO) particles to tumor cells in vivo by using transferrin receptor pathways." Magnetic resonance in medicine : official journal of the Society of Magnetic Resonance in Medicine / Society of Magnetic Resonance in Medicine **40**(2): 236-242.

Krishnan, K. M. (2010). "Biomedical Nanomagnetics: A Spin Through Possibilities in Imaging, Diagnostics, and Therapy." IEEE Trans Magn **46**(7): 2523-2558.

Lampe, J., C. Bassoy, et al. (2012). "Fast reconstruction in magnetic particle imaging." Physics in Medicine and Biology **57**(4): 1113-1134.

Laniado, M. and A. Chachuat (1995). "[The endorem tolerance profile]." Der Radiologe **35**(11 Suppl 2): S266-270.

Lee, J. H., J. T. Jang, et al. (2011). "Exchange-coupled magnetic nanoparticles for efficient heat induction." Nat Nanotechnol **6**:418-422

Lepage, M. G. J. C. (2004). "Contrast mechanisms in magnetic resonance imaging." Journal of Physics: Conference Series **3**: 78-86.

Lin, L., H. Zhao, et al. (2000). "Study on colloidal Au-enhanced DNA sensing by quartz crystal microbalance." Biochemical and Biophysical Research Communications **274**(3): 817-820.

Lin, S. P. and J. J. Brown (2007). "MR contrast agents: Physical and pharmacologic basics." Journal of Magnetic Resonance Imaging **25**(5): 884-899.

Livney, Y. D., O. Ramon, et al. (2001). "Swelling of dextran gel and osmotic pressure of soluble dextran in the presence of salts." Journal of Polymer Science Part B-Polymer Physics **39**(22): 2740-2750.

Lutz, J. F., S. Stiller, et al. (2006). "One-pot synthesis of pegylated ultrasmall iron-oxide nanoparticles and their in vivo evaluation as magnetic resonance imaging contrast agents." Biomacromolecules **7**(11): 3132-3138.

Ma, M., Y. Wu, et al. (2004). "Size dependence of specific power absorption of Fe3O4 particles in AC magnetic field." Journal of Magnetism and Magnetic Materials **268**(1-2): 33-39.

Maier-Hauff, K., F. Ulrich, et al. (2011). "Efficacy and safety of intratumoral thermotherapy using magnetic iron-oxide nanoparticles combined with external beam radiotherapy on patients with recurrent glioblastoma multiforme." Journal of Neuro-Oncology **103**(2): 317-324.

Mailander, V. and K. Landfester (2009). "Interaction of Nanoparticles with Cells." Biomacromolecules **10**(9): 2379-2400.

Malmborg, A. C., A. Michaelsson, et al. (1992). "Real time analysis of antibody-antigen reaction kinetics." Scandinavian journal of immunology **35**(6): 643-650.

Mannix, R. J., S. Kumar, et al. (2008). "Nanomagnetic actuation of receptor-mediated signal transduction." Nature Nanotechnology **3**(1): 36-40.

Mao, X., L. Yang, et al. (2006). "A nanoparticle amplification based quartz crystal microbalance DNA sensor for detection of Escherichia coli O157:H7." Biosensors & Bioelectronics **21**(7): 1178-1185.

Mayer, A., R. J. Francis, et al. (2006). "A phase I study of single administration of antibody-directed enzyme prodrug therapy with the recombinant anti-carcinoembryonic antigen antibody-enzyme fusion protein MFECP1 and a bis-iodo phenol mustard prodrug." Clinical Cancer Research **12**(21): 6509-6516.

McBain, S. C., U. Griesenbach, et al. (2008). "Magnetic nanoparticles as gene delivery agents: enhanced transfection in the presence of oscillating magnet arrays." Nanotechnology **19**(40).

Meyer, T., A. M. Gaya, et al. (2009). "A Phase I Trial of Radioimmunotherapy with I-131-A5B7 Anti-CEA Antibody in Combination with Combretastatin-A4-Phosphate in Advanced Gastrointestinal Carcinomas." Clinical Cancer Research **15**(13): 4484-4492.

Morup, S. H., M. F.; Frandsen, C; (2010). Magnetic Nanoparticles. Comprehensive Nanoscience and Technology. **Vol. 1 Nanomaterials:** 437-491.

Mykhaylyk, O., Y. S. Antequera, et al. (2007). "Generation of magnetic nonviral gene transfer agents and magnetofection in vitro." Nature Protocols **2**(10): 2391-2411.

Myszka, D. G. (1997). "Kinetic analysis of macromolecular interactions using surface plasmon resonance biosensors." Current Opinion in Biotechnology **8**(1): 50-57.

Myszka, D. G. (2000). "Kinetic, equilibrium, and thermodynamic analysis of macromolecular interactions with BIACORE." Methods in Enzymology **323**: 325-340.

Napier, M. P., S. K. Sharma, et al. (2000). "Antibody-directed enzyme prodrug therapy: Efficacy and mechanism of action in colorectal carcinoma." Clinical Cancer Research **6**(3): 765-772.

Nash, M. A., J. J. Lai, et al. (2010). ""Smart" diblock copolymers as templates for magnetic-core gold-shell nanoparticle synthesis." Nano Letters **10**(1): 85-91.

Nunc. Retrieved 18.01.2012, from http://www.nuncbrand.com/us/page.aspx?id=1275 - Subsection2.

Ortega, D. (2012). Structure and Magnetism in Magnetic Nanoparticles. Magnetic Nanoparticles: From Fabrication to Clinical Applications. N. T. K. Thanh, CRC Press.

Otte, J. (1988). "Hyperthermia in Cancer-Therapy." European Journal of Pediatrics **147**(6): 560-569.

Owen, J., Q. Pankhurst, et al. (2012). "Magnetic targeting and ultrasound mediated drug delivery: Benefits, limitations and combination." International Journal of Hyperthermia **28**(4): 362-373.

Pankhurst, Q. A., J. Connolly, et al. (2003). "Applications of magnetic nanoparticles in biomedicine." Journal of Physics D-Applied Physics **36**(13): R167-R181.

Pankhurst, Q. A., N. K. T. Thanh, et al. (2009). "Progress in applications of magnetic nanoparticles in biomedicine." Journal of Physics D-Applied Physics **42**(22): -.

Pintaske, J., P. Martirosian, et al. (2006). "Relaxivity of gadopentetate dimeglumine (Magnevist), gadobutrol (Gadovist), and gadobenate dimeglumine (MultiHance) in human blood plasma at 0.2, 1.5, and 3 Tesla (vol 41, pg 213, 2006)." Investigative Radiology **41**(12): 859-859.

Plank, C., U. Schillinger, et al. (2003). "The magnetofection method: Using magnetic force to enhance gene delivery." Biological Chemistry **384**(5): 737-747.

Pothayee, N. B., S.; Pothayee, N.; Jain, N.; Hu, N.; Lin, Y.; Davis, R. M.; Sriranganathan, N.; Koretsky, A. P.; Riffle, J. S.; (2013). "Magnetic nanoclusters with hydrophilic spacing for dual drug delivery and sensitive magnetic resonance imaging." Journal of Materials Chemistry B **1**: 1142-1149.

Rabin, Y. (2002). "Is intracellular hyperthermia superior to extracellular hyperthermia in the thermal sense?" International Journal of Hyperthermia **18**: 194-202

Reimer, P. and T. Balzer (2003). "Ferucarbotran (Resovist): a new clinically approved RES-specific contrast agent for contrast-enhanced MRI of the liver: properties, clinical development, and applications." European Radiology **13**(6): 1266-1276.

Riemer, J., H. H. Hoepken, et al. (2004). "Colorimetric ferrozine-based assay for the quantitation of iron in cultured cells." Analytical Biochemistry **331**(2): 370-375.

Rosensweig, R. E. (1997). Ferrohydrodynamics, Dover Publications.

Rosensweig, R. E. (2002). "Heating magnetic fluid with alternating magnetic field." Journal of Magnetism and Magnetic Materials **252**(1-3): 370-374.

Ruoslahti, E., S. N. Bhatia, et al. (2010). "Targeting of drugs and nanoparticles to tumors." Journal of Cell Biology **188**(6): 759-768.

Sainz-Pastor, N., B. Tolner, et al. (2006). "Deglycosylation to obtain stable and homogeneous Pichia pastoris-expressed N-A1 domains of carcinoembryonic antigen." Int J Biol Macromol **39**(1-3): 141-150.

Sainz-Pastor, N., B. Tolner, et al. (2006). "Deglycosylation to obtain stable and homogeneous Pichia pastoris-expressed N-A1 domains of carcinoembryonic antigen." International Journal of Biological Macromolecules **39**(1-3): 141-150.

Sarwar, A., R. Lee, et al. (2013). "Magnetic Injection of Nanoparticles Into Rat Inner Ears at a Human Head Working Distance." Ieee Transactions on Magnetics **49**(1): 440-452.

Sarwar, A., A. Nemirovski, et al. (2012). "Optimal Halbach permanent magnet designs for maximally pulling and pushing nanoparticles." Journal of Magnetism and Magnetic Materials **324**(5): 742-754.

Sattel, T. F., T. Knopp, et al. (2009). "Single-sided device for magnetic particle imaging." Journal of Physics D-Applied Physics **42**(2): -.

Scott, A. M., J. D. Wolchok, et al. (2012). "Antibody therapy of cancer." Nature reviews. Cancer **12**(4): 278-287.

Simon, G. H., J. von Vopelius-Feldt, et al. (2006). "Ultrasmall supraparamagnetic iron oxide-enhanced magnetic resonance imaging of antigen-induced

arthritis: a comparative study between SHU 555 C, ferumoxtran-10, and ferumoxytol." Invest Radiol **41**(1): 45-51.

Singh, N., G. J. S. Jenkins, et al. (2010). "Potential toxicity of superparamagnetic iron oxide nanoparticles (SPION)." Nano Reviews doi:10.3402/nano.v1i0.5358

Strebhardt, K. and A. Ullrich (2008). "Paul Ehrlich's magic bullet concept: 100 years of progress." Nat Rev Cancer **8**(6): 473-480.

Stride, E., C. Porter, et al. (2009). "Enhancement of Microbubble Mediated Gene Delivery by Simultaneous Exposure to Ultrasonic and Magnetic Fields." Ultrasound in Medicine and Biology **35**(5): 861-868.

Stride, E. P. and C. C. Coussios (2010). "Cavitation and contrast: the use of bubbles in ultrasound imaging and therapy." Proceedings of the Institution of Mechanical Engineers Part H-Journal of Engineering in Medicine **224**(H2): 171-191.

Thanh, N. T. K. and L. A. W. Green (2010). "Functionalisation of nanoparticles for biomedical applications." Nano Today **5**(3): 213-230.

Theis, T., D. Parr, et al. (2006). "nan'o.tech.nol'o.gy n." Nat Nanotechnol **1**(1): 8-10.

Thomas, L. A., L. Dekker, et al. (2009). "Carboxylic acid-stabilised iron oxide nanoparticles for use in magnetic hyperthermia." Journal of Materials Chemistry **19**(36): 6529-6535.

Thomassen, L. C., A. Aerts, et al. (2010). "Synthesis and characterization of stable monodisperse silica nanoparticle sols for in vitro cytotoxicity testing." Langmuir : the ACS journal of surfaces and colloids **26**(1): 328-335.

Tiefenauer, L. X., G. Kuhne, et al. (1993). "Antibody-magnetite nanoparticles: in vitro characterization of a potential tumor-specific contrast agent for magnetic resonance imaging." Bioconjugate Chemistry **4**(5): 347-352.

Tiselius, A. and E. A. Kabat (1939). "An Electrophoretic Study of Immune Sera and Purified Antibody Preparations." The Journal of experimental medicine **69**(1): 119-131.

Tjandra, J. J., L. Ramadi, et al. (1990). "Development of human anti-murine antibody (HAMA) response in patients." Immunology and cell biology **68 (Pt 6)**: 367-376.

Tolner, B., L. Smith, et al. (2006). "Production of recombinant protein in Pichia pastoris by fermentation." Nature Protocols **1**(2): 1006-1021.

Tolner, B. B., G.; Foster, B; Vigor, K.; Chester, K.; (2013). Production of Recombinant Proteins from Pichia pastoris: Interfacing Fermentation and Immobilized Metal Ion Affinity Chromatography. Laboratory Protocols in

Fungal Biology: Current Methods in Fungal Biology. V. K. T. Gupta, M. G.; , Springer**:** 629.

Torigoe, T., Y. Tamura, et al. (2009). "Heat shock proteins and immunity: Application of hyperthermia for immunomodulation." International Journal of Hyperthermia **25**(8): 610-616.

Elias, E., E. Tsourkas (2009). "Imaging circulating cells and lymphoid tissues with iron oxide nanoparticles." Hematology Am Soc Hematol Educ Program 720-726

van der Zee, J. (2002). "Heating the patient: a promising approach?" Annals of Oncology **13**(8): 1173-1184.

van der Zee, J., D. G. Gonzalez, et al. (2000). "Comparison of radiotherapy alone with radiotherapy plus hyperthermia in locally advanced pelvic tumours: a prospective, randomised, multicentre trial." Lancet **355**(9210): 1119-1125.

van Landeghem, F. K., K. Maier-Hauff, et al. (2009). "Post-mortem studies in glioblastoma patients treated with thermotherapy using magnetic nanoparticles." Biomaterials **30**(1): 52-57.

Vigor, K. L., P. G. Kyrtatos, et al. (2009). "Nanoparticles functionalised with recombinant single chain Fv antibody fragments (scFv) for the magnetic resonance imaging of cancer cells." Biomaterials.

Weizenecker, J., B. Gleich, et al. (2009). "Three-dimensional real-time in vivo magnetic particle imaging." Physics in Medicine and Biology **54**(5): L1-L10.

Wust, P., B. Hildebrandt, et al. (2002). "Hyperthermia in combined treatment of cancer." Lancet Oncology **3**(8): 487-497.

Weller, M., W. Wick (2011). "Nanomania ante portas of neurooncology?" Journal of Neuro-Oncology **104**(2): 613-614

Xie, H., Y. Gu, et al. (2005). "Dendrimer-mediated synthesis of platinum nanoparticles: new insights from dialysis and atomic force microscopy measurements." Nanotechnology **16**(7): S492-501.